

Digital Image Correlation in Dynamic Punch Testing and  
Plastic Deformation Behavior of Inconel 718

THESIS

Presented in Partial Fulfillment of the Requirements for the Degree  
Master of Science in the Graduate School of The Ohio State  
University

By

Timothy James Liutkus, B.S.

Graduate Program in Mechanical Engineering

The Ohio State University

2014

Master's Examination Committee:

Dr. Amos Gilat, Advisor

Dr. Mark Walter

© Copyright by  
Timothy James Liutkus  
2014

## **Abstract**

A custom punch-die fixture allowing full field three-dimensional Digital Image Correlation (DIC) measurements on the rear surface of the specimen is introduced for dynamic and quasi-static punch experiments. The punch fixture design methodology is described. Results from punch experiments on 5.08 mm Ti-6Al-4V disk specimens using three different punch geometries in both dynamic and quasi-static conditions are presented and discussed. These experiments can be used to generate material failure data under complex stress states. Such data is essential in developing and calibrating complex material models, like those developed for precipitate hardened Inconel 718.

The plastic behavior of precipitate hardened Inconel 718 under various strain rates, orientations, and temperatures is examined; and a punch experiment that uses 3D-DIC measurements of the punch specimen is presented. The research presented herein is part of an ongoing project to develop and calibrate a material model in a finite element code, LS-DYNA. Such models are valuable for the simulation of dynamic events, such as blade off failure in aircraft engines.

The equipment, theory, and methodologies used to complete experiments in tension and compression at different strain rates and temperatures are presented. Quasi-static experiments are conducted using a biaxial servo-hydraulic load frame and dynamic experiments using two split Hopkinson bars. A specially designed furnace and adapters are used to complete experiments at

elevated temperatures. DIC is an optical method for measuring full field deformations and strains on the specimen surface that is utilized extensively in this work.

Experimental results for precipitate hardened Inconel 718 are presented and discussed. The material shows significant strain hardening and some strain rate sensitivity in tension. Data from experiments at elevated temperature show complex temperature dependence. The material shows decreasing flow stress with increasing temperature and decreasing ductility between 21°C and 600°C. Between 600° and 800°C the ductility increases significantly. Compression experiments at various strain rates show similar strain hardening and less rate sensitivity than in tension. The material is anisotropic in the  $\pm 45^\circ$  from rolling directions and shows anisotropy between tension and compression loadings in the transverse direction. These data are used to determine parameters for a Johnson-Cook plasticity model, and yield criteria are discussed.

Additional work is presented for the design of plane stress, plane strain, and axisymmetric fracture specimens. These specimens will be used in future work in the generation of a failure surface based on stress triaxiality and lode parameter – two stress-state parameters which govern material failure.

This document is dedicated to my family, friends,  
and mentors who have helped me along the way.

## **Acknowledgments**

My success up to this point in my life is, in no small part, due to the unending support of many fantastic people; and I would like to take the opportunity to thank them. First I would like to thank my parents Tom and Terri Liutkus, whose love, support, and vision for their children have been critical throughout my entire life. Thank you for enthusiastically cheering my successes and helping me back to my feet in my failures. To my best friends – Josh Hirsch, Jim Gross, James Asimes, and Danny Joyce – your inspiration, counsel, and support has been extraordinary. To my Phi Gamma Delta fraternity brothers, I would not have dreamt of this without your mentorship and brotherhood.

Special recognition is due to my Advisor, Professor Amos Gilat, who has been a tremendous mentor and inspiration. His advice and support have been spectacular throughout my work here, and I am eternally thankful for the opportunity to work with him. Dr. Jeremy Seidt has been a great mentor and colleague, and I especially appreciate the countless advice he has given me both professionally and as a friend. I cannot overstate Jeremy's value to this project and my own experience in the past two years. A special thank you, also, to Professor Mark Walter for his work on my thesis defense committee.

This research was funded by the Federal Aviation Administration with collaboration from the National Aeronautics and Space Administration, George Washington University, and George Mason University. Thanks to Bill Emmerling, Chip Queitzsch, and Don Altobelli at the FAA for their advice and support throughout the past two years. Thanks to Mike Pereira, Kelly Carney,

and Brad Lerch at NASA for their support in this project as well. Additional thanks go to Paul Dubois and Steve Kan.

Finally, thank you to my fellow students and colleagues in the Dynamic Mechanics of Materials Lab. Special thanks go out to Jeremiah Hammer and Kevin Gardner, who – in addition to providing support and friendship – did work that was essential in the research presented here. Thanks to Jarrod Smith for his friendship and willingness to help at the drop of a coin, and thanks and good luck to Aaron Ressa as he continues the study of this material.

## Vita

2007.....St. Ignatius High School, Cleveland, OH

2012.....B.S. Mechanical Engineering,  
The Ohio State University

### Publications:

Hammer, J.T., Liutkus, T. J., Seidt, J.D., Gilat, A., “Using Digital Image Correlation (DIC) in Dynamic Punch Tests”, *Experimental Mechanics* (Submitted Dec. 2012).

## Fields of Study

Major Field: Mechanical Engineering, Experimental Mechanics, Dynamic Behavior of Materials, Plasticity, Computational Mechanics

## Table of Contents

	<b>Page</b>
Abstract.....	ii
Acknowledgments.....	v
Vita.....	vii
Table of Contents.....	viii
List of Tables.....	xi
List of Figures.....	xii
Chapter 1: Introduction.....	1
1.1 Motivation & Objectives.....	3
Chapter 2: Digital Image Correlation in Dynamic Punch Tests.....	5
2.1 Introduction.....	5
2.2 Punch Testing Literature Review.....	6
2.3 Experimental Setup.....	8
2.3.1 The Dynamic Punch Test Setup.....	9
2.3.2 The Quasi-Static Punch Test Setup.....	14
2.4 Experimental Results & Discussion.....	15
2.5 Summary and Conclusions.....	23
Chapter 3: Plastic Deformation Behavior of Precipitate Hardened Inconel 718.....	25

3.1	Introduction .....	25
3.2	Inconel 718 Literature Review .....	25
3.3	Plastic Deformation of Precipitate Hardened Inconel 718: Experimental Procedures and Techniques.....	26
3.3.1	Tension Experiments .....	27
3.3.2	Compression Experiments .....	41
3.3.3	Three Dimensional Digital Image Correlation (DIC).....	46
3.4	Plastic Deformation of Precipitate Hardened Inconel 718 Experimental Results & Discussion.....	49
3.4.1	Strain Rate Sensitivity Test Series .....	50
3.4.2	Tension Anisotropy Test Series .....	52
3.4.3	Tension Temperature Dependence Test Series.....	53
3.4.4	Compression Strain Rate Sensitivity Test Series.....	55
3.4.5	Compression Anisotropy Test Series.....	58
3.4.6	Comparison of Tension and Compression Data .....	59
3.4.7	Constitutive Modeling of Precipitate Hardened Inconel 718 .....	63
3.5	Summary & Conclusions .....	70
Chapter 4:	Inconel 718 Fracture Specimen Design .....	71
4.1	Introduction & Background .....	71
4.2	Design Process & Final Geometries.....	72
4.3	Summary & Conclusions .....	78
Appendix A:	Principal Strain Histories – 3D DIC in Punch Experiments .....	80
A.1	Sharp Punch Experiments .....	81
A.1.1	Quasi-Static Experiments.....	81

A.1.2	Dynamic Punch Experiments.....	83
A.2	Hemispherical Punch Experiments .....	86
A.2.1	Quasi-static Experiments .....	86
A.2.2	Dynamic Experiments.....	89
Appendix B:	Full Experimental Results – Precipitate Hardened Inconel 718.....	92
B.1	Experimental Results: Tension Strain Rate Sensitivity.....	93
B.2	Experimental Results: Tension Anisotropy.....	96
B.3	Experimental Results: Compression Strain Rate Sensitivity .....	98
B.4	Experimental Results: Compression Anisotropy .....	101
Appendix C:	Finite Element Meshes Used in the Design of Specimen Geometries for the Ductile Fracture Test Series.....	104
C.1	Plane Stress Specimens .....	105
C.2	Plane Strain Specimens .....	107
C.3	Axisymmetric Specimens.....	110
Bibliography	.....	116

## List of Tables

Table 3.1: Experimental outline for plastic deformation testing of precipitate hardened Inconel 718 in tension loadings. ....	27
Table 3.2: Precipitate hardening heat treatment profile.....	28
Table 3.3: Material composition of 12.7mm plate stock .....	28
Table 3.4: Experimental outline for precipitate hardened Inconel 718 plastic deformation tests in compression. ....	41
Table 3.5: Johnson-Cook model parameter comparison.....	64
Table 4.1: Plane stress fracture specimen geometry, stress triaxiality, and lode parameter. ....	75
Table 4.2: Plane strain fracture specimen geometry, stress triaxiality, and lode parameter. ....	76
Table 4.3: Axisymmetric fracture specimen geometry, average stress triaxialty, and lode parameter.....	78

## List of Figures

Figure 2.1: Ti-6Al-4V punch specimen geometry.....	8
Figure 2.2: Stress triaxiality results from 5.08mm thick specimen LS-DYNA simulation.	9
Figure 2.3: Dynamic punch test - experimental setup: (a) sketch and (b) close-up of die fixture-specimen and punch.....	10
Figure 2.4: Tungsten carbide punches: (a) Sharp (6.35mm radius), (b) Hemispherical (12.17mm radius), (c) Blunt.....	11
Figure 2.5: (a) Slotted die fixture (left) and solid holder design (right), (b) Comparison of transmitted wave to incident pulse.....	13
Figure 2.6: Simulated and experimental wave propagation through slotted-die fixture...	14
Figure 2.7: Quasi-static punch test setup .....	15
Figure 2.8: Elastic waves recorded for a dynamic punch test using the hemispherical (12.17mm radius) punch .....	16
Figure 2.9: Maximum principal strain contours for a dynamic test with the hemispherical punch at (a) 0 $\mu$ s, (b) 40 $\mu$ s, (c) 90 $\mu$ s, (d) 130 $\mu$ s, (e) 180 $\mu$ s, (f) 230 $\mu$ s after load initiation .....	17
Figure 2.10: Principal strain evolution for specimen center point (blue) and failure point (green) in dynamic punch test with hemispherical punch geometry .....	18
Figure 2.11: Force and displacement history for a quasi-static punch test using the hemispherical punch. ....	18
Figure 2.12: Maximum principal strain contours for a quasi-static punch experiment using the hemispherical punch. Images correspond to times (a) 0s, (b) 32.25s, (c) 70.50s, (d) 105.50s, (e) 140.76s, (f) 176.2s after load initiation.....	19
Figure 2.13: Principal strain and applied contact force history - quasi-static punch experiment with hemispherical punch .....	20

Figure 2.14: Static and dynamic contact force versus displacement data for: (a) Sharp, (b) blunt, and (c) hemispherical punch geometries .....	21
Figure 2.15: equivalent strain versus principal strain ratio data for (a) sharp punch and (b) hemispherical punch experiments.....	23
Figure 3.1: Tension Specimen Geometry.....	29
Figure 3.2: : Specimen Orientations in 12.7mm Inconel 718 plate .....	29
Figure 3.3: Dynamic tension geometry.....	30
Figure 3.4: Elevated temperature tension specimen geometry.....	30
Figure 3.5: Quasi-static tension setup.....	31
Figure 3.6: Tension SHB schematic.....	33
Figure 3.7: Tension SHB (left) and dynamic tension specimen in adapter (right).....	34
Figure 3.8: Comparison of strain measurements versus time. Large dashed curves represent wave data and solid lines represent virtual extensometer data. The small dashes show strains measured using DIC at the specimen failure point.....	36
Figure 3.9: Axial strain across a specimen at different times in a dynamic tension experiment at $500\text{s}^{-1}$ .....	37
Figure 3.10: Axial strain across a specimen at different times in a dynamic tension experiment at $2000\text{s}^{-1}$ .....	37
Figure 3.11: Close-up view of elevated temperature setup.....	38
Figure 3.12: Overall view of elevated temperature tension setup.....	39
Figure 3.13: Tension adapters for high temperature experiments. Components are: Inconel adapter (orange), #8 Screw (red), #8 Hex Nut (yellow), and Hastalloy-X Bushings (blue).....	40
Figure 3.14: Compression specimen geometry.....	42
Figure 3.15: Quasi-static compression setup .....	43
Figure 3.16: Compression SHB schematic diagram.....	45
Figure 3.17: Photograph of compression SHB.....	45

Figure 3.18: 4mm extensometer used in tension data processing. (a) initial length (b) length prior to failure. ....	48
Figure 3.19: (a) 2mm extensometer and (b) platen area data used in compression DIC measurements.....	49
Figure 3.20: True stress versus true strain data for tension experiments at different strain rates. ....	50
Figure 3.21 - True stress (MPa) at 5% strain versus strain rate ( $s^{-1}$ ) data in tension for precipitate hardened Inconel 718.....	51
Figure 3.22 - True stress (MPa) versus true strain data from two tests: one at $1.0 \times 10^{-2} s^{-1}$ , one at $1.0 s^{-1}$ . Notice the change in the rate of strain hardening beginning around $\epsilon_T = 0.011$ . ....	52
Figure 3.23 - True stress (MPa) versus true strain data for tension anisotropy experiments. Note that representative curves from the test series are shown for clarity. ....	53
Figure 3.24 - True stress (MPa) versus true strain data from tension experiments carried out at room temperature (red curves), 200°C (blue), 400°C (green), 600°C (purple), and 800°C (grey).....	54
Figure 3.25: True strain at failure versus temperature data. Experimental data (blue) is compared to ASM handbook data (red).....	55
Figure 3.26: True stress (MPa) versus true strain data for compression experiments at various strain rates. ....	56
Figure 3.27: True stress (MPa) at $\epsilon = 0.10$ versus strain rate for the compression test series .....	57
Figure 3.28: True stress (MPa) versus true strain data for two compression tests. ....	58
Figure 3.29: Representative true stress (MPa) versus true strain data from compression experiments conducted at a nominal strain rate of $1.0 s^{-1}$ on specimens machined in various orientations.....	59
Figure 3.30: Effective stress versus equivalent plastic strain data for the tension and compression loading conditions at the $1.0 s^{-1}$ strain rate. ....	60
Figure 3.31: Comparison of rate sensitivity data for tension and compression. True stress at 10% true strain versus strain rate. ....	61

Figure 3.32: Effective stress versus equivalent plastic strain data for specimens with various plate orientations .....	62
Figure 3.33: Effective Stress at 10% equivalent plastic strain and specimen orientation with 95% confidence intervals.....	63
Figure 3.34: Johnson-Cook curves and tension data at $1.0 \times 10^{-4} \text{s}^{-1}$ .....	65
Figure 3.35: Johnson-Cook curves and tension data at $2000 \text{s}^{-1}$ .....	66
Figure 3.36: Model predictions and experimental data - true stress (MPa) at 5% strain versus strain rate. ....	66
Figure 3.37: Model predictions for tension temperature dependence. Effective stress at 5% strain versus $T^*$ .....	67
Figure 3.38: Model predictions and experimental data for compression experiments at $1.0 \times 10^{-4} \text{s}^{-1}$ .....	68
Figure 3.39: Model predictions and experimental data for compression experiments at $2000 \text{s}^{-1}$ .....	69
Figure 3.40: Johnson-Cook curve fits and experimental data for strain rate sensitivity. Effective stress @ 10% strain versus strain rate. ....	69
Figure 4.1: Representative meshes for plane stress (left), plane strain (center), and axisymmetric (right) specimen geometries. ....	73
Figure 4.2: Meshed geometries with arrows highlighting the location from which data is extracted in fracture specimen design process.....	74
Figure 4.3: Necked sample geometry as used in Bridgman's equation.....	77
Figure A.1: Principal strain and load history for a quasi-static punch test using the sharp punch geometry.....	81
Figure A.2: Principal strain and load history for a quasi-static punch test using the sharp punch geometry.....	82
Figure A.3: Principal strain and load history for a quasi-static punch test using the sharp punch geometry.....	82
Figure A.4: Principal strain history for a dynamic punch experiment using the sharp punch geometry.....	83

Figure A.5: Principal strain history for a dynamic punch experiment using the sharp punch geometry.....	84
Figure A.6: Principal strain history for a dynamic punch experiment using the sharp punch geometry.....	85
Figure A.7: Principal strain and load history for a quasi-static punch experiment with the hemispherical punch geometry. ....	86
Figure A.8: Principal strain and load history for a quasi-static punch experiment with the hemispherical punch geometry. ....	87
Figure A.9: Principal strain and load history for a quasi-static punch experiment with the hemispherical punch geometry. ....	88
Figure A.10: Strain history for a dynamic punch experiment using the hemispherical punch geometry.....	89
Figure A.11: Strain history for a dynamic punch experiment using the hemispherical punch geometry.....	90
Figure A.12: Strain history for a dynamic punch experiment using the hemispherical punch geometry.....	91
Figure B.1: Experimental results from tension experiments at $1.0 \times 10^{-4} \text{s}^{-1}$ .....	93
Figure B.2: Experimental results from tension experiments at $1.0 \times 10^{-2} \text{s}^{-1}$ .....	93
Figure B.3: Experimental results from tension experiments at $1.00 \text{s}^{-1}$ .....	94
Figure B.4: Experimental results from tension experiments at $500 \text{s}^{-1}$ .....	94
Figure B.5: Experimental results for tension experiments conducted at $2000 \text{s}^{-1}$ . ....	95
Figure B.6: Experimental results for tension experiments conducted at $1.00 \text{s}^{-1}$ in the rolled direction .....	96
Figure B.7: Experimental results for tension experiments conducted at $1.00 \text{s}^{-1}$ in the $+45^\circ$ direction. ....	96
Figure B.8: Experimental Results for tension experiments conducted at $1.00 \text{s}^{-1}$ in the $-45^\circ$ direction. ....	97
Figure B.9: Experimental Results for Tension Experiments conducted at $1.00 \text{s}^{-1}$ in the Transverse Direction.....	97

Figure B.10: Experimental results for compression experiments conducted at $1.0 \times 10^{-4} \text{s}^{-1}$ . .....	98
Figure B.11: Experimental results for compression experiments conducted at $1.0 \times 10^{-2} \text{s}^{-1}$ . .....	98
Figure B.12: Experimental results for compression experiments conducted at $1.00 \text{s}^{-1}$ ....	99
Figure B.13: Experimental results for compression experiments conducted at $1000 \text{s}^{-1}$ ...	99
Figure B.14: Experimental results for compression experiments conducted at $2000 \text{s}^{-1}$ .	100
Figure B.15: Experimental results for compression experiments conducted at $1.00 \text{s}^{-1}$ in the rolled direction .....	101
Figure B.16: Experimental results for compression experiments conducted at $1.00 \text{s}^{-1}$ in the $45^\circ$ direction.....	101
Figure B.17: Experimental results for compression experiments conducted at $1.00 \text{s}^{-1}$ in the transverse direction. ....	102
Figure B.18: Experimental results for compression experiments conducted at $1.00 \text{s}^{-1}$ in the $-45^\circ$ direction. ....	102
Figure B.19: Experimental results for compression experiments conducted at $1.00 \text{s}^{-1}$ in the direction through the thickness. ....	103
Figure C.1: Mesh for SG1, plane stress smooth, geometry. ....	105
Figure C.2: Mesh for SG2, plane stress large notched, geometry. ....	105
Figure C.3: Mesh for SG3, plane stress medium notched, geometry. ....	106
Figure C.4: Mesh for SG4, plane stress small notched, geometry.....	106
Figure C.5: Mesh for SG11, plane strain smooth, geometry. ....	107
Figure C.6: Mesh for SG12, plane strain large notch, geometry. ....	108
Figure C.7: Mesh for SG13, plane strain medium notch, geometry. ....	109
Figure C.8: Mesh for SG5, axisymmetric smooth, geometry. ....	110
Figure C.9: Mesh for SG6, axisymmetric notched, geometry. ....	111

Figure C.10: Mesh for SG7, axisymmetric notched, geometry. ....	112
Figure C.11: Mesh for SG8, axisymmetric notched, geometry. ....	113
Figure C.12: Mesh for SG9, axisymmetric notched, geometry. ....	114
Figure C.13: Mesh for SG10, axisymmetric notched, geometry. ....	115

## Chapter 1: Introduction

As engineers rely more and more on finite element analyses during the design process, the requirement for accurate material models grows. Finite element modeling is a cost effective way for evaluating complex component and system designs. Simulations can involve complex geometry, multiple materials, and complex boundary conditions. Traditional design processes concern themselves with a part's elastic behavior, but for many mechanical systems there are design requirements that require simulating a part's plastic deformation and failure. Such simulations require more complex material models, as plastic deformation is more affected by variables such as strain rate, temperature, anisotropy, and other factors. Existing numerical codes can accurately simulate materials under complex loading conditions only if the material model takes these conditions into account.

One such material model is the Johnson-Cook model [1]. This model is commonly used in simulations where plastic deformation and failure of materials in dynamic loading conditions is required. Johnson-Cook is a phenomenological model, meaning the model is curve fit to observed material behavior. Specifically, the Johnson-Cook model accounts for strain hardening, strain rate sensitivity, and temperature dependence. The constitutive equation for the model is given by

$$\bar{\sigma} = [A + B\varepsilon^n] \left[ 1 + C \ln \left( \frac{\dot{\varepsilon}}{\dot{\varepsilon}_0} \right) \right] \left[ 1 - \left( \frac{T - T_r}{T_m - T_r} \right)^m \right] \quad (1)$$

where  $\bar{\sigma}$  is the effective flow stress,  $\varepsilon$  is the equivalent plastic strain,  $\dot{\varepsilon}_0$  is the reference strain rate,  $\dot{\varepsilon}$  is the actual strain rate,  $T$  is the test temperature,  $T_r$  is room temperature, and  $T_m$  is the

melting temperature. A, B, n, C, and m are constants which may be determined from experimental data.

The work presented in this document falls into two categories. The first section presents a new technique for carrying out dynamic punch tests with three dimensional digital image correlation. A custom designed die fixture allows for a stereoscopic view of the rear surface of a thin disk punch specimen. Data from such an experiment can be used to both develop material models and, importantly, validate data from simulations using existing material models. This capability is critical because these material models form the basis of finite element analyses used in predictive design. The second set of research aims to create a database of experimental data for precipitate hardened Inconel 718 for the calibration of MAT224, a material model incorporated in LS-DYNA [2]. This is a tabulated model, which uses tabulated stress strain curves at different strain rates and temperatures to predict material response. This work is part of an ongoing project to develop MAT224.

A large team is dedicated to carrying out this ongoing project. Researchers in The Ohio State University's Dynamic Mechanics of Materials Lab (DMML) generate experimental data from coupon tests under a range of conditions. Researchers from George Mason University are focused on the development and calibration of the material model. Scientists at the National Aeronautics and Space Administration (NASA) at Cleveland's Glenn Research Center (GRC) carry out ballistic impact experiments, microstructural analysis, and additional LS-DYNA support. Several members from the Federal Aviation Administration (FAA) oversee the program as part of the FAA's Uncontained Engine Debris Mitigation Program.

## 1.1 Motivation & Objectives

The extreme environments inherent in aircraft turbines pose challenges to the design process. For instance, the hot section of a jet engine reaches temperatures of over 1300°C and can operate in excess of 10,000 RPM. Because of these temperatures and velocities, failure of a component can cause catastrophic damage.

In jet engines, blade-off and disk failures have the greatest potential for such damage. These events are characterized by mechanical failure in which a part of the blade or disk is expelled away from the center of the engine. This component becomes a projectile that can subsequently penetrate the engine shroud. Uncontained debris can cause failure of the engine and substantial damage to the aircraft.

To ensure the safety of passengers and crew, government regulations are in place to minimize the potential for such a catastrophic engine failure. Federal Aviation Administration (FAA) regulation 25.903 subsection (d) states:

*(1) Design precautions must be taken to minimize the hazards to the airplane in the event of an engine rotor failure or of a fire originating within the engine which burns through the engine case.*

Despite this regulation, these failures do happen. In 2010, Qantas Flight 32, en route to Sydney from Singapore, suffered an uncontained engine failure shortly after takeoff [3]. The damage to their number 2 engine resulted in an oil fire and forced the aircraft to make an emergency landing in Singapore. There were no fatalities in this incident. In 1984, a compressor disc in a Pratt & Whitney JT8D-15 engine failed while Cameroon Airlines flight 786 taxied for takeoff at Douala Airport in Cameroon [4]. Uncontained debris punctured the wing and a fuel tank, and the aircraft burned out resulting in two deaths. Perhaps the most famous and most deadly incident involving

uncontained engine failure is United Airlines Flight 232. This DC-10 suffered damage to its rear engine en route to Chicago from Denver in 1989 [5]. Debris from the failure severed all three hydraulic systems. The aircraft crashed upon landing in Sioux City, Iowa, and 111 people perished. These incidents and others emphasize the potential for catastrophic damage and loss of life that can result from an uncontained engine failure.

Because of such dangerous potential, designers must be able to reliably predict the behavior of components and materials in the event of a blade-off failure. To computationally simulate such an event, the material models used must accurately describe the material behavior at elevated temperatures, high strain rates, and complex stress states.

To calibrate such a material model, the material behavior at such conditions must be investigated experimentally. Thus, the objective of this project is the development of a dynamic punch experiment that can utilize three dimensional digital image correlation measurements. Such an experiment allows researchers to validate their models under more complex stress states. A second objective is to experimentally investigate the plastic deformation behavior of precipitate hardened Inconel 718 at various strain rates and elevated temperatures and to use the data from such experiments to calibrate an accurate model of that behavior.

## **Chapter 2: Digital Image Correlation in Dynamic Punch Tests**

A dynamic punch test in which three dimensional DIC is used to measure the deformation of the rear surface of a thin disk specimen is introduced. A special die fixture is developed for connection to a compression split Hopkinson bar (SHB) apparatus. The specimens are clamped to this fixture, which is slotted along its axis such that the rear of the specimen is visible to two high speed cameras. The stereographic view from these cameras is used to measure full-field displacement using 3D-DIC. The slotted die fixture can also be mounted to a servo hydraulic load frame for quasi-static testing.. This work is an extension of the work on Ti-6Al- 4V performed by Jeremiah Hammer [6].

### **2.1 Introduction**

Historically, researchers have used the mechanical punch test to study the formability and failure of materials. A typical mechanical punch test involves driving a spherical –shaped punch into the surface of a sheet metal blank that is fixed around its circumference. The specimen experiences biaxial deformation until fracture or a reduction in the magnitude of the applied loading force is observed. A standardized punch test [7] (ASTM E 643-09) involves punching a 0.20 to 2.00mm thick specimen at slow velocities ranging from 0.08 to 0.4mm/s. The applied force and displacement of the formed cup are recorded for analysis. The data from such experiments is

traditionally used to compare formability of different materials and to generate forming limit diagrams for functions such as sheet metal forming.

More recently, researchers have used mechanical punch experiments to calibrate and validate numerical models and simulations used in forming operations and other applications involving plastic deformation and failure of materials. While simple models are traditionally calibrated using tension or compression tests, more advanced models require understanding of material behavior in more complex stress states. The stress state in punch experiments can be varied by changing punch geometry. For example, a hemispherical punch test results in a stress state of biaxial tension, while a blunt punch test results in a shear stress state. Furthermore, the thickness of the specimen can be manipulated to achieve a desired stress state [8]. These characteristics make mechanical punch tests an ideal way to validate those advanced models. Of particular interest are failure models that are written in terms of stress triaxiality and the Lode parameter [9, 10, 11, 12, 13, 14].

## **2.2 Punch Testing Literature Review**

Multiple authors have used quasi-static load frames to study ductile fracture of thin metallic specimens at low punch velocities. Lee, et al. [15] used a hemispherical punch to investigate the quasi-static behavior of several ductile thin sheet metals. Grytten , et al. [16] used a servo hydraulic load frame and measured the rear surface deformation of the thin specimen using a non-contacting laser gage and optical techniques in their study of thin 5083-H16 aluminum plates. These authors utilized four different punch geometries as well. Chen, et al. [17] measured full field strains on punch specimens that were tested in static experiments on a servo hydraulic load frame. Reu, et al. [18] measured specimen surface strains with 3D DIC in static tests on steel plates using a load frame.

Many authors have studied dynamic ductile fracture using pneumatic projectiles, drop towers, and compression split Hopkinson bars. Grytten, et al., [16] used a pneumatically fired projectile in a study of 5083-H116 aluminum under dynamic punch loading. The tethered projectile was instrumented with strain gages for measuring contact force and was fired at a velocities ranging from 4 to 16 m/s. In the same study on steel plates introduced above, Reu, et al. [18] performed dynamic experiments using a drop tower. Specimen strains were measured using 3D DIC. Walters [19] used a drop weight test rig to study ductile fracture of high strength steels at strain rates up to  $500\text{s}^{-1}$ .

Several researchers have modified the compression SHB to complete mechanical punch tests at high strain rates. Two groups of authors have used modified SHB setups to complete studies examining adiabatic shear bands. Zurek [20] used a custom designed fixture in dynamic punch experiments on pearlitic 4340 steel. Similarly, Roessig and Mason [21] modified a compression SHB by using only the striker and incident bars in their study involving 1018 steel, 6061-T6 aluminum, and Ti-6Al-4V. The plate specimen is clamped to a fixed support and penetrated by the incident bar, and the authors use a two-wave analysis to determine load and displacement for the experiment. These authors conducted a separate study in which they performed parallel numerical simulations to match the physical experiments [22]. Gilat and Seidt [23] deformed thin 2024-T351 aluminum disks in punch experiments on a compression SHB apparatus. This study utilized a hemispherical punch and a mechanical stop ring for limiting punch displacement into the specimen. This stop ring allowed for study of the failure mode evolution. Gaudillere, et al. [24] used a Hopkinson tube sensor in their work studying dynamic force transmitted from a punch to a work piece in a blanking operation. In this experiment, the punch specimen was mounted to a die that was fixed to the Hopkinson tube; and punch velocity was measured by a laser extensometer.

## 2.3 Experimental Setup

The Ti-6Al-4V punch specimen geometry is shown in Figure 2.1. The specimen is 50.8mm in diameter and 5.08mm thick. Six clearance holes for #6-32 screws are drilled in a 40.9mm diameter bolt circle, which allows six screws to clamp the specimen to the slotted die fixture.

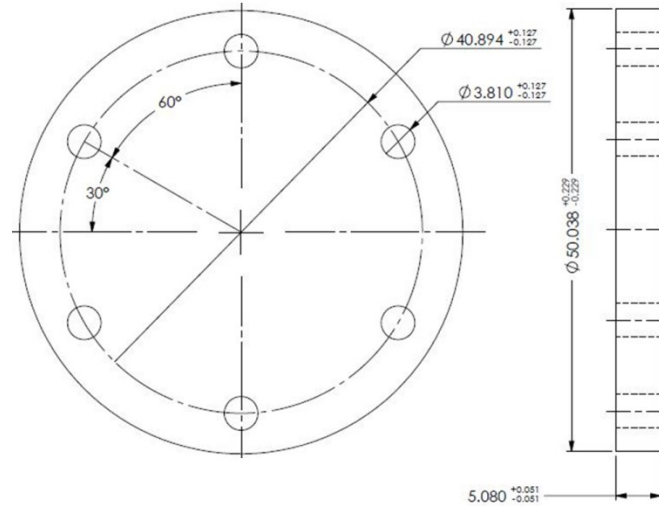


Figure 2.1: Ti-6Al-4V punch specimen geometry.

The thickness of the specimen was selected based on the results of simulations conducted in LS-DYNA. A close up view of simulation results with this geometry are shown in Figure 2.2. The results show the stress triaxiality over the failure path (outlined elements) through the specimen when loaded by a blunt punch with 20.0m/s initial velocity. The punch and holder in this simulation were modeled as rigid bodies, and the Ti-6Al-4V plate specimen was modeled using Johnson-Cook parameters from Hammer [6]. Additional specimens with thicknesses of 2.54mm and 7.62mm, respectively, were simulated as well. The 2.54mm results predicted specimen failure occurring along the inner diameter of the die fixture, rather than along the outer diameter of the punch. The results from the 5.08mm and 7.62mm specimens were very similar, predicting

desirable stress triaxiality at the failure point on the rear of the specimen. Thus, the 5.08mm thick specimen design was selected.

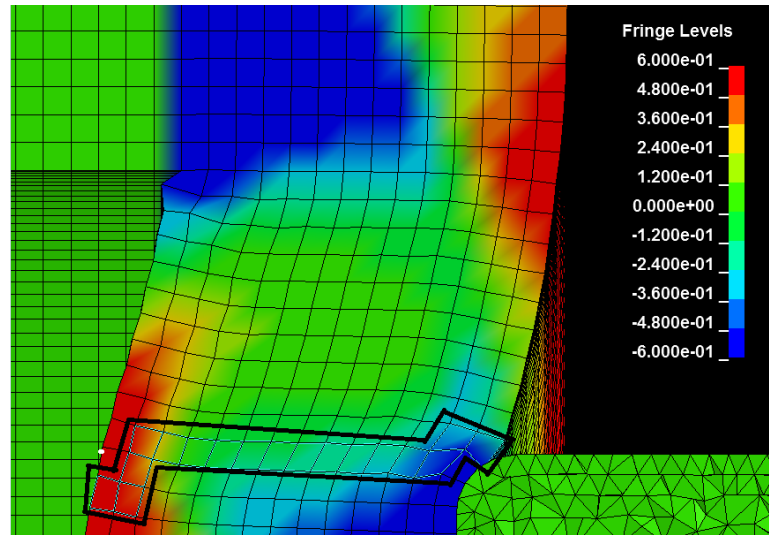
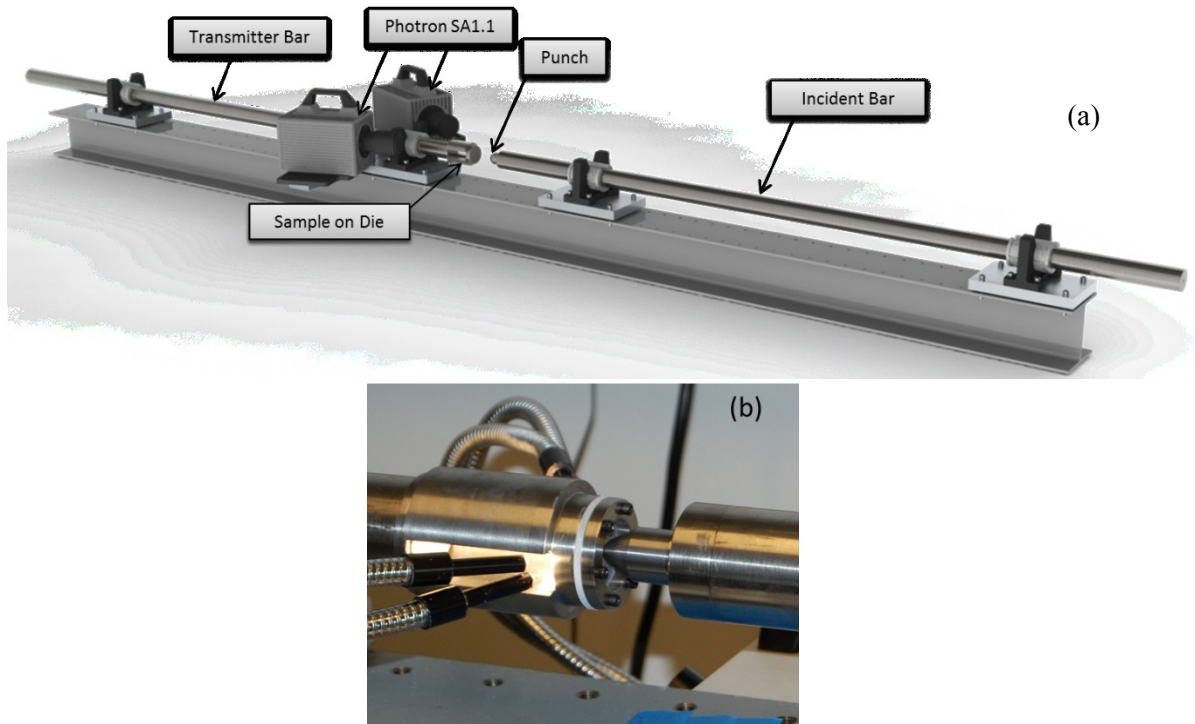


Figure 2.2: Stress triaxiality results from 5.08mm thick specimen LS-DYNA simulation.

### 2.3.1 The Dynamic Punch Test Setup

The experimental setup for the dynamic punch experiment is presented in Figure 2.3(a) and (b). The thin disk specimen is attached to the transmitter bar of the compression SHB apparatus, and the punch is connected to the incident bar. The specimen is clamped by its circumference to the tubular adapter (die), which has two narrow slots on opposing sides. These slots allow two cameras to be positioned such that they have a stereographic view of the rear surface of the punch specimen. The compression SHB apparatus used in this experiment is comprised of two 1930.4mm long bars made of 50.8mm diameter Ti-6Al-4V. The striker bar is a 774.7mm long bar made out of the same 50.8mm diameter Ti-6Al-4V as the incident and transmitter bars. This striker length generates a 320 $\mu$ s loading wave in the incident bar.



**Figure 2.3: Dynamic punch test - experimental setup: (a) sketch and (b) close-up of die fixture-specimen and punch.**

Tungsten carbide punches with three different tip geometries are used in these experiments and shown in Figure 2.4: Tungsten carbide punches: (a) Sharp (6.35mm radius), (b) Hemispherical (12.17mm radius), (c) Blunt. Figure 2.4. The first (Figure 2.4(a)) is conical with a 6.35mm radius nose. The second (Figure 2.4(b)) is hemispherical with a 12.17mm radius. The third (Figure 2.4(c)) is blunt with a 0.79mm corner radius.

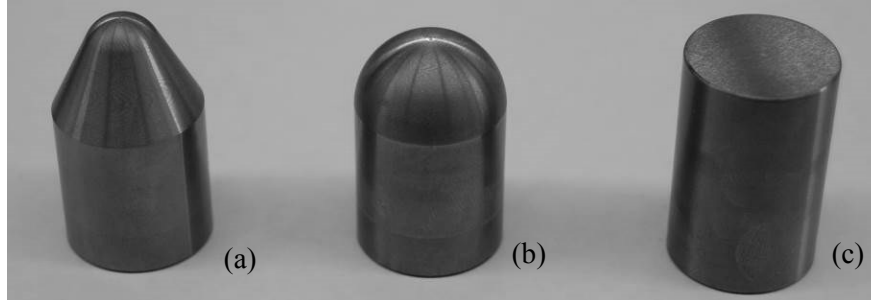


**Figure 2.4: Tungsten carbide punches: (a) Sharp (6.35mm radius), (b) Hemispherical (12.17mm radius), (c) Blunt.**

Prior to a test, the punch is moved such that it contacts the front surface of the specimen. MoS<sub>2</sub> grease is used to lubricate the contact surface between the punch and the specimen. The striker bar is fired at a velocity of roughly 16 m/s, which generates an incident wave of approximately 378kN. This wave pushes the punch into the specimen. Images for three dimensional DIC measurements of the rear surface of the specimen are recorded by a synchronized pair of Photron SA1.1 cameras running at 100,000 frames per second at 192 pixel by 192 pixel resolution. The incident and transmitted waves are measured by strain gages at the midpoint of each bar. The contact force between punch and specimen is calculated from the transmitted wave. The die fixture is designed to minimize its effect on the transmitted wave.

The die fixture is designed such that the wave generated by the loading force around the clamped disk specimen circumference, which reacts to the applied punch force, propagates through the fixture into the transmitter bar smoothly with minimal disturbances. This is accomplished by manipulating the cross-sectional area of the slotted die fixture such that the mechanical impedance along its length is constant and equal to that of the bars in the SHB apparatus. Mechanical impedance is:

$$Z = \rho A c \tag{1}$$

where  $\rho$  is the material density,  $A$  is the cross-sectional area, and  $c$  is the wave speed in the material. It is important that the impedance remain constant because classical analysis of the waves in a compression SHB apparatus is based on the assumption that the impedance of the incident and transmitter bars is constant between the specimen contact surface and the location where the waves are measured. If this is true, then the force measured at the strain gage on the transmitter bar will correspond to the contact force at the punch-specimen interface.

To achieve this design goal, the geometry of the die fixture was modified iteratively and simulated with the entire compression SHB apparatus in LS-DYNA. The die fixture was attached to the transmitter bar and placed in contact with the incident bar with no specimen. The simulations were repeated with various geometries until a desirable transmitted pulse was predicted. Solid geometry was used as a baseline for comparison. The two geometries are presented in Figure 2.5(a), and their simulation results are presented in Figure 2.5 (b).

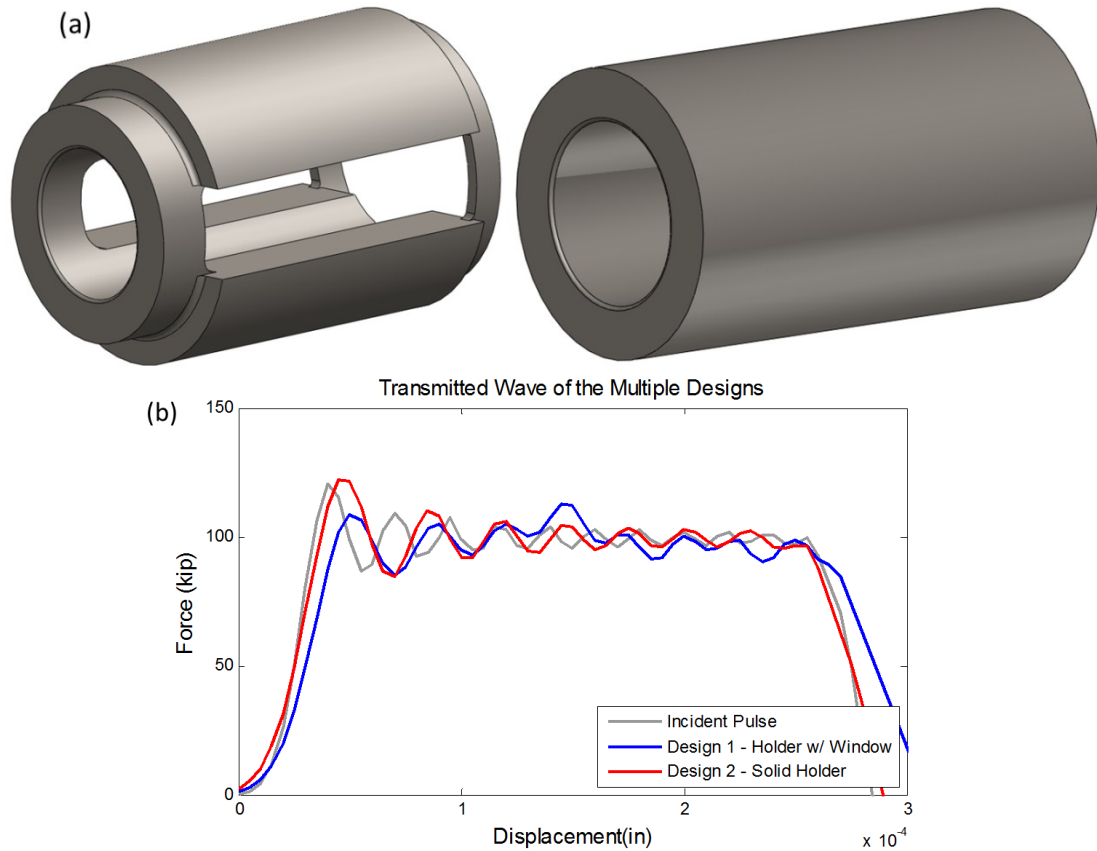


**Figure 2.5: (a) Slotted die fixture (left) and solid holder design (right), (b) Comparison of transmitted wave to incident pulse**

Once the geometry was finalized, the fixture was fabricated and tested physically. The results of the simulation and physical experiment are compared in Figure 2.6. The simulated and measured waves are nearly the same except for a small reflection of the loading wave back into the incident bar in the physical experiment. Such a phenomenon is likely the result of an imperfect contact at the incident bar – slotted die fixture interface. There is also a roughly 25 $\mu$ s delay in the arrival time of the transmitted wave at the strain gages on the transmitter bar in the experiment relative to the simulation. The imperfect contact surface, differences in density, or differences in elastic modulus between simulation and actual material can explain this delay.

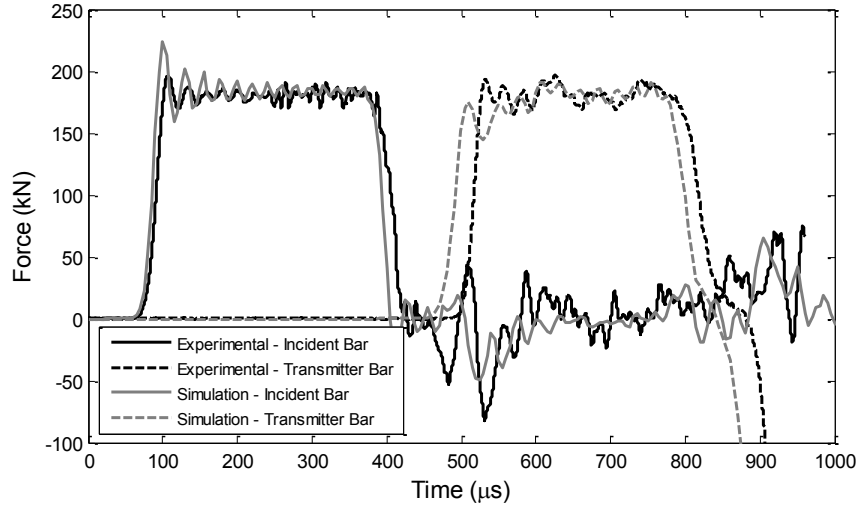


**Figure 2.6: Simulated and experimental wave propagation through slotted-die fixture**

### 2.3.2 The Quasi-Static Punch Test Setup

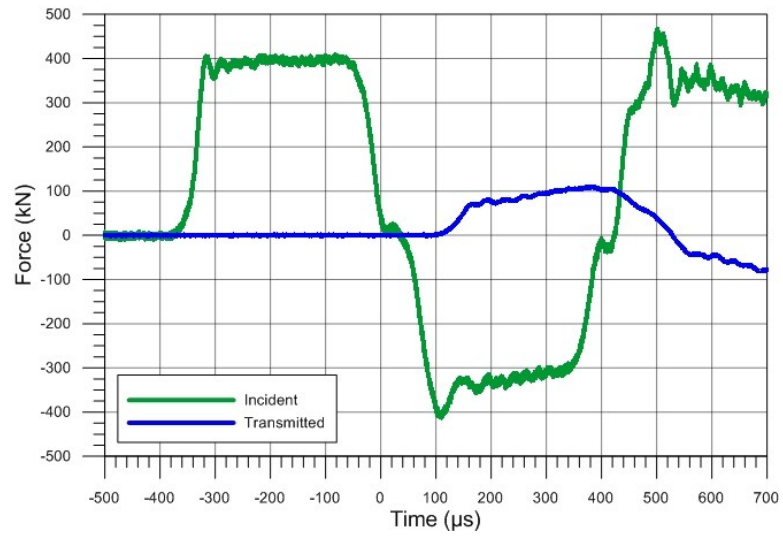
The experimental set-up for the quasi-static punch test is shown in Figure 2.7. The die-fixture-disk assembly used in the dynamic tests is attached through a connecting rod to the load cell of a servo-hydraulic load frame. Two load frames are used in the quasi-static experiments: an 89kN load frame was used in quasi-static tests with the sharp punch, and a 245kN load frame was used in quasi-static tests with the hemispherical and blunt punches. The punch sits on a connecting rod mounted to the load frame's actuator. Point Gray GRAS-20S4M-C cameras are positioned with a view through the slots in the die fixture and record the deformation of the rear surface of the specimen at 4.0 frames per second with a 1600 x 1200 pixel resolution. Contact force is measured by the load cell, and punch motion is measured using the LVDT of the hydraulic load frame. The actuator velocity in the quasi-static punch experiments is 0.023mm/s.



**Figure 2.7: Quasi-static punch test setup**

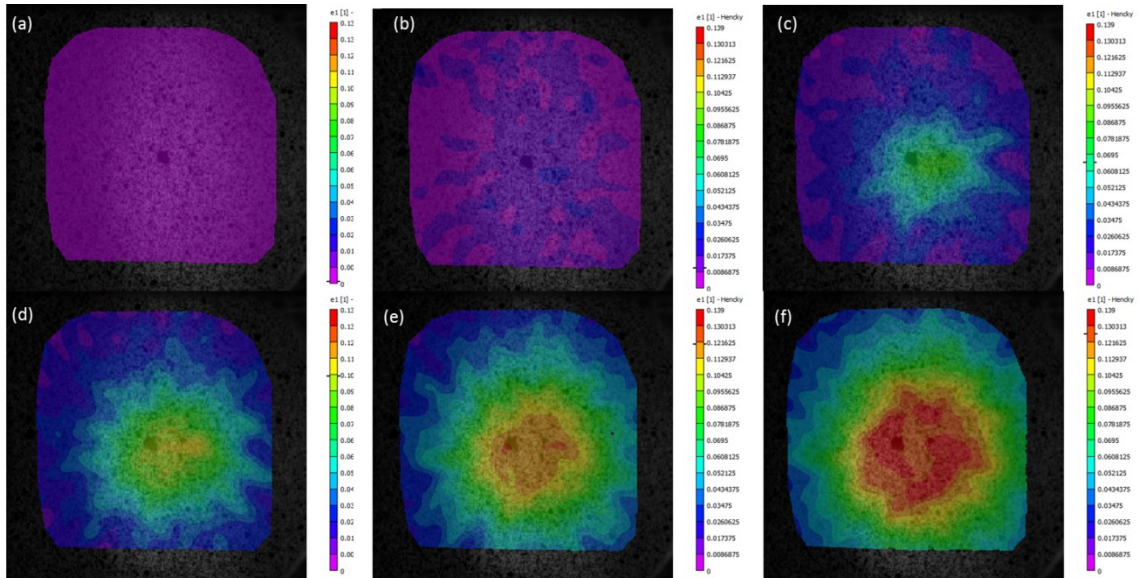
## **2.4 Experimental Results & Discussion**

The dynamic test results for a test with the hemispherical punch are shown in Figure 2.8 – Figure 2.10. The striker projectile impact velocity is 17.6m/s in this experiment, and the elastic waves recorded by the incident and transmitter bars are shown in Figure 2.8. The incident wave amplitude is 400kN, and the transmitter bar wave shows the contact force reaches a maximum of 110kN.



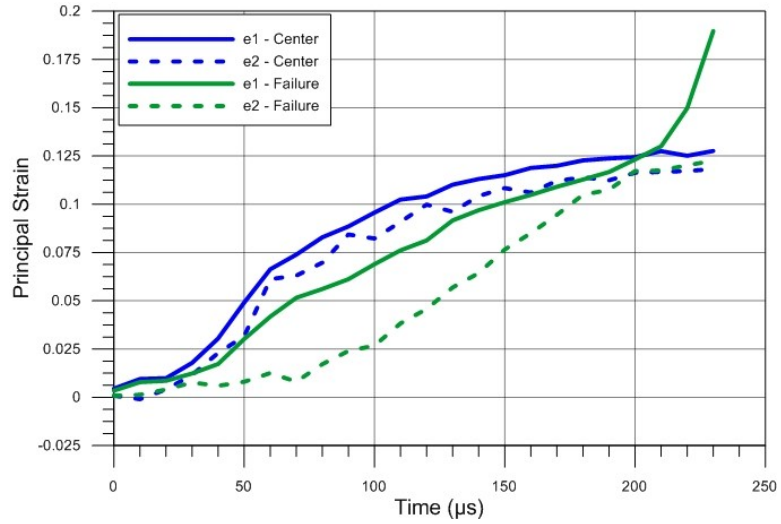
**Figure 2.8: Elastic waves recorded for a dynamic punch test using the hemispherical (12.17mm radius) punch**

Figure 2.9 shows maximum principal strain contours on the rear surface of the specimen from six frames during the experiment. Figure 2.9 (a), (b), (c), (d), (e), and (f) show the specimen immediately prior to loading, 40, 90, 130, 180, and 230 $\mu$ s after loading initiates, respectively. Figure 2.9 (f) specifically corresponds to the moment just prior to fracture on the rear surface of the specimen.



**Figure 2.9: Maximum principal strain contours for a dynamic test with the hemispherical punch at (a)  $0\mu\text{s}$ , (b)  $40\mu\text{s}$ , (c)  $90\mu\text{s}$ , (d)  $130\mu\text{s}$ , (e)  $180\mu\text{s}$ , (f)  $230\mu\text{s}$  after load initiation**

The data in Figure 2.10 comes from point data extracted from the DIC measurements. The history of the principal strains at the specimen center point and the point where fracture is observed are compared. In an ideal test, the center point is in biaxial tension. Figure 2.10 shows that the two principal strains at the failure point are nearly the same at failure. The failure point is offset slightly from the center point, and the strain state is not biaxial tension until just prior to failure. Such data, when combined with the contact force history, is valuable for calibrating fracture models and validating simulations.



**Figure 2.10: Principal strain evolution for specimen center point (blue) and failure point (green) in dynamic punch test with hemispherical punch geometry**

Results for a quasi-static hemispherical punch test are shown in Figure 2.11 – Figure 2.13. The force and displacement histories are shown in Figure 2.11. The maximum contact force between punch and specimen is 85kN, and the displacement at this time is approximately 2.8mm.

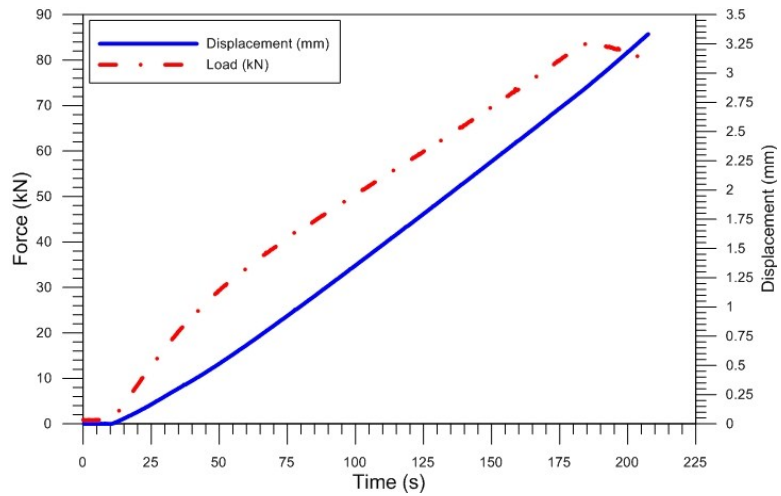


**Figure 2.11: Force and displacement history for a quasi-static punch test using the hemispherical punch.**

Figure 2.12 shows six images of maximum principal strain data calculated using DIC during the duration of the quasi-static punch test. Figure 2.12(a), (b), (c), (d), (e), and (f) show the specimen

at the moment before loading, 32.25, 70.50, 105.50, 140.76, and 176.02 seconds after loading begins, respectively. The final frame corresponds to the moment just prior to when fracture is observed in the experiment. Inspection of these contours shows that the maximum strains occur in the same location as those in the dynamic case.

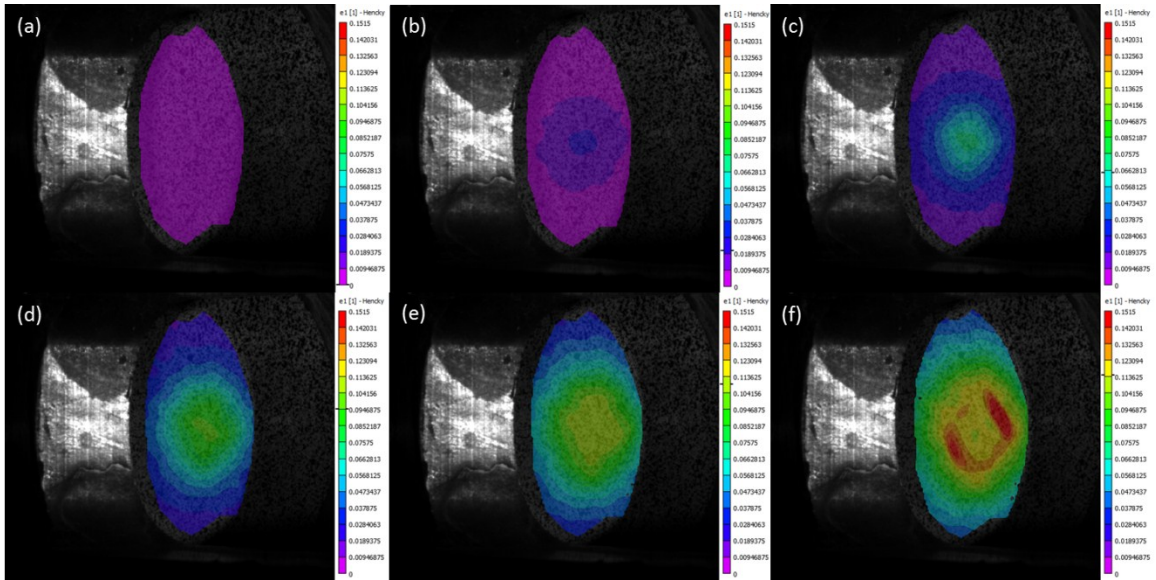


**Figure 2.12: Maximum principal strain contours for a quasi-static punch experiment using the hemispherical punch. Images correspond to times (a) 0s, (b) 32.25s, (c) 70.50s, (d) 105.50s, (e) 140.76s, (f) 176.2s after load initiation.**

The history of the principal strain components at the center and fracture points of the specimen and the applied load are shown in Figure 2.13. The center point is nearly in biaxial tension throughout the whole test, but the failure point deviates from biaxial strain significantly in the first half of the experiment.

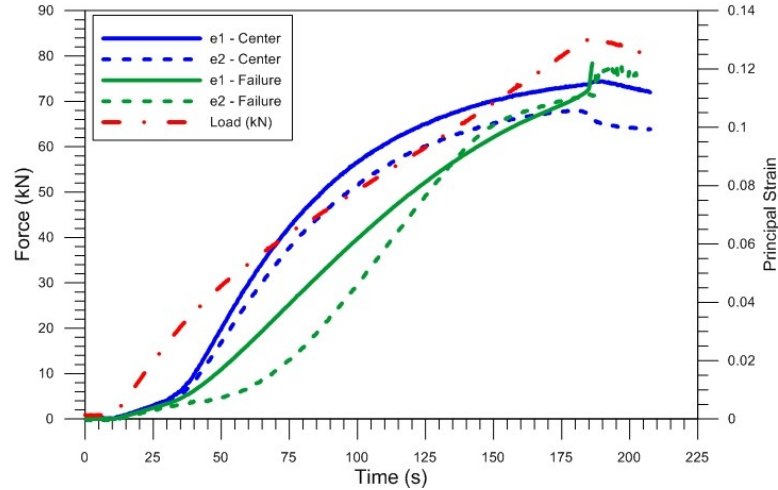


**Figure 2.13: Principal strain and applied contact force history - quasi-static punch experiment with hemispherical punch**

Contact force versus displacement results from the Ti-6Al-4V punch testing series are summarized in Figure 2.14. These data come from a total of 18 punch experiments: three dynamic and three quasi-static tests conducted using each of the three punch geometries. Contact force is calculated using the transmitted wave in the dynamic tests and data from the load cell in the quasi-static tests. Displacement corresponds to the displacement of the center point of the rear surface of the specimen as measured with DIC. In static tests, this displacement is the absolute displacement measured using the image techniques. It is assumed that the slotted die fixture and hydraulic frame are rigid, meaning the specimen's circumference does not move during the experiment. In dynamic tests, the specimen's circumference moves with the transmitter bar. This motion is included in the DIC measurements. To correct for this, the displacement of the transmitter bar is calculated from the transmitted wave and is subtracted from the DIC measured displacement. Force magnitude is influenced by the punch shape. The peak force in static experiments is 68kN, 85kN, and 210kN for sharp, hemispherical, and blunt punch geometries, respectively. In dynamic experiments, this peak contact force is 83kN, 105kN, and 235kN for

sharp, hemispherical, and blunt geometries, respectively. The force magnitude is also affected by the loading rate. Peak contact forces in the dynamic case are 22%, 24%, and 12% greater than static forces for the sharp, hemispherical, and blunt punch respectively.

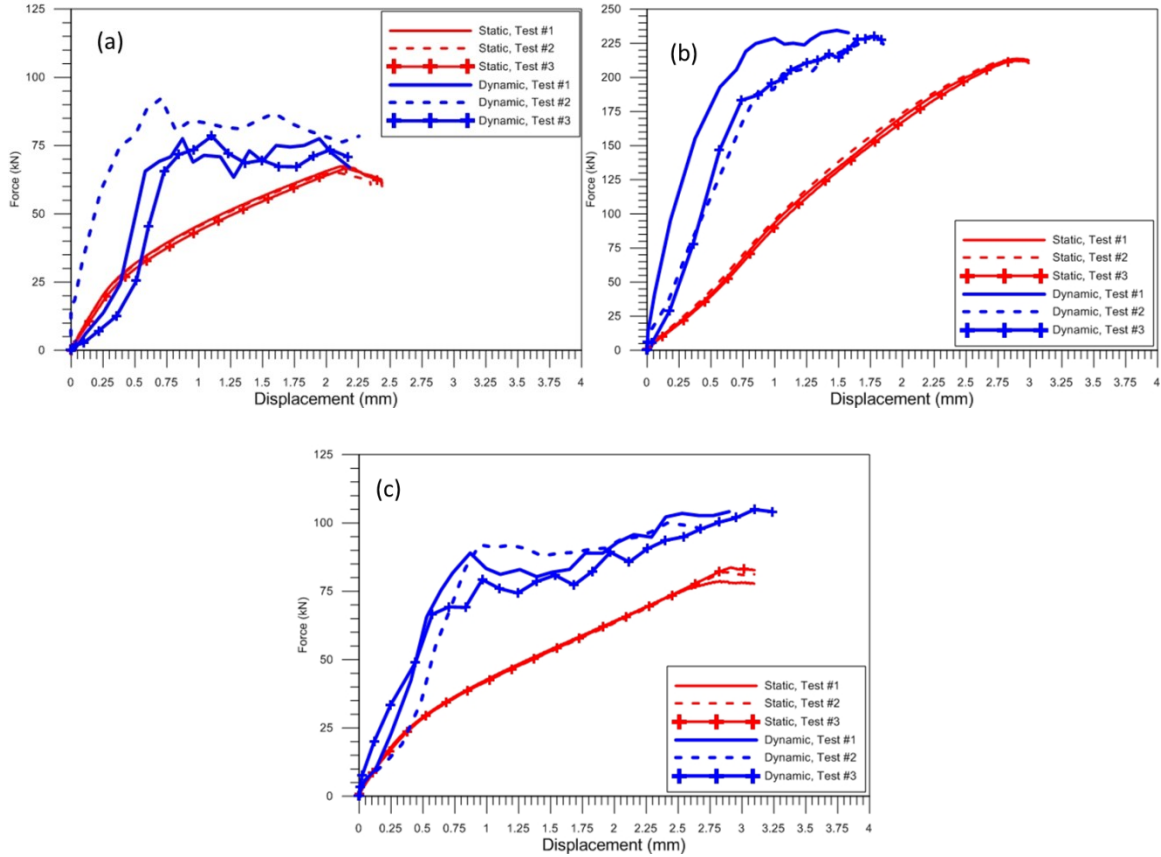


**Figure 2.14: Static and dynamic contact force versus displacement data for: (a) Sharp, (b) blunt, and (c) hemispherical punch geometries**

The evolution of equivalent Hencky strain,  $\bar{\epsilon}$ , and the ratio of the two principal strains,  $\alpha$ , is useful for creating a strain-based failure locus for Ti-6Al-4V. Data from DIC measurements at the point fracture is first observed is used to calculate these variables, using the following brief derivation.

The equivalent Hencky strain increment is defined as:

$$d\bar{\varepsilon} = \sqrt{\frac{2}{3}d\varepsilon_{ij}d\varepsilon_{ij}} \quad (2)$$

The Hencky strain tensor is defined by:

$$\varepsilon_{ij} = \frac{1}{2}\ln(B_{ij}) \quad (3)$$

where  $B_{ij}$  is the left Cauchy Green deformation tensor. Assuming the material is incompressible, deformation must be isochoric, and the trace of the Hencky strain tensor is equal to zero [25].

Thus, the third principal strain is determined from equation (4),

$$\varepsilon_1 + \varepsilon_2 + \varepsilon_3 = 0 \quad (5)$$

And equations (2) and (5) can be combined to find the equivalent Hencky strain. The principal strain ratio is defined as

$$\alpha = \frac{\varepsilon_1}{\varepsilon_2} \quad (6)$$

This strain evolution is presented in Figure 2.15 (a) for experiments conducted using the sharp (6.35mm radius) punch, and Figure 2.15 (b) for experiments conducted using the hemispherical punch. Data from the blunt punch is not included because the failure point is not visible in test images used in DIC measurements. The principal strain ratio ranges from 0.5 to 0.96 in experiments conducted with the sharp punch. This ratio ranges from 0.2 to 0.97 in those experiments using the hemispherical punch. Failure occurs at  $\alpha$  values between 0.65 and 0.8 in sharp punch experiments and between 0.61 and 0.85 in hemispherical punch experiments.

Equivalent failure strain of sharp punch tests averages 0.339 in the static case and 0.342 in the dynamic case. Equivalent failure strain of hemispherical punch tests averages 0.284 in the static case and 0.312 in the dynamic case. These data suggest equivalent failure strain is mildly strain rate dependent.

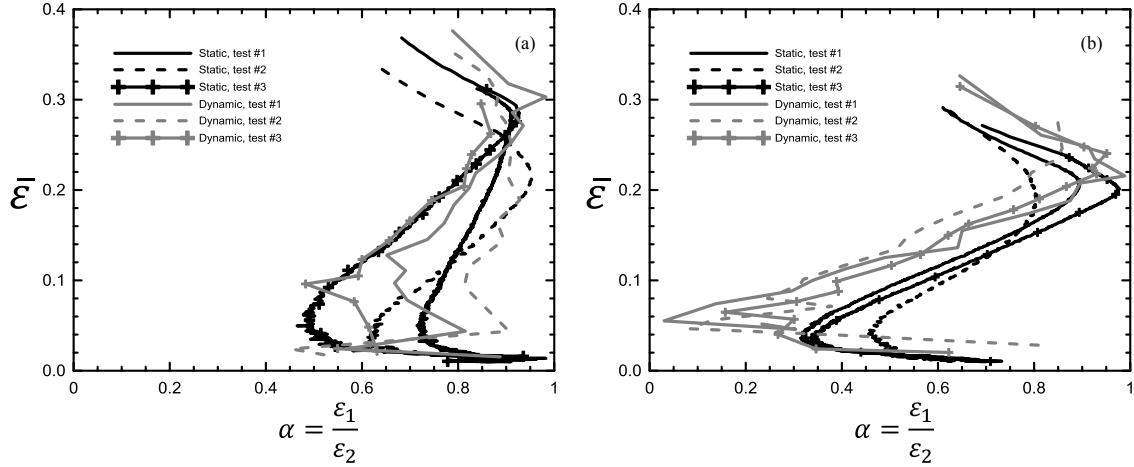


**Figure 2.15: equivalent strain versus principal strain ratio data for (a) sharp punch and (b) hemispherical punch experiments.**

Prior work [13] has shown that the principal strain ratio,  $\alpha$ , can be correlated to stress triaxiality under plane strain conditions. The data shown in Figure 2.15(a) and (b) could be used to build a stress state based failure locus for thin specimens for which the plane stress assumption is valid. The Ti-6Al-4V disk specimens tested here are likely too thick for the plain stress assumption to hold, but data points for a stress-state based failure locus could be found by running parallel numerical simulations. Another use for these is in Ti-6Al-4V material model validation.

## 2.5 Summary and Conclusions

A dynamic punch test using 3D-DIC is introduced that utilizes a custom designed slotted die fixture to offer two high speed cameras a stereoscopic view of the rear surface of a thin metallic disk specimen. In the dynamic experiment, this die-fixture-specimen assembly is mounted to the transmitter bar of a compression split Hopkinson bar apparatus and a tungsten carbide punch is mounted to the incident bar. The die fixture is designed specifically to minimize the distortion of the loading wave as the wave passes through the fixture, which allows the SHB wave data to be analyzed using the same wave analysis techniques as a dynamic compression test. The punch

specimen thickness is selected based on the desired stress triaxiality results from a series of simulations conducted in LS-DYNA. The punch fixture is also used in quasi-static experiments using servo hydraulic load frames. Detailed experimental results are presented for dynamic and quasi-static experiments conducted using hemispherical punch geometry. Force-displacement data is presented for experiments using three different punch geometries in both dynamic and quasi-static experiments. These data suggest that punch shape and loading rate affect peak contact force. Analysis of the equivalent strain using DIC data at the failure point suggests that equivalent failure strain is mildly strain rate dependent. 3D-DIC data from such experiments can be valuable in calibrating and validating advanced material models and studying ductile failure of materials under more complex stress states than those achievable using simple axial tension or axial compression experiments.

## **Chapter 3: Plastic Deformation Behavior of Precipitate Hardened**

### **Inconel 718**

#### **3.1 Introduction**

Inconel is a nickel-chromium based superalloy, first developed for use in jet engines in the 1940s. Its high strength, fatigue, creep, and rupture properties make it useful for a variety of applications. Inconel is commonly found in advanced aerospace and automotive applications, such as turbines and turbochargers, where good strength is required in extreme environments. Some more notable uses of the superalloy include the thrust chamber of the F1 rocket engine, which powered the Apollo space program's Saturn V rocket; and the engine manifold of the Merlin rocket, which is used by the Space-X Falcon 9 launch vehicle.

#### **3.2 Inconel 718 Literature Review**

The dynamic plastic flow behavior of Inconel 718 has been studied over a variety of elevated strain rates using ballistic experiments and split Hopkinson bars. DeMange, et al. [26], studied the dynamic behavior of Inconel 718 in both the annealed and precipitation hardened conditions. They used high speed penetration tests as well as dynamic compression tests to investigate how changes in material microstructure affected dynamic response. Sciuva, et al. [27], conducted impact tests on cast Inconel 718 plates at varying velocities to investigate structure response in a penetration event and obtain a dynamic characterization of the material. These authors generated a ballistic limit curve by performing a numerical correlation with the experimental results. Pereira and Lerch [28] studied the effects of different heat treatments on the ballistic impact behavior of

Inconel 718. Their work examined the material at two different annealing conditions and an aged condition. Kobayashi, et al. [29], studied the plastic deformation behavior of Inconel 718 in shear over a range of strain rates from  $0.01\text{s}^{-1}$  to  $3000\text{s}^{-1}$ . Low rate tests were performed on a quasi-static torsion machine, and high rate tests were performed using a torsional split Hopkinson bar.

The study of Inconel 718 under elevated temperature conditions has focused on the material's behavior in two situations: 1) superplastic deformation, which is important for the manufacturing of Inconel 718 parts, and 2) plastic deformation, which is important for behavior of Inconel 718 parts used in mechanical systems. Zhang, et al. [30], developed a set of constitutive equations to represent the superplastic behavior of Inconel 718 based on a hyperbolic sine relation. Xue, et al. [31], conducted superplastic tests of Inconel 718 at strain rates between  $10^{-4}$  and  $10^{-1}\text{s}^{-1}$  and temperatures between 940 and 1020 °C. Yoo, et al. [32], investigated superplastic behavior of Inconel 718 via a free bulging test at 980 °C. Of more interest to this work are studies conducted on Inconel 718 in a non-superplastic state. Zhang, et al. [33], investigated the effect of different phase contents in aged Inconel 718 deformation under tensile loading at 950 °C. This study also investigated the fracture characteristics of those specimens. Thomas, et al. [34], studied the behavior of Inconel 718 at high temperatures in the context of hot forming operations. These authors performed experiments at various quasi-static strain rates and temperatures of 1080, 1050, 1000, 950, and 900 °C in uniaxial compression.

### **3.3 Plastic Deformation of Precipitate Hardened Inconel 718: Experimental Procedures and Techniques**

Techniques for testing uniaxial tension specimens in quasi-static, dynamic, and elevated temperature configurations and the analysis of data from such tests are described. Uniaxial compression testing techniques in quasi-static and dynamic conditions are presented along with

data analysis. Finally, DIC, a technique that allows for measurement of full-field surface displacements and the calculation of full-field strains on the visible surface of the specimen, is described.

### 3.3.1 Tension Experiments

Tension tests are completed on Inconel 718 to observe plastic deformation behavior over a wide range of strain rates, temperatures, and specimen orientations. The experimental test plan for the tension experiments is shown in Table 3.1. Strain rate sensitivity is studied with tests on specimens fabricated in the rolling direction of the plate. These tests are performed at strain rates of  $1 \times 10^{-4}$ ,  $1 \times 10^{-2}$ , 1.00, 500, and  $2000 \text{ s}^{-1}$ . Additionally, tests are conducted at  $1.00 \text{ s}^{-1}$  on specimens fabricated in three additional orientations:  $+45^\circ$  from rolled, transverse, and  $-45^\circ$  from rolled. Finally, tests are conducted on rolled direction specimens at four elevated temperatures: 200, 400, 600, and  $800^\circ\text{C}$ .

Test No.	Testing Apparatus	Strain Rate (1/s)	Specimen Orientation	Temperature ( $^\circ\text{C}$ )
1	Hydraulic Load Frame	1.00E-04	Rolled	Room Temp
2		1.00E-02		
3		1.00E+00		
4	Tension SHB	5.00E+02		
5		2.00E+03		
6	Hydraulic Load Frame	1.00E+00	45 from Rolled	
7			Transverse	
8			- 45 from Rolled	
9			Rolled	200
10				400
11				600
12	800			

**Table 3.1: Experimental outline for plastic deformation testing of precipitate hardened Inconel 718 in tension loadings.**

### 3.3.1.1 Tension Specimen Design and Fabrication

All specimens are machined from 12.7mm thick precipitate hardened Inconel 718 plate stock. The material was obtained from Allegheny Ludlum in the annealed condition. The plates were then heat treated using the heat profile described in Table 3.2.

Phase	Description	Time (hrs)
1- Temp Hold	718 °C Constant Temperature	8
2 – Furnace Cool	Furnace Cool 55°C per hour	1.76
3 – Temp. Hold	621 °C Constant Temperature	8

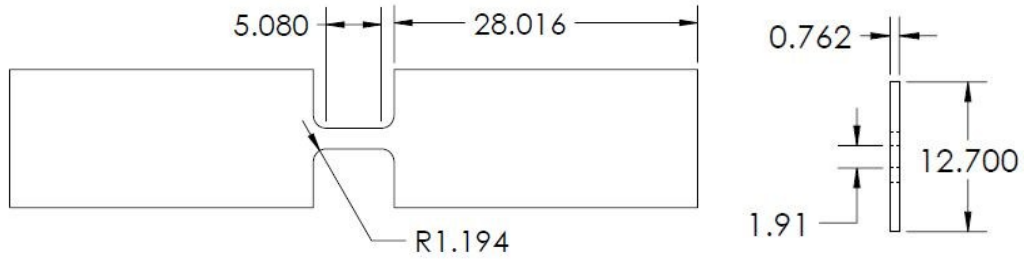
**Table 3.2: Precipitate hardening heat treatment profile.**

The material composition of this plate is summarized in Table 3.3. Tests were conducted on specimens with identical gage section geometries. Minor modifications were made to the dynamic and high temperature test specimens in order to attach those specimens to the testing equipment.

C	Mn	P	S	Si	Ni	Cr	Mo	Co	Cu	Al	Ti	Cb	B	Fe	Ta
.048	.083	.008	.0001	.072	52.60	18.32	2.87	.20	.034	.54	1.02	4.94	.0029	19.25	.010

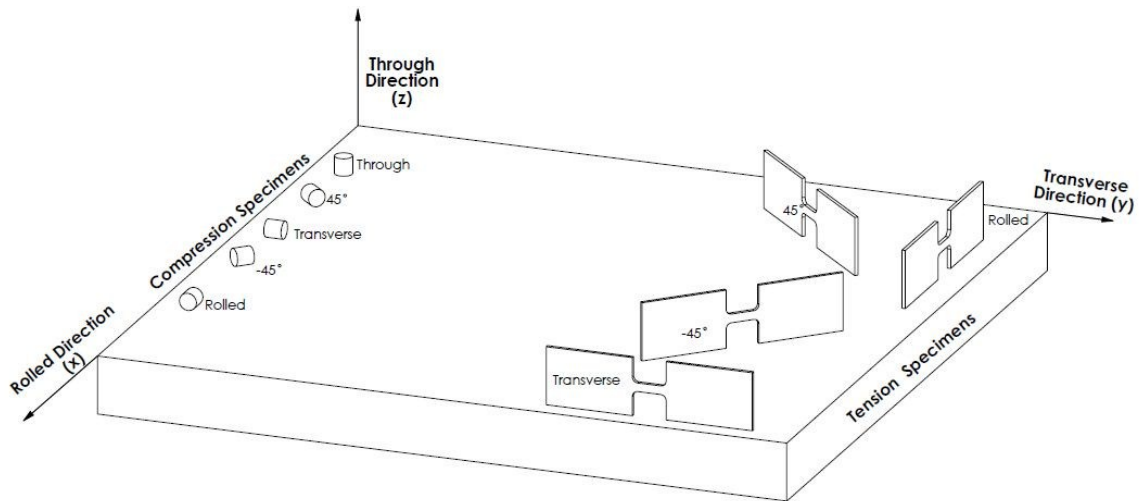
**Table 3.3: Material composition of 12.7mm plate stock**

The geometry for quasi-static, room temperature tension tests is shown below in Figure 3.1. The size of the gage section, which is unchanged across the entire set of tension experiments, is limited by the characteristics of the dynamic test apparatus. The specimen for the split Hopkinson bar must be small to ensure that force equilibrium occurs and that the transmitted force is low. If the transmitted force is not significantly lower than the incident force, the specimen will fail to deform. Generally, the desired transmitted force for the tension SHB apparatus used is 2200 N. For an expected peak specimen stress of 1380MPa, the 1.91mm x 0.76mm cross-sectional geometry results in a maximum transmitted load just under the limit at 2000N. The length of the gage section is 5.08mm; and the full specimen length is 63.5mm, which gives plenty of surface area on each end for the servo-hydraulic load frame grips.



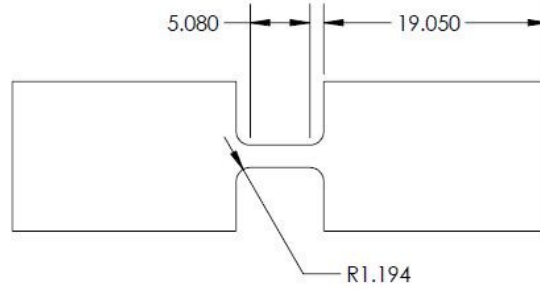
**Figure 3.1: Tension Specimen Geometry.**

Figure 3.2 diagrams the orientations of quasi-static tension specimens used to study anisotropy in the material. The X axis is the direction that the 12.7mm precipitate hardened Inconel 718 plate stock was rolled, and Y axis aligns with the direction transverse to rolling. Specimens are fabricated in the rolled direction, +45° to rolled direction, transverse direction, and -45° to rolled direction.



**Figure 3.2: : Specimen Orientations in 12.7mm Inconel 718 plate**

The geometry for dynamic, room temperature tension tests is presented in Figure 3.3. The gage section is identical to that of the low rate specimens. The overall specimen length, however, is shorter (45.57mm). In this case the specimen ends are shortened to match the depth of the adapters used to connect the dynamic tension specimens to the tension SHB.



**Figure 3.3: Dynamic tension geometry.**

The geometry for quasi-static tension experiments at elevated temperatures is shown in Figure 3.4. The gage section matches that of the other specimens in the tension series. The length of the specimen is again 63.5mm, and there are two 4.50mm diameter through holes located 7.62mm from each end of the specimen. These holes are used with the high-temperature tension fixture; described in the following section; that uses pins and bushings to hold the specimen.

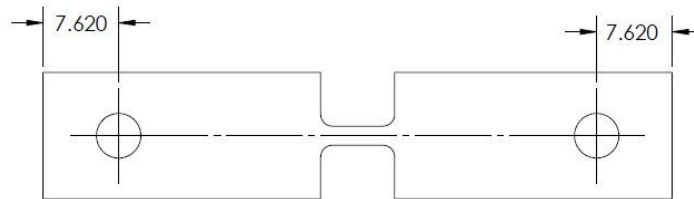


**Figure 3.4: Elevated temperature tension specimen geometry.**

### **3.3.1.2 Quasi -static Tension Experiments**

The experimental setup for quasi-static tension experiments is presented in Figure 3.5. Tests are conducted using an 89kN servo-hydraulic load frame. The specimen is gripped by hydraulic clamps at either end. The upper grip is fixed to an 89kN load cell, which is fixed to the load frame crosshead. The lower grip is fixed to the actuator head. The motion of the actuator head is recorded by a linear variable differential transformer (LVDT). Two cameras are positioned less than 0.5m from the specimen, on the same vertical plane, such that they are focused on the same

point on the specimen with roughly  $12^\circ$  to  $15^\circ$  angle between them. Point Gray Research GRAS-20S4M-C cameras, with a  $1624 \times 1224$  pixel resolution, are used in experiments at nominal strain rates of  $1.0 \times 10^{-4} \text{ s}^{-1}$  and  $1.0 \times 10^{-2} \text{ s}^{-1}$  at 1/15 and 10 frames per second, respectively. Photron MC2 cameras, with a resolution of  $512 \times 512$  pixels, are used in experiments at a nominal strain rate of  $1.0 \text{ s}^{-1}$  at a frame rate of 2000fps. Schneider 30mm lenses are used in all tests conducted on the load frame.

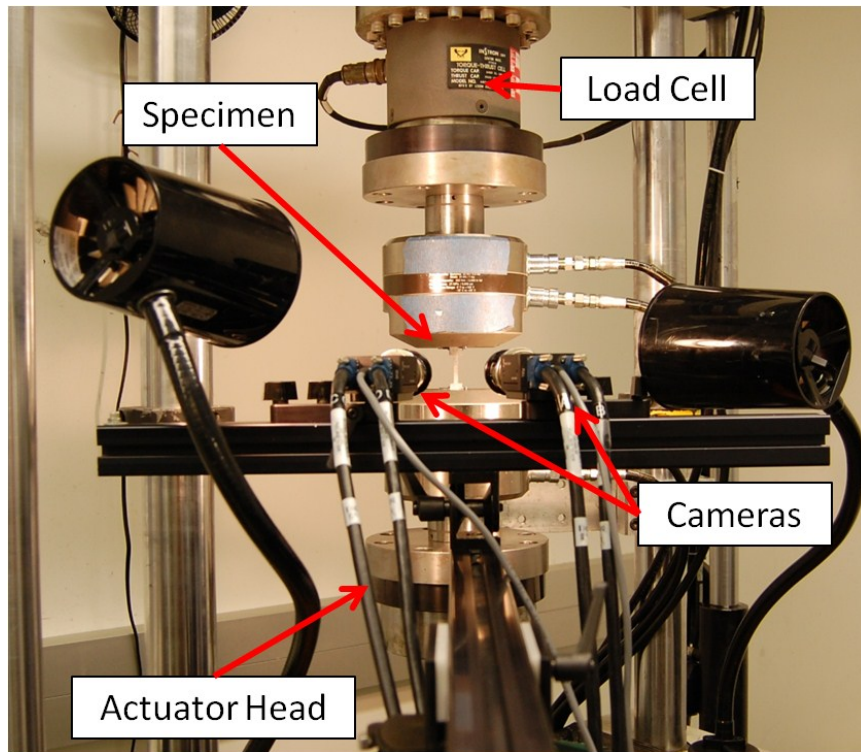


**Figure 3.5: Quasi-static tension setup**

Tests on the servo-hydraulic load frame are carried out by moving the actuator downwards in displacement control at a constant velocity, recording the load and displacement response through the load cell and LVDT, and taking photographs of the deforming specimen throughout the entire experiment using the cameras. The actuator of the load frame is controlled using an MTS FlexTestSE through 793 control software. The cameras are operated using Correlated Solution

VIC Snap. The control software is programmed to record the time, stroke, and load during the duration of the experiment. The camera frame rate is set to ensure approximately 500 images are taken of the test event. These images are processed with Correlated Solutions VIC-3D 2009 DIC software to calculate displacements on the surface of the specimen.

Engineering stress and engineering strain are calculated from measurements of the specimen dimensions and the recorded loads and displacements from the experiment. The engineering strain is calculated using the following formula:

$$\varepsilon_E = \frac{\Delta l}{l_o} \quad (7)$$

where  $\Delta l$  is the displacement measured using DIC and  $l_o$  is the gage length. The engineering stress is calculated using equation (8).

$$\sigma_E = \frac{F}{wt} \quad (8)$$

where  $F$  is the loading force,  $w$  is the gage width, and  $t$  is the gage thickness. These two values can be converted to true strain and true stress using equations 9 and 10.

$$\varepsilon_T = \ln(1 + \varepsilon_E) \quad (9)$$

$$\sigma_T = \sigma_E(1 + \varepsilon_E) \quad (10)$$

### 3.3.1.3 *Dynamic Tension Experiments*

A diagram of the tension SHB used for dynamic tests is shown in Figure 3.6. Each end of the specimen is bonded into a cylindrical adapter, which is then bound to the ends of the incident and transmitter bars using JB Quick 2-part epoxy (see Figure 3.7). Both the incident and transmitter bars are 12.7mm diameter 7075-T651 aluminum. The incident bar is 3.68m long. The transmitter bar is 1.83m long. Three full wheatstone bridges, labeled A, B, and C, are used to record the stress waves during the dynamic tension test. The loading wave is created by rapidly releasing a stored tensile force. The incident bar is clamped in front of Gage A. The pulley is used to put a

tensile load on the section of the bar in front of the clamp. A fracture pin is used in the clamp. This pin is designed to fracture at a predetermined load. When that load is applied the pin breaks, and the tensile loading wave ( $\epsilon_i$ ) is released down the incident bar. When it reaches the specimen, the specimen is plastically deformed by the relative motion between the bars. Part of the loading wave is transmitted through the specimen until failure ( $\epsilon_t$ ), and part of it is reflected ( $\epsilon_r$ ) into the incident bar. The transmitted wave is recorded by strain gage C on the transmitter bar, while the incident and reflected waves are measured by gages A and B on the incident bar. These gages are powered by a 15V excitation, and signals are sent through a preamplifier before being recorded on a Tektronix oscilloscope.

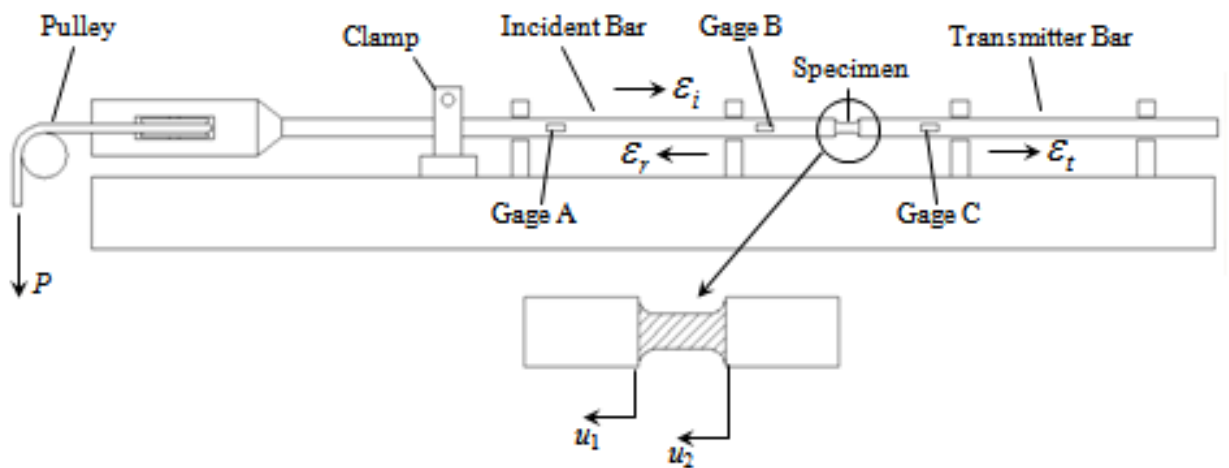
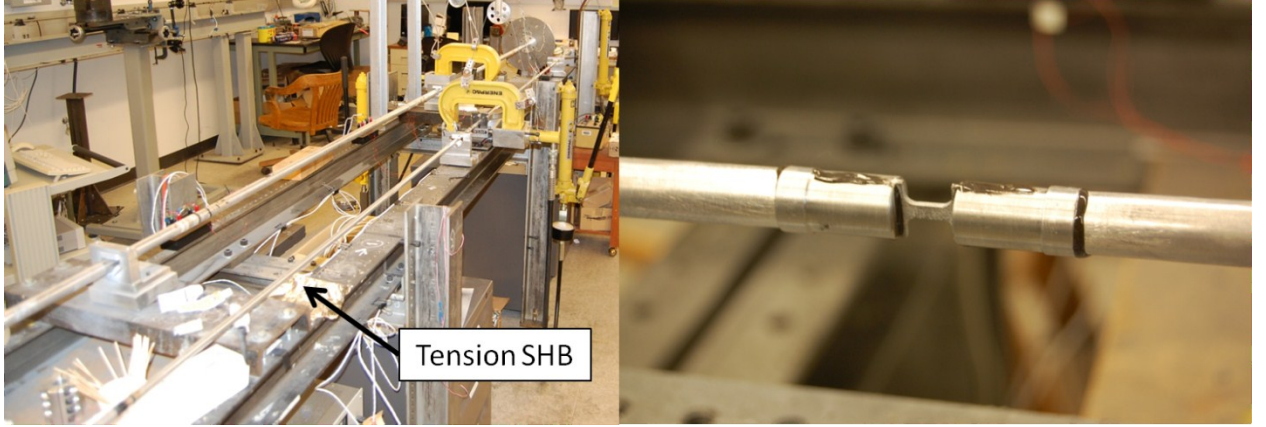


Figure 3.6: Tension SHB schematic.



**Figure 3.7: Tension SHB (left) and dynamic tension specimen in adapter (right).**

The following set of equations can be used to calculate the engineering strain and stress in the specimen from measured experimental values, specimen dimensions, and values related to the SHB apparatus [35]. Assuming homogeneous deformation and force equilibrium, the strain rate is

$$\dot{\epsilon} = \frac{\dot{u}_1 - \dot{u}_2}{l} \quad (11)$$

where  $\dot{u}_1$  and  $\dot{u}_2$  are the linear velocities of the specimen at the incident and transmitter ends respectively. The length of the gage section is  $l$ . These velocities at a certain time,  $t$ , can be determined from 1-D elastic wave theory using

$$\dot{u}_1 = \frac{1}{\rho A c} \left[ F_A \left( t - \frac{L_A}{c} \right) + F_A \left( t - \frac{L_A}{c} + 2 \left( \frac{L_B}{c} \right) \right) - F_B \left( t + \frac{L_B}{c} \right) \right] \quad (12)$$

$$\dot{u}_2 = \frac{1}{\rho A c} \left[ F_C \left( t + \frac{L_C}{c} \right) \right] \quad (13)$$

where  $\rho$  is the density,  $A$  is the cross-sectional area, and  $c$  is the uniaxial wave speed of the incident and transmitter bars.  $c$  is defined as  $\sqrt{\frac{E}{\rho}}$ , the square root of the material modulus divided by the material density.  $L_A$ ,  $L_B$ , and  $L_C$  are distances from gages A, B, and C to the specimen.  $F_A$ ,  $F_B$ , and  $F_C$  are the force measured at gage A, B, and C, respectively. The strain rate can be integrated with respect to time to yield engineering strain:

$$\varepsilon_E(t) = \int_0^t \dot{\varepsilon}(t)dt \quad (14)$$

Finally, the engineering stress in the specimen at time  $t$  is:

$$\sigma_E(t) = \frac{F_c}{A_s} \left( t + \frac{L_c}{c} \right) \quad (15)$$

where  $A_s$  is the cross-sectional area of the tension specimen. These values can be converted to true stress and true strain using equations (9) and (10), respectively. Additional measurements are carried out using DIC techniques with 2 high speed Photron SA1.1 cameras positioned with a view of the surface of the specimen. These cameras record 64x208 pixel images of the experiments at a frame rate of 150000 frames per second.

Prior research by Gilat, et al., has shown that the wave equations are not valid in cases where significant strain occurs outside the gage section of the dynamic tension specimen [36]. This can be investigated by comparing the strains calculated from the wave data to those measured using DIC and by examining the surface strain across the specimen at several times throughout the test. Figure 3.8 shows that strains calculated using a 4.0 mm virtual extensometer from DIC data closely match those calculated from the SHB wave data for experiments at both  $500\text{s}^{-1}$  and  $2000\text{s}^{-1}$  up to the start of localization. Localization can be seen when the strain at the failure point diverges from that measured by the waves and virtual extensometer. Figure 3.9 and Figure 3.10 present waterfall plots of the axial strain versus location along the specimen for experiments at  $500\text{s}^{-1}$  and  $2000\text{s}^{-1}$ , respectively. It can be concluded from these figures that the strain outside the gage section is insignificant, so strain measurements from the SHB waves and DIC are valid.

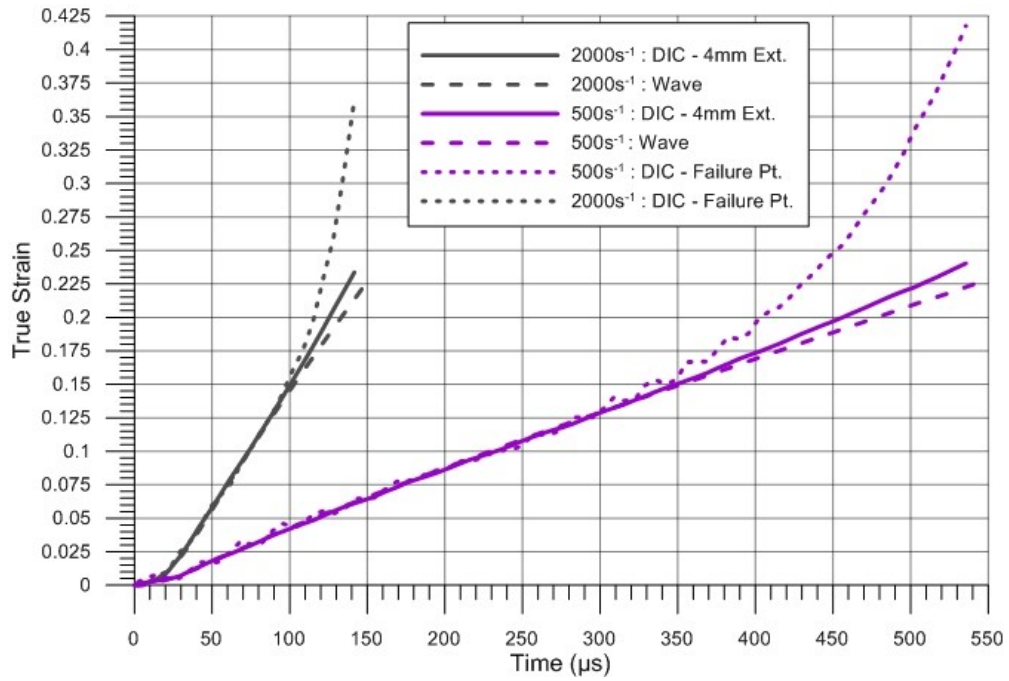


**Figure 3.8: Comparison of strain measurements versus time. Large dashed curves represent wave data and solid lines represent virtual extensometer data. The small dashes show strains measured using DIC at the specimen failure point.**

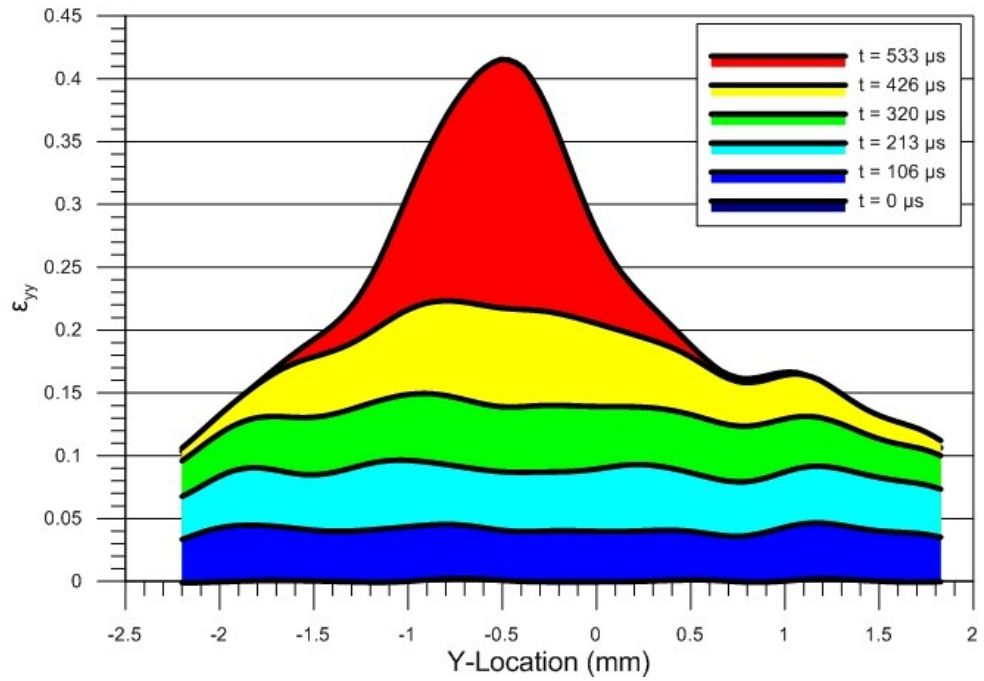


Figure 3.9: Axial strain across a specimen at different times in a dynamic tension experiment at  $500\text{s}^{-1}$ .

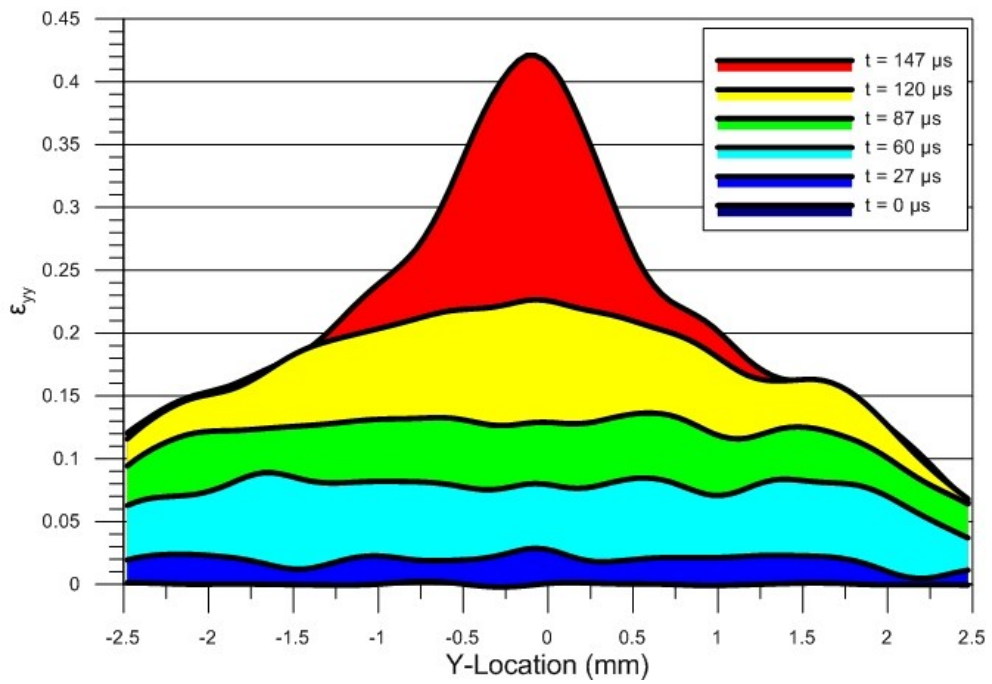
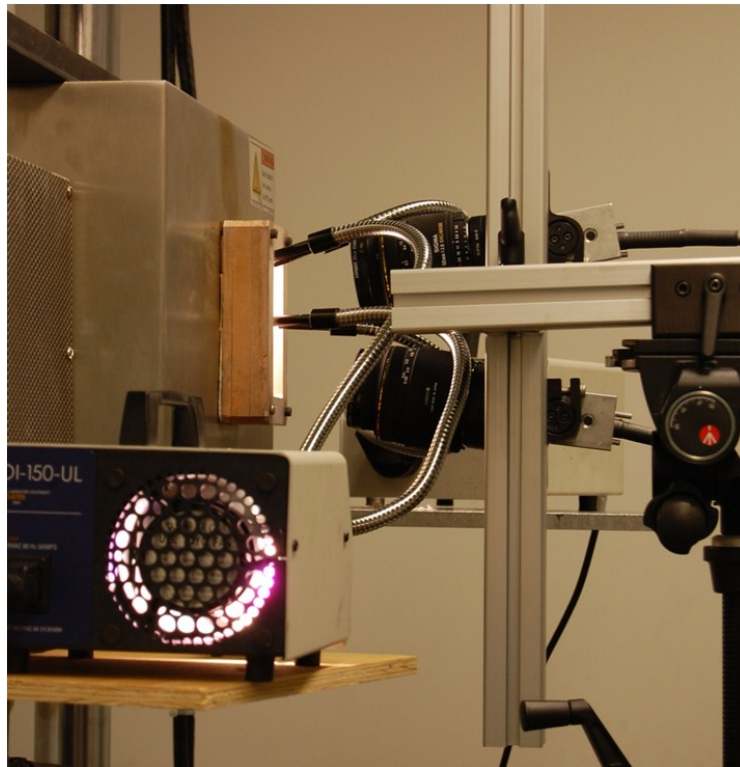


Figure 3.10: Axial strain across a specimen at different times in a dynamic tension experiment at  $2000\text{s}^{-1}$ .

#### ***3.3.1.4 Elevated Temperature Tension Experiments***

The elevated temperature test setup, which allows for experiments at temperatures up to 850°C, is described in this section. A specially designed furnace is mounted to the servo hydraulic load frame to achieve elevated specimen temperatures. There are cut-outs in the body and insulation of this furnace that allow custom tension fixtures to pass through the furnace and to be connected to the actuator and cross-head of the load frame. The front of the furnace has an optical quartz window, allowing two cameras to view the surface of the sample for taking DIC measurements. An Inconel 718 fan inside the furnace circulates the air to minimize temperature gradients and optical distortion. Two thermocouples are mounted to the walls of the furnace. These provide a feedback signal for a PID controller. A detailed image of the furnace is shown in Figure 3.11, and the overall setup can be seen in Figure 3.12.



**Figure 3.11: Close-up view of elevated temperature setup.**

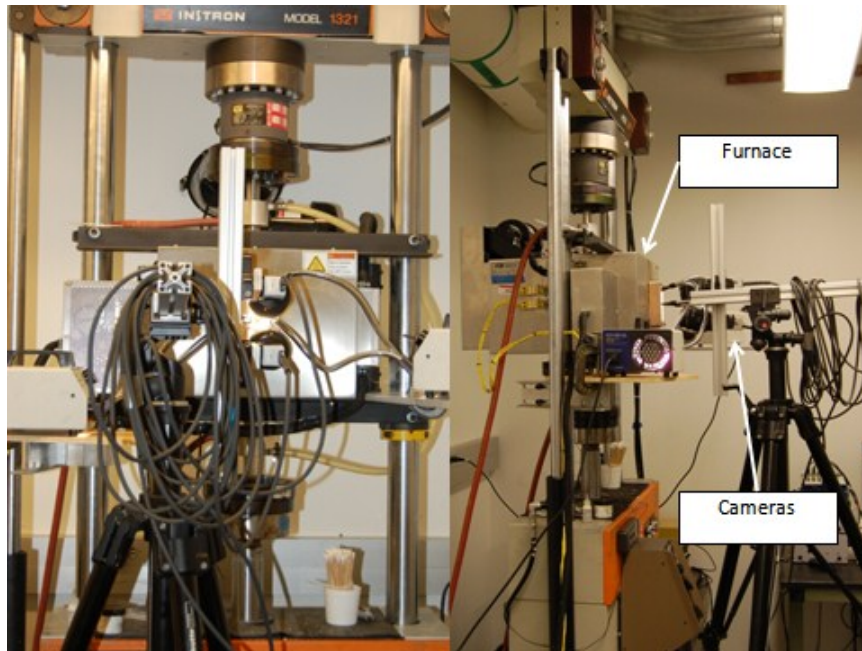


**Figure 3.12: Overall view of elevated temperature tension setup.**

A diagram of the tension fixture is shown in Figure 3.13. The fixture assembly is comprised of two slotted adapters, two #8 hex screws, two #8 hex nuts, and four 12.7mm cylindrical bushings. The slotted adapters, hex screws, and nuts are made from Inconel 718. The bushings are machined from Hastalloy-X. The tension specimen is placed in between the slotted adapters, and bushings are placed in the cylindrical holes on either side of both ends of the specimen. The #8 hex screws are then inserted through the bushings and the holes in the tension specimen, and the nuts are secured to the other side. Thus, the specimen is fixed on the inside of the through hole by the shoulder of the hex screw and on either surface by the pressure of the bushing. The bottoms of the slotted adapters are threaded such that they can be screwed into water cooled grips that mount upward to the crosshead and downward to the actuator head.

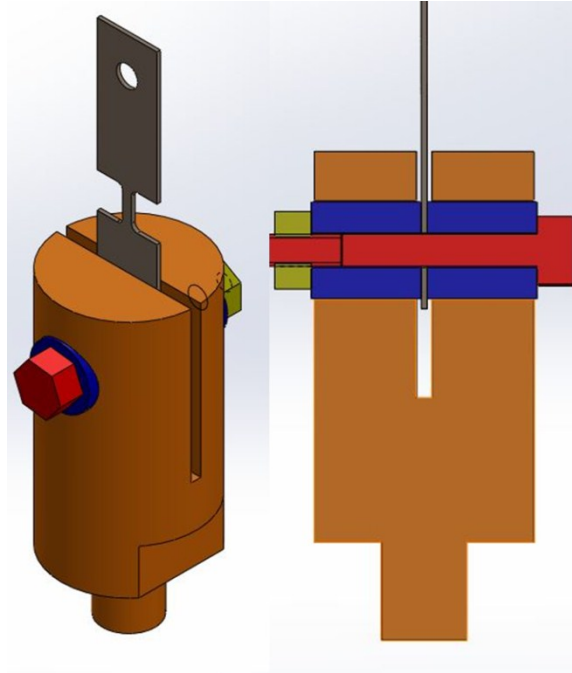


**Figure 3.13: Tension adapters for high temperature experiments. Components are: Inconel adapter (orange), #8 Screw (red), #8 Hex Nut (yellow), and Hastalloy-X Bushings (blue).**

The elevated temperature tension experiments are conducted in a similar way to the quasi-static tension experiments. The load frame is placed in load control with a 44.5 N tensile load on the specimen before the hex screw/nut assembly is tightened fully. This eliminates any slip in the fixture before the test is started and compensates for thermal expansion in the pull rods, ensuring the sample is not compressed and buckled. Two thermocouples are fixed to the back surface of the specimen: one near the upper fixture and one near the lower fixture. The temperature history of the specimen is recorded during the heating phase. Once the average of the two thermocouple readings reaches the desired temperature the load frame is switched back into displacement control, and the actuator head is displaced at a constant velocity.

### 3.3.2 Compression Experiments

Compression experiments are conducted to investigate the plastic deformation behavior of Inconel 718 in uniaxial compression. The experimental outline for compression tests is presented in Table 3.4. Strain rate sensitivity is studied with experiments at strain rates of  $1 \times 10^{-4}$ ,  $1 \times 10^{-2}$ , 1.00, 1000, and  $2000 \text{ s}^{-1}$  on specimens fabricated in the rolled direction. Experiments are conducted at  $1.00 \text{ s}^{-1}$  on specimens in an additional four directions;  $45^\circ$  from rolled, transverse,  $-45^\circ$  from rolled, and through the thickness of the plate; to study anisotropy.

Test No.	Testing Apparatus	Strain Rate (1/s)	Specimen Orientation	Temperature
1	Hydraulic Load Frame	1.00E-04	Rolled	Room Temp
2		1.00E-02		
3		1.00E+00		
4	Compression SHB	1.00E+03		
5		2.00E+03		
6	Hydraulic Load Frame	1.00E+00	45 from Rolled	
7			Transverse	
8			- 45 from Rolled	
9			Through Thickness	

Table 3.4: Experimental outline for precipitate hardened Inconel 718 plastic deformation tests in compression.

#### 3.3.2.1 Compression Specimen Design and Fabrication

Compression samples were fabricated from the same 12.7mm plate as the tension specimens. The compression specimen geometry is shown in Figure 3.14. It is a cylinder with both a height and a diameter of 3.81mm. This geometry is small because strain rate is inversely proportional to gage length in dynamic compression tests on the compression SHB apparatus, small samples ensure force equilibrium and uniform deformation, and small geometry ensures a large difference between the incident and transmitted forces that results in plastic deformation. The same specimen geometry is used in all compression test series to ensure that specimen geometry does not influence the results.



**Figure 3.14: Compression specimen geometry.**

Compression specimens are fabricated in a total of five separate orientations to investigate anisotropic behavior. These orientations – the rolled direction,  $+45^\circ$  to rolled, transverse,  $-45^\circ$  to rolled, and through thickness – are diagrammed in Figure 3.2. A representative drawing of the Inconel plate stock is shown, with the rolled direction and transverse direction axes labeled.

### ***3.3.2.2 Quasi-static Compression Experiments***

Quasi-static compression experiments are conducted on the 89kN servo hydraulic load frame. The experimental set up, shown in Figure 3.15, is similar to that used in quasi-static tension experiments. The specimen is placed between two 12.7mm diameter tungsten carbide platens. The contact surfaces between platen and specimen are lubricated with  $\text{MoS}_2$  grease. These platens are fit into cylindrical slots cut in the top and bottom fixtures. The top fixture is mounted to the 89kN load cell, and the load cell is fixed to the crosshead of the load frame. The bottom fixture is mounted to the actuator head of the load frame. Two cameras are positioned between 0.25m and 0.50m from the specimen such that their focal points are trained on the same location on the specimen surface and the angle between them is between  $10^\circ$  and  $15^\circ$ .

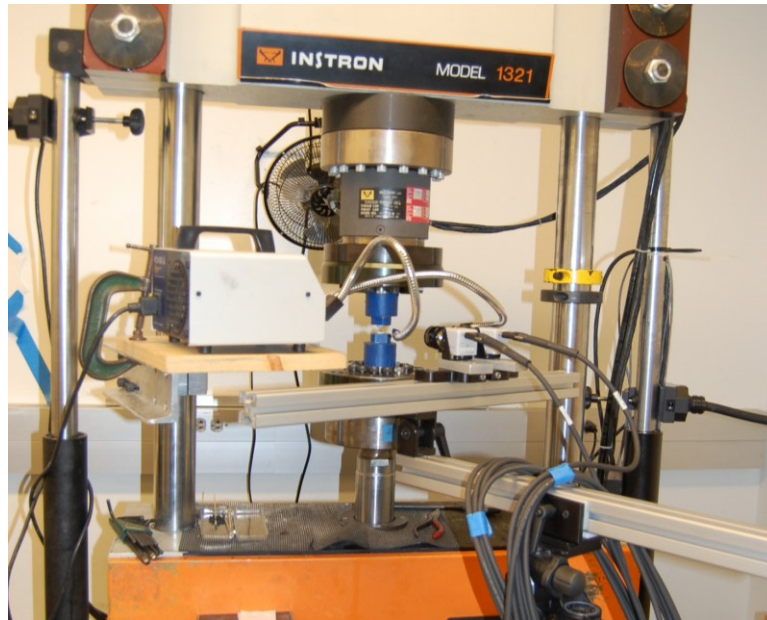


**Figure 3.15: Quasi-static compression setup**

The actuator motion control is the same as in quasi-static tension experiments. The specimen is first placed between the platens and given a pre-load between 222N and 445N. The actuator is moved upward in displacement control a total distance of 1.9mm; one half the specimen height; at a constant velocity such that the nominal strain rate matches that desired for the experiment.

The actuator displacement is recorded from the LVDT. The applied compressive load is recorded from the load cell. Additional measurement data is generated using DIC techniques and images taken by the cameras throughout the duration of the test. The number of images taken is dependent on the camera framerate and test duration; however it is typically around 500 images in the quasi-static tests. Tests at the nominal strain rate of  $1.0 \times 10^{-4} \text{s}^{-1}$  and  $1.0 \times 10^{-2} \text{s}^{-1}$  use Point Gray Research GRAS-20S4M-C cameras, and tests at  $1.0 \text{s}^{-1}$  use Photron MC2 cameras. The Point Gray cameras take  $1624 \times 1224$  pixel images at a rate of one image every 10 seconds. The Photron

cameras take 512x512pixel images at a rate of 10 frames per second. These data are used with measurements of the specimen geometry to calculate engineering strain, engineering stress, true strain, and true stress using equations (16),(17),(9), and (10).

$$\varepsilon_E = \frac{\Delta l}{h} \quad (16)$$

$$\sigma_E = \frac{F}{\frac{\pi d^2}{4}} \quad (17)$$

Where  $\Delta l$  is the vertical displacement measured using a 4mm virtual extensometer from DIC measurements,  $h$  is the specimen height,  $F$  is the applied compressive load, and  $d$  is the measured specimen diameter.

### ***3.3.2.3 Dynamic Compression Experiments***

Dynamic compression experiments at nominal strain rates of  $1000\text{s}^{-1}$  and  $2000\text{s}^{-1}$  are completed using a split-Hopkinson pressure bar apparatus. A schematic diagram of the SHB setup is shown in Figure 3.16, and a photograph of the setup is shown in Figure 3.17. This apparatus consists of three main components: the striker bar, incident bar, and transmitter bar. The bars are made of 12.7mm diameter Ti-6Al-4V rods. The striker bar is 0.61m long. The incident and transmitter bars are 1.22m long. The specimen is located between the incident and transmitter bars, which are instrumented at the center of their lengths with strain gages to measure the incident and transmitted compression waves, respectively. These strain gages are excited by a 15V DC signal from a HP E3611A DC power supply. Each gage's signal is sent through a SRS SR560 low noise preamplifier and is then recorded on a Tektronix oscilloscope. Two high-speed Photron SA 1.1 cameras are positioned next to the compression SHB such that they can record the deformation of the specimen throughout the duration of the experiment. These cameras record 128x112 pixel images at a frame rate of 200000 frames per second.

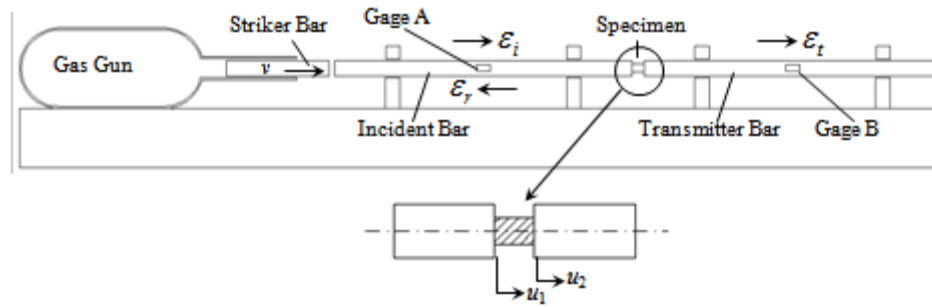


Figure 3.16: Compression SHB schematic diagram.

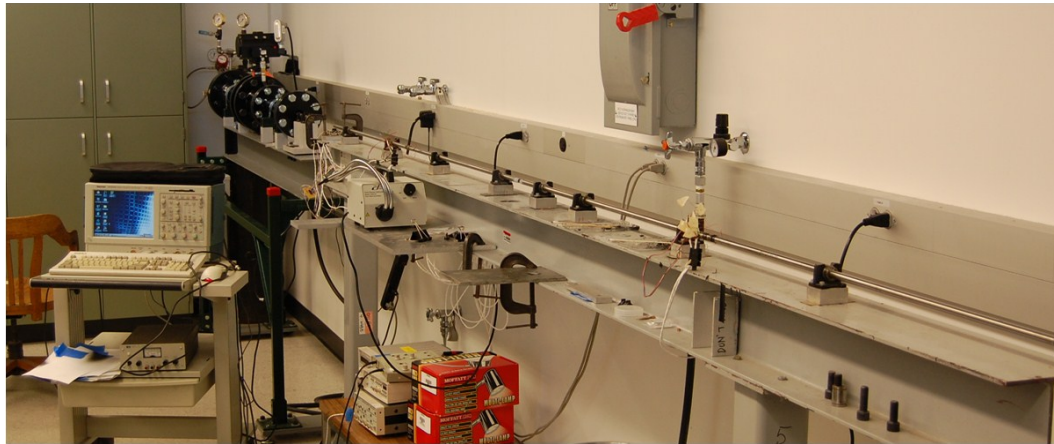


Figure 3.17: Photograph of compression SHB.

An input wave is generated by using a gas gun to fire the striker bar into the incident bar. As the wave ( $\epsilon_i$ ) passes through the incident bar, it is measured by gage A. The portion of the wave that acts on the specimen ( $\epsilon_t$ ) is transferred into the transmitter bar and measured at gage B, while the rest of the wave reflects back ( $\epsilon_r$ ) and is measured by gage A.

The following calculations are used to find displacements, load, stress, and strain in the dynamic compression test using data recorded at the strain gages. These simple equations assume 1-D wave propagation, that the incident and transmitter bars remain elastic during the test, and that the specimen is in force equilibrium. This assumption is generally true except for a “ringing-up” period during the start of specimen loading. Those looking for more information should

consult the ASTM handbook section on Classic Split-Hopkinson Pressure Bar Testing [37].

From the 1-D split-Hopkinson bar wave theory, the strain rate can be expressed as

$$\dot{\varepsilon} = \frac{2c_b \varepsilon_r}{l_s} \quad (18)$$

where  $c_b$  is the longitudinal wave speed in the bars,  $\varepsilon_r$  is the reflected wave, and  $l_s$  is the length of the compression specimen. This can be integrated with respect to time to find the strain in the specimen.

$$\varepsilon_E = \int_0^t \dot{\varepsilon}(t) dt \quad (19)$$

The relative displacement can be calculated using the engineering strain and the specimen length.

$$u = \varepsilon_E l_s \quad (20)$$

The force in the specimen is simply equal to the transmitted force  $F_t$  and thus the normal engineering stress can be calculated by

$$\sigma_E = \frac{F_t}{A_s} \quad (21)$$

where  $A_s$  is the cross-sectional area of the specimen, and  $F_t$  is

$$F_t = EA\varepsilon_t \quad (22)$$

where  $E$  is the elastic modulus of the transmitter bar,  $A$  is the cross-sectional area of the transmitter bar, and  $\varepsilon_t$  is the transmitted strain wave.

### 3.3.3 Three Dimensional Digital Image Correlation (DIC)

Digital Image Correlation (DIC) is an optical measurement technique that allows researchers to examine full field displacements and strains on the surface of a specimen. A detailed analysis of this technique is conducted by Sutton, Orteu, and Schreier [38]. Several DIC systems are available commercially. The work shown herein is completed using Correlated Solutions VIC-3D 2009 [39].

The 3D – DIC system consists of two cameras that provide a stereographic view of the specimen, data acquisition software that provides time synchronized images, and 3D DIC software that processes the acquired images. 3D-DIC measurements are completed by first calibrating the system, recording and processing an experiment, and then using post-processing techniques to extract the desired data.

In order to ensure accurate measurements, the 3D-DIC system is calibrated by taking multiple photographs of a panel with known grid spacing in various orientations. These images are taken using both cameras and are then analyzed using the VIC-3D software. The software uses the known grid measurements to calculate the location of each camera, which is then used to create a series of transformations between coordinates in the 2-D pixel space and a three dimensional world coordinate system.

Once the system is calibrated, the system records raw images of the deformation during the test. The specimen is given a speckle pattern with white and black spray paint. The DIC software analyzes each pair of images by first discretizing the image into  $n \times n$  pixel subsets. The first image becomes a reference image for all images after it. The software tracks the displacement of each subset using the gray scale values of the speckle pattern on the specimen by referencing the location of the subsets relative to their locations in the reference image. Strains are calculated from these displacements using one of several available definitions of the strain tensor.

The 3D-DIC software gives the user a variety of post-processing inspection options, such as data from a single point, a virtual extensometer, or data averaged within a box. Data extracted at a single point is useful for understanding the evolution of the strain state at a point of interest, like the location of specimen fracture. Virtual extensometers of arbitrary length can be used to determine engineering strain. These data can be compared to data generated using traditional

measurement techniques like mechanical extensometers and strain gages. Averaged data in a given area can be extracted as well. Furthermore, multiple methods may be used in conjunction. Data from points and averaged areas include five strain components -  $\epsilon_{xx}$ ,  $\epsilon_{yy}$ ,  $\epsilon_{xy}$ ,  $\epsilon_1$ ,  $\epsilon_2$  – and three displacement measurements – x-displacement ( $u$ ), y-displacement ( $v$ ), and z-displacement ( $w$ ).

### 3.3.3.1 DIC Measurements – Tension Experiments

Strain data from all tension tests are presented with DIC measurements. These data are collected using a 4mm virtual extensometer over the gage section of the tension specimen. An example of this measurement is shown in Figure 3.18a and b. Figure 3.18a shows the initial extensometer length before deformation has taken place, and Figure 3.18b shows the extensometer length at the moment before specimen failure.

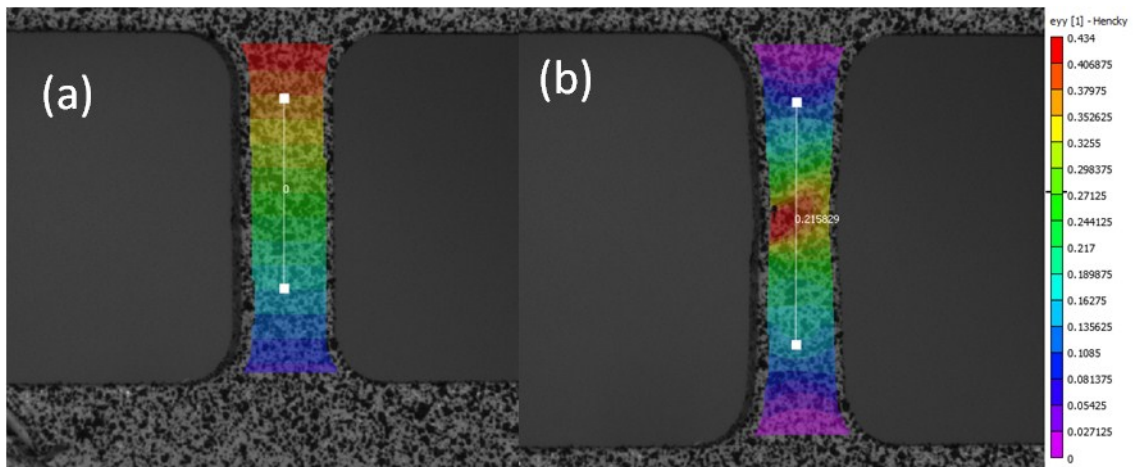


Figure 3.18: 4mm extensometer used in tension data processing. (a) initial length (b) length prior to failure.

### 3.3.3.2 DIC Measurements – Compression Experiments

Strain data from all compression tests, except those completed at nominal strain rates of  $1000s^{-1}$  and  $2000s^{-1}$  on the compression SHB apparatus, are presented with DIC strain measurements. These data are collected using a combination of data collected from a 2mm virtual extensometer

over the specimen surface and the relative displacements of the platens. The elastic deformation is collected from the extensometer, and deformation after yield is from the relative platen motion. Strain calculated from platen motion is:

$$\varepsilon = \frac{u_1 - u_2}{l_o} \quad (20)$$

where  $u_1$  is the lower platen,  $u_2$  is the upper platen, and  $l_o$  is the initial gage length of the specimen. This technique is used because the barreling phenomenon, which arises due to friction at the sample/platen interface, results in surface strains that are not representative of the strain in the center of the specimen. The 2mm extensometer is shown in Figure 3.19a, and the selected platen areas are shown in Figure 3.19b.

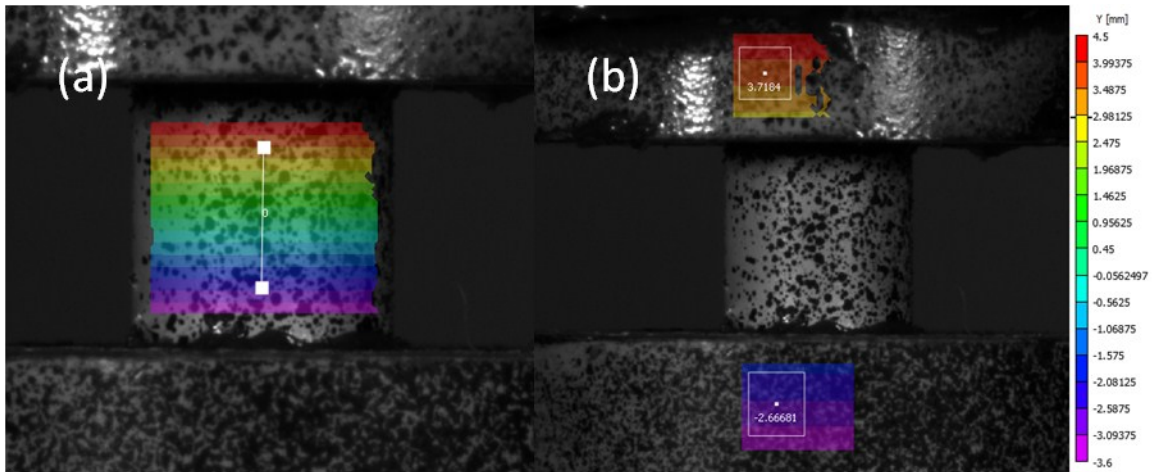


Figure 3.19: (a) 2mm extensometer and (b) platen area data used in compression DIC measurements.

### 3.4 Plastic Deformation of Precipitate Hardened Inconel 718 Experimental Results & Discussion

Results and discussion are presented for experimental tests conducted in tension and compression at various strain rates, orientations, and temperatures. Data from each series is presented independently followed by a discussion of its characteristics, specifically those of yield, plastic

flow, ultimate stress, and failure behavior. Parameters – determined by fitting the experimental data sets - are presented that model the material behavior in both tension and compression using the Johnson-Cook plasticity model.

### 3.4.1 Strain Rate Sensitivity Test Series

Representative experimental data from tension experiments at various strain rates on specimens fabricated in the rolled direction are shown in Figure 3.20. The material yields around 1100 MPa in the low strain rate conditions. It exhibits significant strain hardening – approximately 500 MPa - between yield and ultimate stress. The ultimate stresses occur around 22.5% strain in the lowest two strain rates, and around 18.5% strain at  $1.00s^{-1}$ ,  $500s^{-1}$  and  $2000s^{-1}$ .

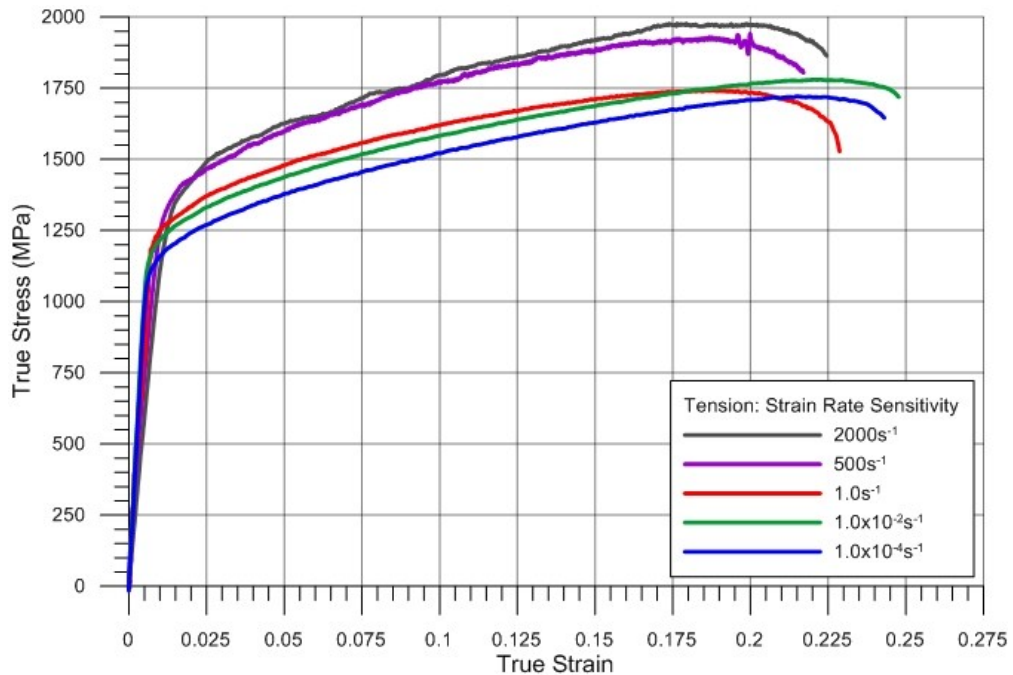
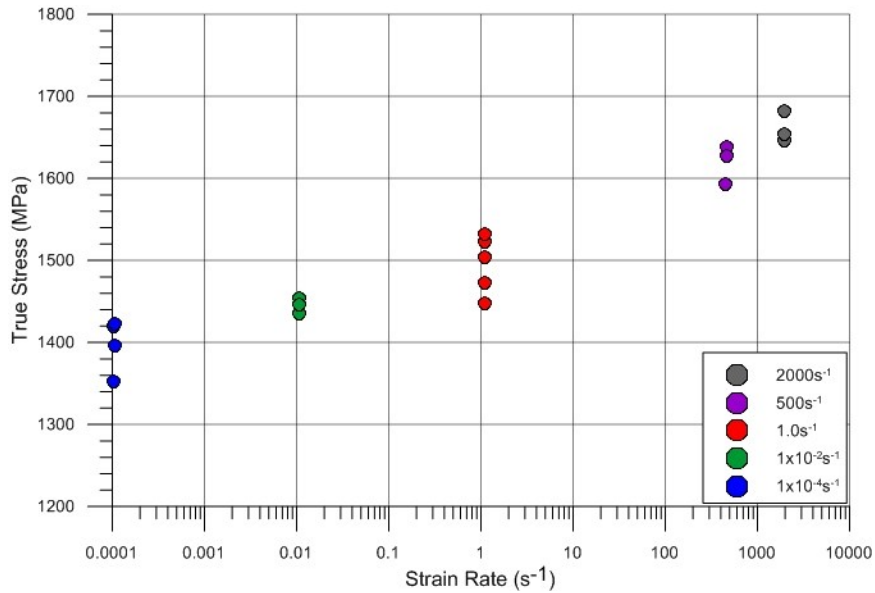


Figure 3.20: True stress versus true strain data for tension experiments at different strain rates.

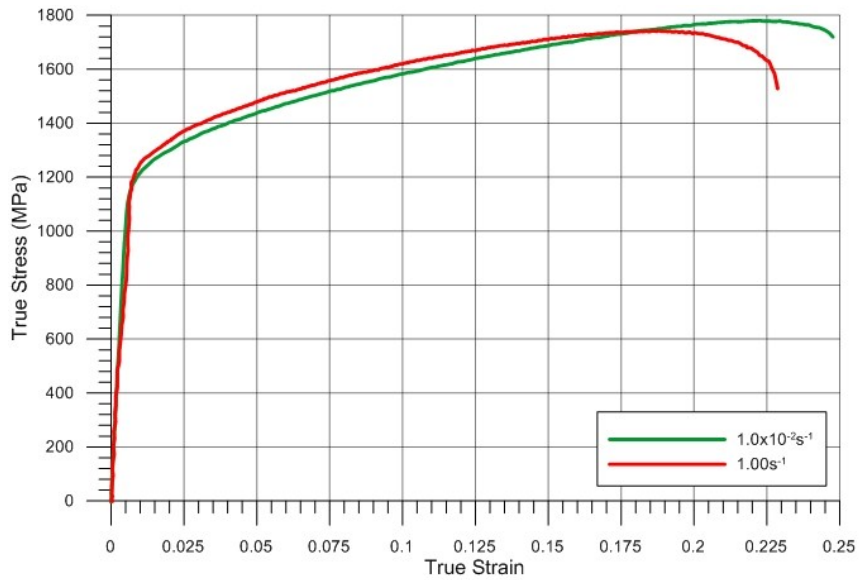
To further examine strain rate sensitivity the true stress at 5% true strain for each test at each nominal strain rate is identified and plotted against the average strain in Figure 3.21. True stress

increases with increasing strain rate, rising from roughly 1400MPa at  $1 \times 10^{-4} \text{ s}^{-1}$  to around 1650MPa at  $2000 \text{ s}^{-1}$ .



**Figure 3.21 - True stress (MPa) at 5% strain versus strain rate ( $\text{s}^{-1}$ ) data in tension for precipitate hardened Inconel 718**

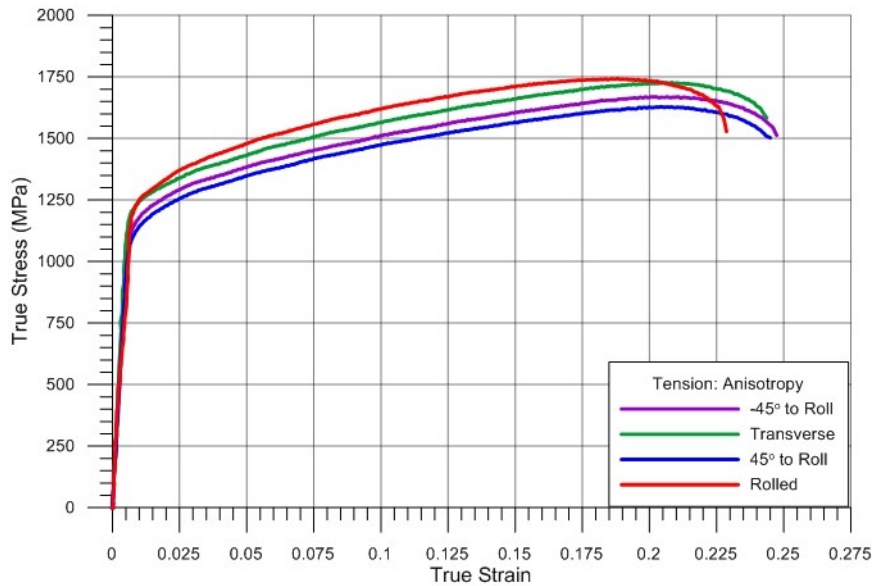
In addition to a degree of rate dependence, the data from this test series presents another interesting trend with regard to plastic flow behavior. Data from one test at  $1.0 \text{ s}^{-1}$  and one test at  $1.0 \times 10^{-2} \text{ s}^{-1}$  are presented in Figure 3.22. Starting around 11% strain, the rate of strain hardening – i.e. the slope of the true stress/true strain curve – is lower in the  $1.0 \text{ s}^{-1}$  test than in the  $1.0 \times 10^{-2} \text{ s}^{-1}$  case. Despite a lower yield stress, the slower test results in a higher ultimate stress. This result suggests that the strain hardening behavior varies slightly with strain rate, in addition to the typical increase in stress with increasing strain rate.



**Figure 3.22 - True stress (MPa) versus true strain data from two tests: one at  $1.0 \times 10^{-2} \text{ s}^{-1}$ , one at  $1.0 \text{ s}^{-1}$ . Notice the change in the rate of strain hardening beginning around  $\epsilon_T = 0.011$ .**

### 3.4.2 Tension Anisotropy Test Series

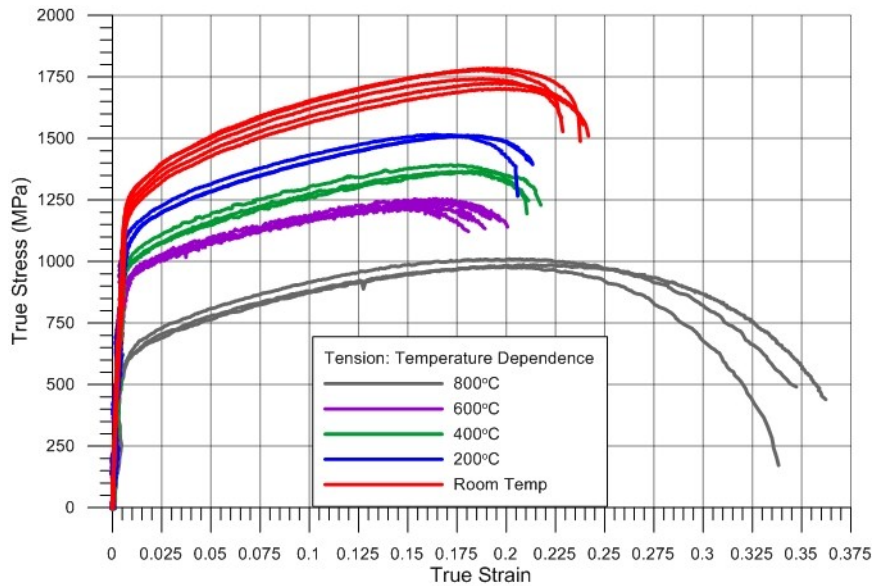
Representative experimental results for the anisotropy series are presented in Figure 3.23. These data show moderately different behavior in between the  $\pm 45^\circ$  directions and the rolled/transverse directions. The yield stress is approximately 1075MPa for the former and 1175MPa for the latter. This trend holds for the ultimate stress where the  $\pm 45^\circ$  directions average roughly 1600MPa and rolled/transverse directions about 1725MPa. One interesting difference is in the strain at onset of localization and failure. The rolled direction sample localizes around 18.5% strain and fails just past 22.5% strain. The other directions all localize around 21% strain and fail at approximately 24.5% strain.



**Figure 3.23 - True stress (MPa) versus true strain data for tension anisotropy experiments. Note that representative curves from the test series are shown for clarity.**

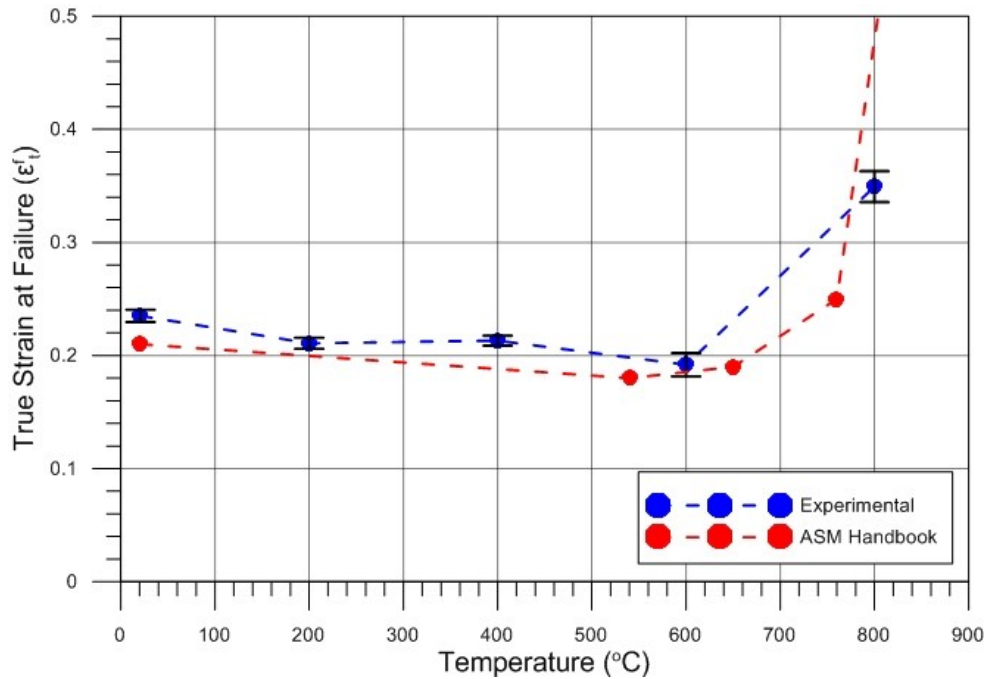
### 3.4.3 Tension Temperature Dependence Test Series

Experimental data from the tension temperature dependence test series are presented in Figure 3.24. Room temperature data (red) has an average yield stress of 1139MPa, average ultimate stress of 1747MPa, and fail at roughly 23% strain. The data at 200°C (blue) average a yield stress of 1019MPa, an ultimate stress of 1514MPa, and fail at roughly 21% strain. Test data generated at 400°C (green) average yield stress at 921MPa, ultimate stress at 1376MPa, and fail at approximately 21% strain. Three experiments conducted at 600°C (purple) average yield stress around 852MPa, ultimate stress of 1239MPa, and fail between 18% and 20% strain. Finally, three experiments conducted at 800°C (grey) report average yield stress of 525MPa and average ultimate stress of 992MPa. The 800°C specimens showed greater ductility, failing between 34% and 36% strain.



**Figure 3.24 - True stress (MPa) versus true strain data from tension experiments carried out at room temperature (red curves), 200°C (blue), 400°C (green), 600°C (purple), and 800°C (grey)**

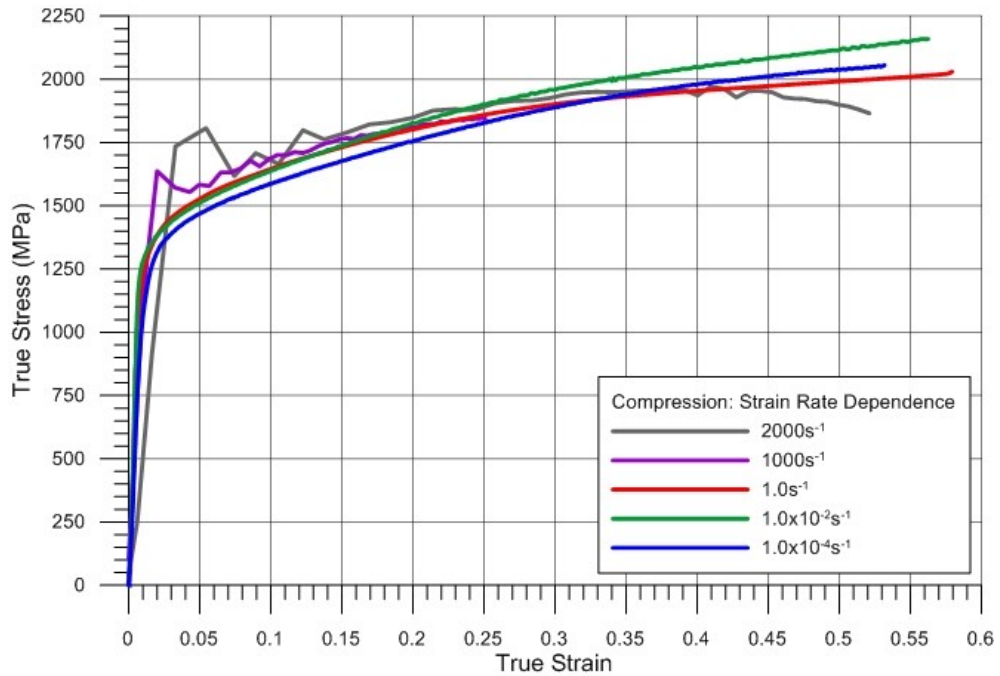
Two phenomena may be observed from the data in Figure 3.24. First, the strength decreases with increasing temperature. This strength decrease, however, is not proportional to the change in temperature. This is shown by the relative strength differences between the curves. The room temperature and 200°C curves differ by roughly 150MPa, while the difference between 400°C and 600°C is as small as 75MPa at yield. Furthermore the gap between the 600°C and 800°C curves is roughly 300MPa at yield. The second phenomenon is the unusual change in ductility as temperature increases. Typically, ductile metals tend show increased ductility with increased temperature. For precipitate hardened Inconel 718, however, decreases slightly up to 600°C. This is followed by a roughly 80% increase in ductility between 600°C and 800°C. This behavior is corroborated by tensile elongation values from the ASM Handbook [40] as well as testing completed by Brinkman and Korth [41] in their study focusing on fatigue behavior of the material. The average experimental data, with 95% confidence intervals, and ASM values are plotted in Figure 3.25.



**Figure 3.25: True strain at failure versus temperature data. Experimental data (blue) is compared to ASM handbook data (red).**

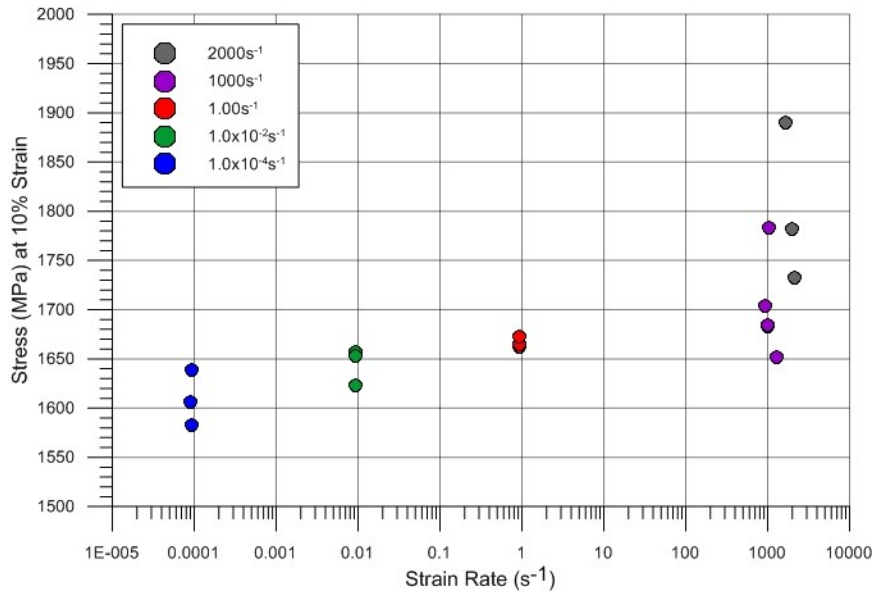
### 3.4.4 Compression Strain Rate Sensitivity Test Series

Representative data from compression experiments at various strain rates on specimens fabricated in the rolled direction are shown in Figure 3.26. Yield occurs around 1200 – 1250MPa in the quasi-static experiments (strain rates  $1.0 \times 10^{-4}$ ,  $1.0 \times 10^{-2}$ , and  $1.00 \text{s}^{-1}$ ). The plastic flow behavior is similar to that seen in tension. The material exhibits significant strain hardening, with stress rising roughly 700MPa by 30% strain. As the strain rate increases the strain hardening rate decreases at 20% strain.



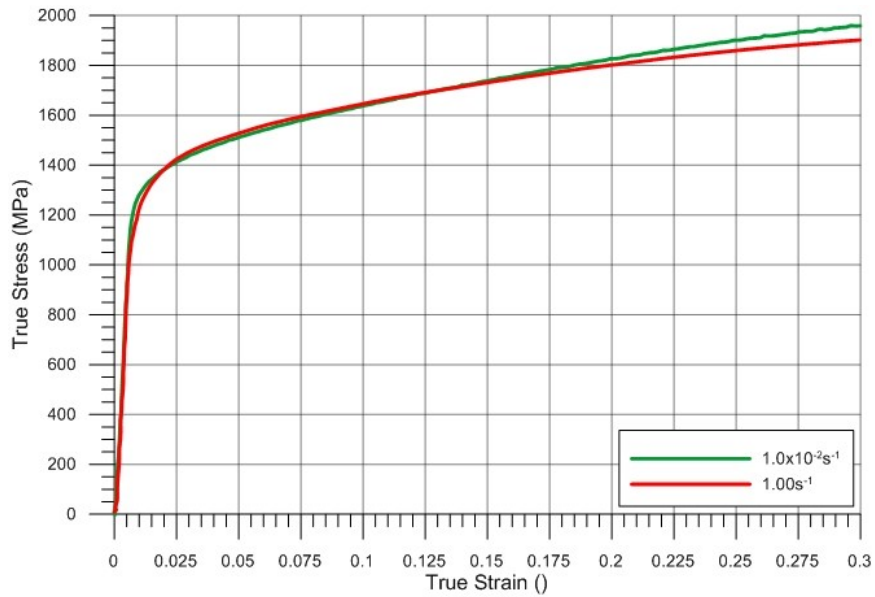
**Figure 3.26: True stress (MPa) versus true strain data for compression experiments at various strain rates.**

True stress at a true strain of 10% is plotted versus the log of strain rate,  $\dot{\epsilon}$ , in Figure 3.27. The data shows that the material exhibits sensitivity to strain rate when loaded in compression. The data around  $\dot{\epsilon} = 1000\text{s}^{-1}$  and  $\dot{\epsilon} = 2000\text{s}^{-1}$ , which correspond to dynamic tests completed on the split Hopkinson pressure bar apparatus, is more widely spread than the data from quasi-static tests completed on the servo hydraulic load frame.



**Figure 3.27: True stress (MPa) at  $\epsilon = 0.10$  versus strain rate for the compression test series**

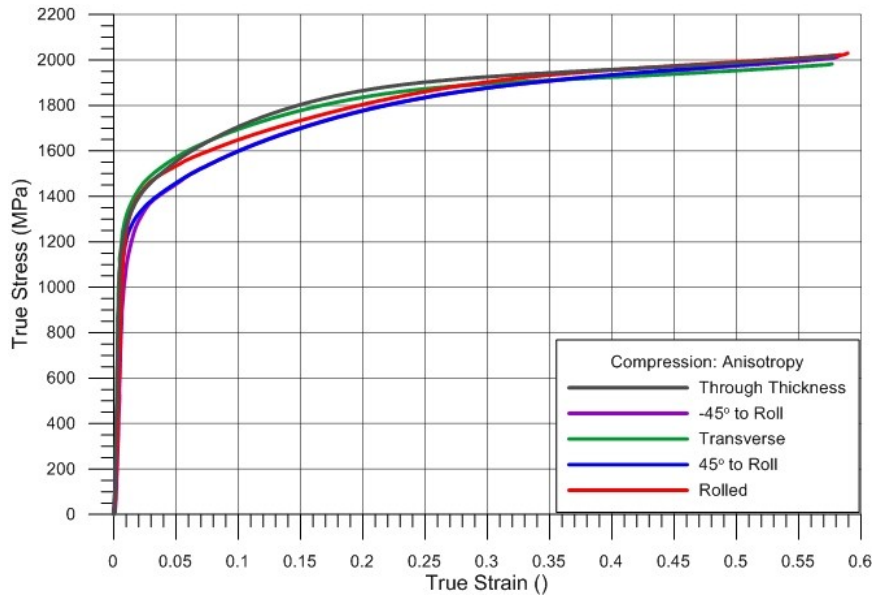
These data exhibit a similar strain hardening rate to that observed in tension between  $1.0 \times 10^{-2} \text{ s}^{-1}$  and  $1.0 \text{ s}^{-1}$ . True stress versus true strain records for two compression tests are shown in Figure 3.28. The experiment conducted at a nominal strain rate of  $1.0 \times 10^{-2} \text{ s}^{-1}$  is shown in green, and the experiment conducted at a nominal strain rate of  $1.0 \text{ s}^{-1}$  is shown in red. These two samples yield at approximately the same stress level, and their strain hardening rates are nearly identical between yield and a true strain of 7.5%. The strain hardening rate decreases at true strains greater than 7.5%, resulting in a lower true stress level around 13.5% true strain. The plastic flow behavior is sensitive to changes in strain rate, particularly, strain rates greater than  $1.0 \text{ s}^{-1}$ . The strain hardening rate decreases as strain increases when compared to that at  $1 \times 10^{-4} \text{ s}^{-1}$  and  $1 \times 10^{-2} \text{ s}^{-1}$ .



**Figure 3.28: True stress (MPa) versus true strain data for two compression tests.**

### 3.4.5 Compression Anisotropy Test Series

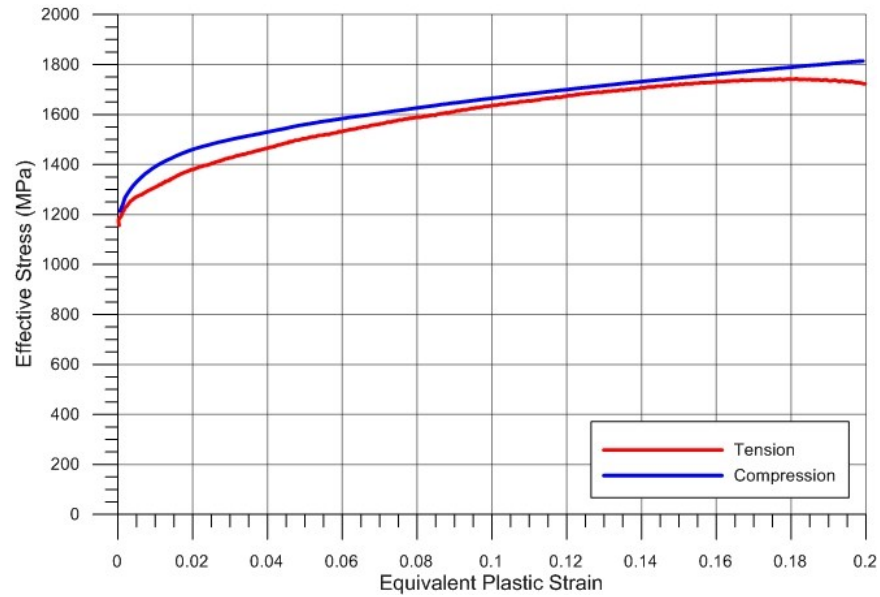
Representative data from experiments on specimens fabricated in each direction is presented in Figure 3.29. In this plot the  $\pm 45^\circ$  directions show similar behavior, as do the through thickness and transverse direction. The rolled direction data is interesting because it yields at roughly the same stress as the transverse and through directions, but exhibits less strain hardening. In fact, the strain hardening rates between yield and 15% true strain are roughly equal for all directions except the rolled. At true strain larger than 15%, the transverse and through direction strain hardening rate is less than that of the  $\pm 45^\circ$  directions. The stress at high strains (true strain  $\geq 45\%$ ) is nearly the same for all orientations.



**Figure 3.29: Representative true stress (MPa) versus true strain data from compression experiments conducted at a nominal strain rate of  $1.0s^{-1}$  on specimens machined in various orientations.**

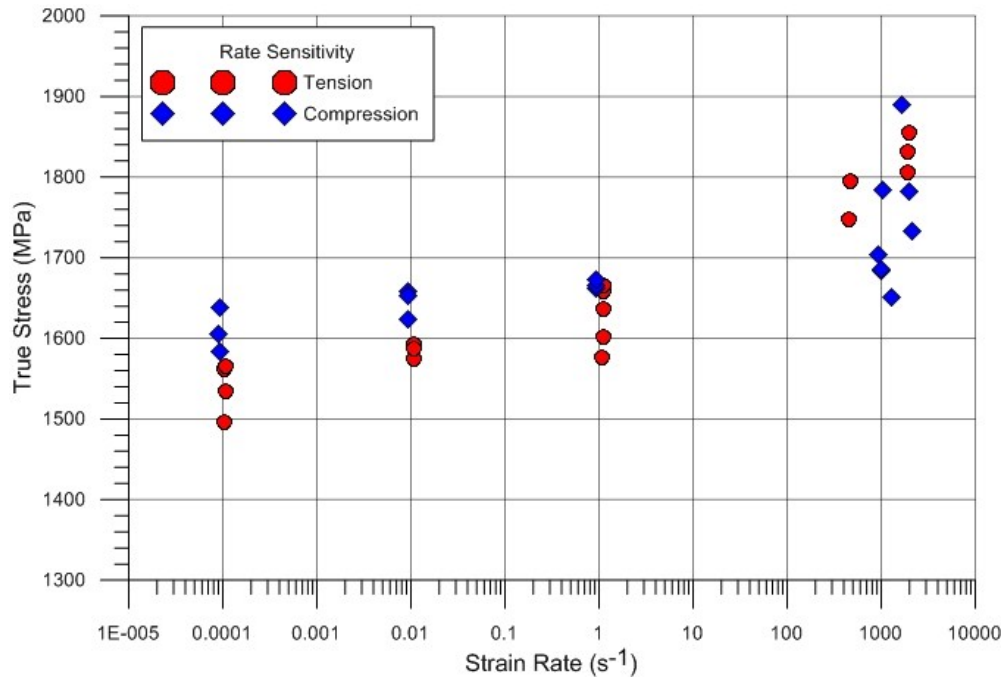
### 3.4.6 Comparison of Tension and Compression Data

Figure 3.30 presents effective stress versus equivalent plastic strain for representative experimental data from tension and compression experiments at a nominal strain rate of  $1.0s^{-1}$ . These data suggest that the material response is the same in both tension and compression.



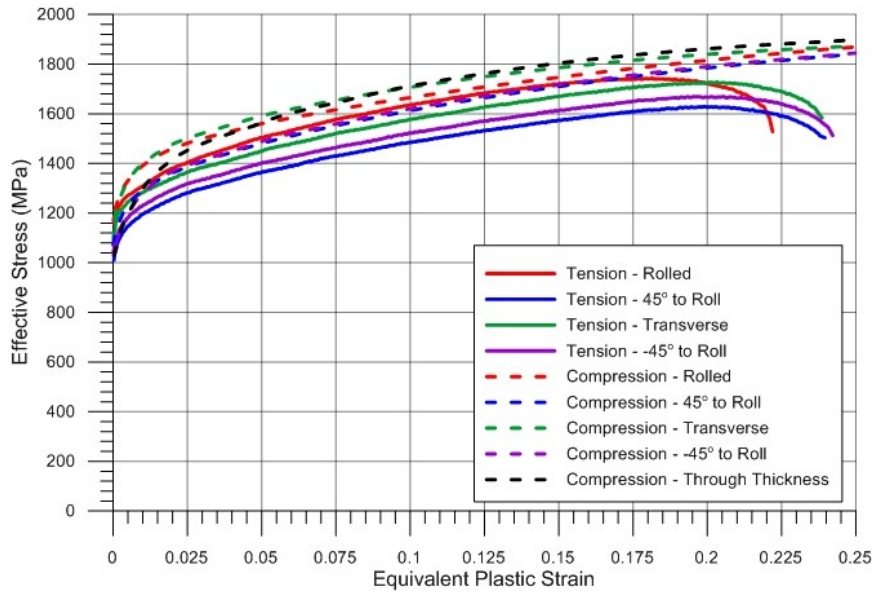
**Figure 3.30: Effective stress versus equivalent plastic strain data for the tension and compression loading conditions at the  $1.0s^{-1}$  strain rate.**

Figure 3.31 compares true stress at 10% true strain versus strain rate data for experiments in tension and compression. The material shows greater rate sensitivity in tension than compression. At low strain rates the stress in compression is greater than that in tension, and at high rates the tension and compression data fall in the same stress range.



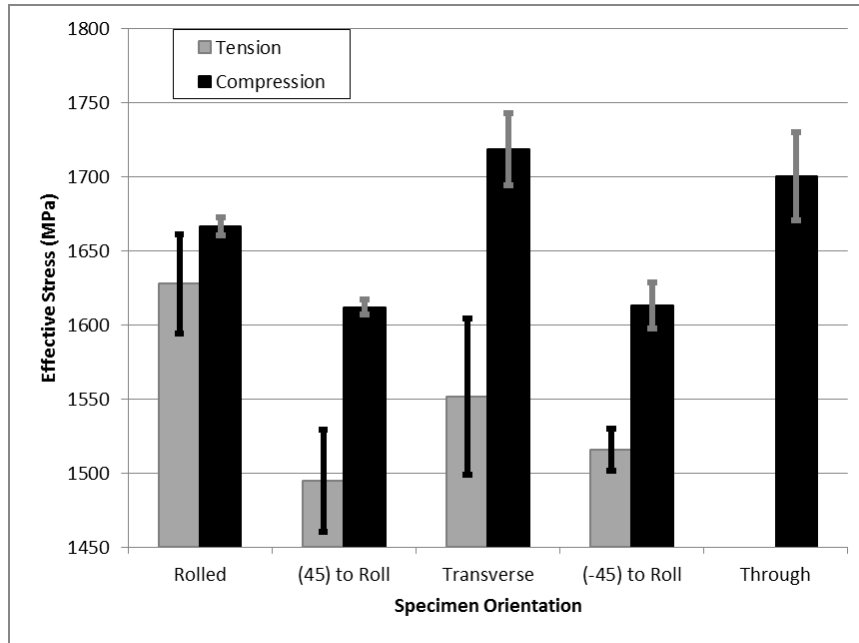
**Figure 3.31: Comparison of rate sensitivity data for tension and compression. True stress at 10% true strain versus strain rate.**

Figure 3.32 presents representative effective stress versus equivalent plastic strain data for tension and compression experiments conducted on specimens fabricated from different directions through the 12.7mm plate stock. This data suggests subtle anisotropy and potentially differences in flow behavior between the loading configurations.



**Figure 3.32: Effective stress versus equivalent plastic strain data for specimens with various plate orientations**

Figure 3.33 plots the average effective stress at 10% equivalent plastic strain for each specimen orientation. The error bars reflect the 95% confidence intervals. The chart suggests that the anisotropy present in both tension and compression is statistically significant. Specifically, the stresses in the  $\pm 45^\circ$  direction are less than those in the rolling direction. Average transverse stress is less than the rolling direction stress in tension; however, the opposite is true in compression. This trend suggests an asymmetry between tension and compression.



**Figure 3.33: Effective Stress at 10% equivalent plastic strain and specimen orientation with 95% confidence intervals.**

### 3.4.7 Constitutive Modeling of Precipitate Hardened Inconel 718

The Johnson-Cook model is shown in equation (1). The Johnson-Cook parameters can be determined from experimental data that covers a wide range of strain rates and temperatures. The process established by Johnson and Cook [1] is used to determine parameters for precipitate hardened Inconel 718.

Parameters  $A$ ,  $B$ ,  $n$ ,  $C$ , and  $m$  are determined in three steps. First, effective stress is plotted versus equivalent plastic strain for each test at the reference strain rate ( $1.0s^{-1}$ ). Since these experiments are conducted at the reference strain rate and the reference temperature, the second and third terms in the Johnson-Cook equation are equal to 1. Constants  $A$ ,  $B$ , and  $n$  are determined for each curve using the MATLAB curve fitting toolbox. Parameters for each test are recorded, then averaged. With  $A$ ,  $B$ , and  $n$  known, the strain rate constant,  $C$ , is determined by setting  $A$ ,  $B$ , and  $n$  equal to those values found in step one and fitting the resultant equation to data from experiments

conducted at various strain rates at room temperature.. The final term,  $m$ , is determined by fitting the equation to experiments conducted at various temperatures. The reference temperature is 21°C. The melting temperature for Inconel 718, 1298°C, is determined by finding the average of the melt temperature range presented in literature from Special Metals Co [42].

The Johnson – Cook parameters from experiments conducted on 12.7mm thick precipitate hardened Inconel 718 plate specimens in tension and compression are presented alongside existing parameters from Kobayashi, et al.[29], and Pereira, et al.[28] in Table 3.5.

	A	B	n	C	m
Liutkus - Tension	1123	1602	.426	.0088	1.40
Liutkus – Compression	1142	1329	.396	.0038	-
Kobayashi	980	1370	.164	.02	1.03
Pereira	1350	1139	.6522	.0134	-

**Table 3.5: Johnson-Cook model parameter comparison.**

The various model predictions are plotted with representative experimental data for tests conducted at the nominal strain rate of  $1.0 \times 10^{-4} \text{ s}^{-1}$  in Figure 3.34. The new parameters closely match the experimental curve until specimen localization. Both the Pereira-Lerch and Kobayashi curves predict a slightly higher yield point. Kobayashi predicts greater strain hardening initially and a lower rate of strain hardening at larger strains. Pereira-Lerch predicts a lower, more constant rate of strain hardening.

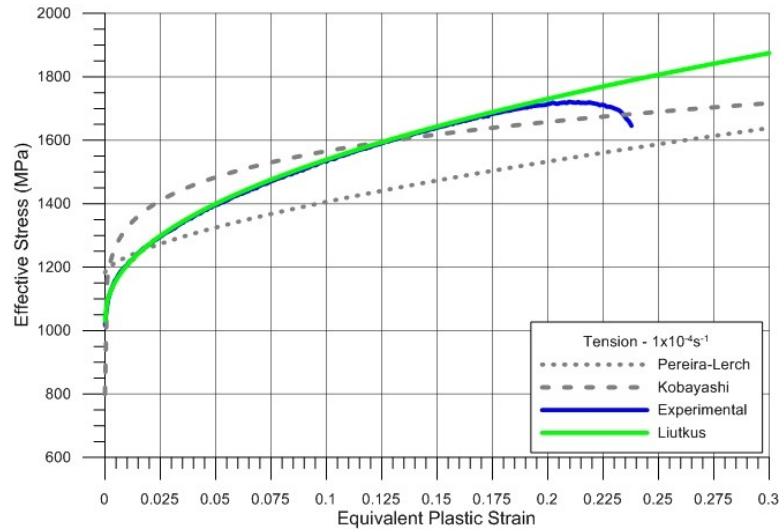


**Figure 3.34: Johnson-Cook curves and tension data at  $1.0 \times 10^{-4} \text{s}^{-1}$ .**

Figure 3.35 presents experimental data and model predictions for tension experiments conducted at  $2000 \text{s}^{-1}$ . The new model parameters closely match the data from yield until necking. The Pereira-Lerch curve estimates a 25% greater yield stress, but its lower rate of strain hardening brings it within 5% of the experimental stress near the necking point. The Kobayashi model predicts a much greater rate of strain rate hardening, which overestimates the stress at necking by about 400MPa.

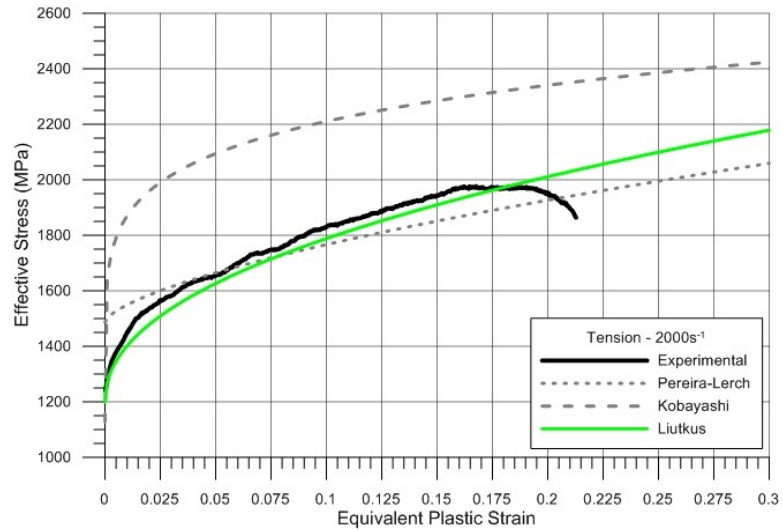


Figure 3.35: Johnson-Cook curves and tension data at  $2000s^{-1}$ .

The various Johnson-Cook model of rate sensitivity are summarized in Figure 3.36. The new parameters predict slightly less rate sensitivity than Pereira-Lerch, and much less rate sensitivity than Kobayashi.

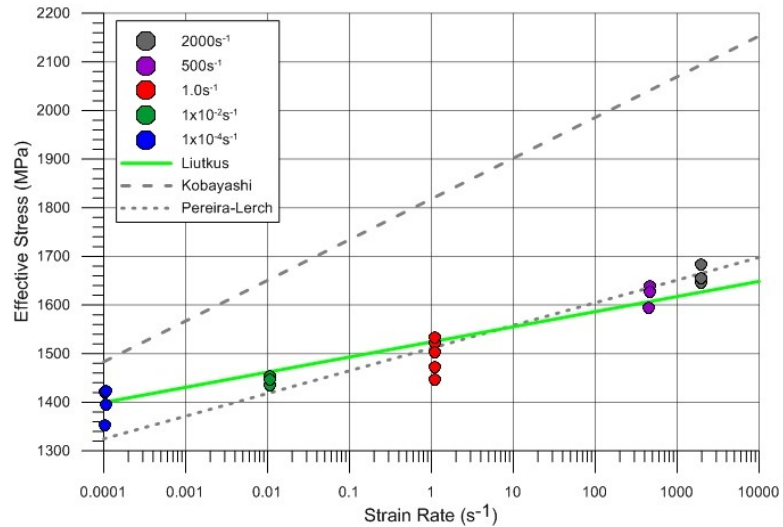
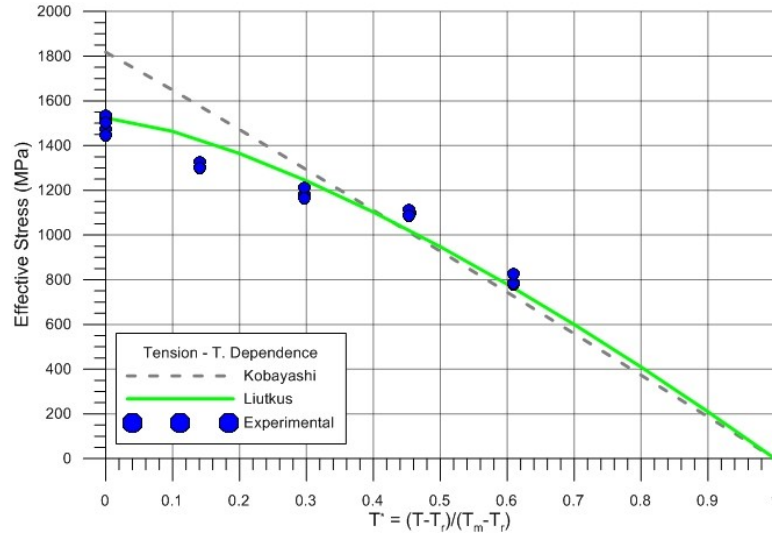


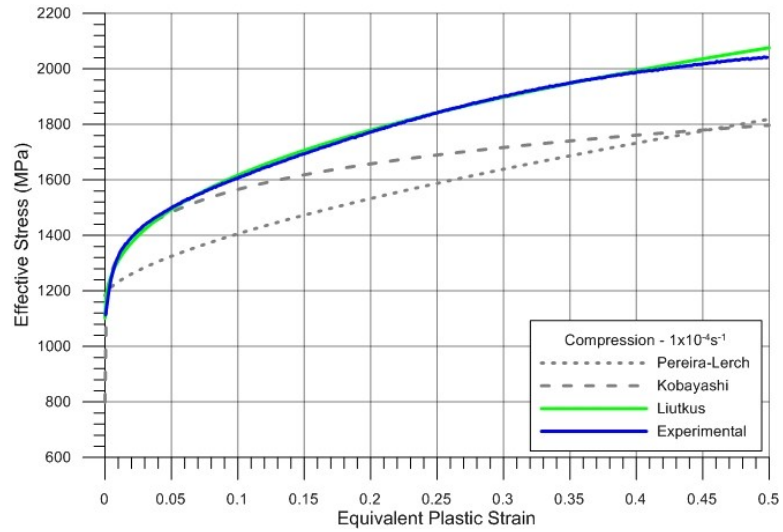
Figure 3.36: Model predictions and experimental data - true stress (MPa) at 5% strain versus strain rate.

Figure 3.37 summarizes the temperature dependence predicted by the Liutkus and Kobayashi curves by plotting the predicted effective stress at 5% strain as well as experimental data versus

the homologous temperature. The new parameters predict data at low temperatures much more accurately than the Kobayashi parameters. At temperatures above 600°C, the two sets of parameters predict nearly identical flow stress.

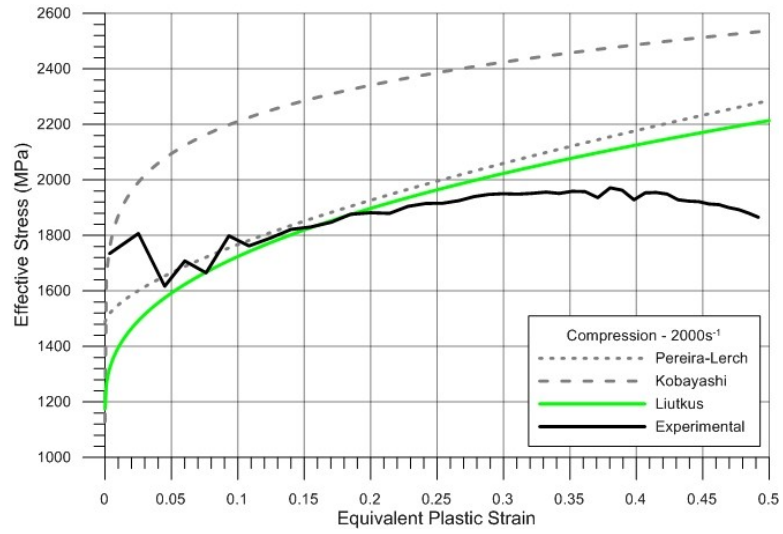


**Figure 3.37: Model predictions for tension temperature dependence. Effective stress at 5% strain versus  $T^*$ .** Johnson-Cook model predictions and experimental data from uniaxial compression experiments at  $1.0 \times 10^{-4} \text{ s}^{-1}$  are presented in Figure 3.38. All three sets of parameters predict the yield point accurately. The new parameters most closely matches the experimental data. The Kobayashi model matches up to 5% strain, where it predicts a lower strain hardening rate than that seen experimentally. The Pereira-Lerch model predicts a similar overall strain hardening rate, but does not predict the greater strain hardening immediately following yield.



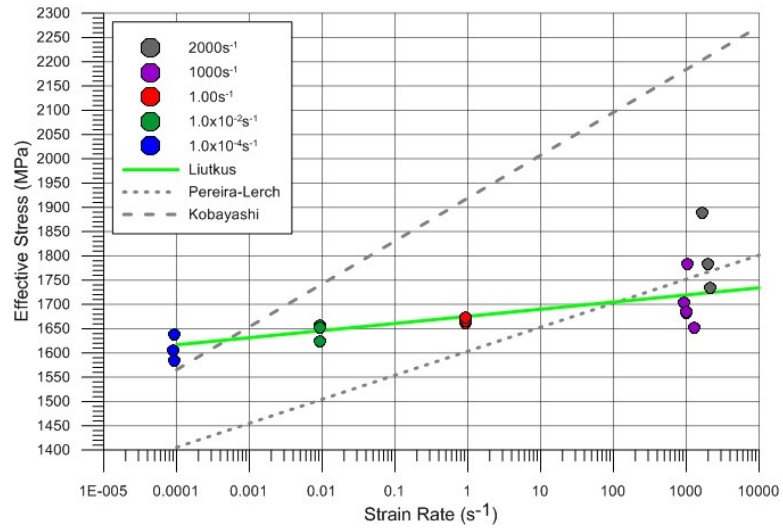
**Figure 3.38: Model predictions and experimental data for compression experiments at  $1.0 \times 10^{-4} \text{s}^{-1}$ .**

Figure 3.39 presents Johnson-Cook model predictions and experimental data for compression experiments at a nominal strain rate of  $2000 \text{s}^{-1}$ . Again, yield stress is difficult to evaluate due to force inequilibrium at low strain in SHB experiments. The Liutkus and Pereira – Lerch curves are similar, with Liutkus predicting lower yield but greater initial strain hardening. Both match the experimental data until roughly 17.5% strain, where the experimental strain hardening rate decreases.



**Figure 3.39: Model predictions and experimental data for compression experiments at  $2000s^{-1}$ .**

Data presented in Figure 3.40 compares the strain rate sensitivity predicted by each set of Johnson-Cook parameters with the compression experimental data. The data from this project shows less strain rate sensitivity in compression than that predicted by either Kobayashi or Pereira-Lerch.



**Figure 3.40: Johnson-Cook curve fits and experimental data for strain rate sensitivity. Effective stress @ 10% strain versus strain rate.**

### 3.5 Summary & Conclusions

Plastic flow behavior of precipitate hardened Inconel 718 is studied in tension and compression at various strain rates, specimen orientations, and temperatures. Multiple experiments are conducted for each test configuration.

Flat, dog-bone specimens loaded in tension show unique plastic flow behavior. The material exhibits significant strain hardening at all strain rates. The strain hardening rate at  $1.0\text{s}^{-1}$  is lower than that at  $1.0 \times 10^{-2}\text{s}^{-1}$ . This trend is likely due to thermal softening. Tension tests on specimens fabricated in various orientations suggest that the material is slightly anisotropic. Statistical analysis of this data suggests that the differences between data from each direction is significant. Elevated temperature experiments in tension show that the material strength decreases with temperature. Temperature's effect on ductility is more complex. Data between room temperature and  $600\text{ }^{\circ}\text{C}$  show a slight reduction in failure strain, while data from experiments at  $800\text{ }^{\circ}\text{C}$  shows elongation nearly 100% greater than that at room temperature. This behavior is consistent with data for Inconel 718 in the ASM Handbook [40].

Cylindrical specimens loaded in axial compression show similar compressive flow behavior. Again, the material shows significant strain hardening, and some strain rate dependence. The strain hardening rate at  $1.0\text{s}^{-1}$  is less than that at  $1.0 \times 10^{-2}\text{s}^{-1}$ . The rate sensitivity in compression is less than that in tension. Anisotropy tests show lower stress in the  $\pm 45^{\circ}$  directions and greater stress in the transverse direction when compared to the rolling direction. These results are statistically significant.

Johnson-Cook parameters are generated from both tension and compression experimental data. The plasticity curves generated by these parameters are compared with experimental data at all test conditions and existing Model predictions from the literature.

## Chapter 4: Inconel 718 Fracture Specimen Design

In addition to studying the plastic flow behavior of precipitate hardened Inconel 718, the ongoing project plans to investigate the failure of the material experimentally and to use that experimental data with concurrent finite element simulations to generate a failure surface for the material. The specimen geometries for this test series are designed here.

### 4.1 Introduction & Background

Characterizing the ductile fracture of material is necessary to properly model and analyze failure. Real engineering components are typically loaded in complex stress states, which can affect the failure strain of the material. Bai and Wierzbicki [9] examined a variety of specimen geometries and concluded that stress triaxiality has a strong effect on ductile fracture. Further research by Barsoum and Faleskog [10] suggested that stress triaxiality alone could not sufficiently describe fracture behavior and that the Lode parameter has a role in characterizing fracture as well. The stress triaxiality is defined as the ratio of mean stress,  $\sigma_m$ , to effective stress,  $\bar{\sigma}$ . This is shown below in Equations (24) – (26).

$$\sigma^* = \frac{\sigma_m}{\bar{\sigma}} \quad (24)$$

$$\sigma_m = \frac{1}{3} \sigma_{kk} = \frac{1}{3} (\sigma_{11} + \sigma_{22} + \sigma_{33}) \quad (25)$$

$$\bar{\sigma} = \left( \frac{3}{2} S_{ij} S_{ij} \right)^{\frac{1}{2}} \quad (26)$$

where,  $S_{ij}$ , is the deviatoric stress tensor:

$$S_{ij} = \sigma_{ij} - \frac{1}{3}\sigma_{kk}\delta_{ij} \quad (27)$$

The Lode parameter is defined as:

$$\bar{\theta} = -\frac{2\sigma_1 - \sigma_2 - \sigma_3}{\sigma_1 - \sigma_3} \quad (28)$$

where  $\sigma_1$ ,  $\sigma_2$ , and  $\sigma_3$  are the three principal stresses. It is possible to devise a fracture model that is dependent on both stress triaxiality and Lode parameter.

$$\bar{\epsilon}_f^p = f(\sigma^*, \bar{\theta}) \quad (29)$$

To adequately represent the stress-space, specimens must be designed that result in experimental data at a variety of data points in the triaxiality/lode parameter space. Finite element simulations are used to numerically predict the stress state of candidate specimen geometries for the test series.

## 4.2 Design Process & Final Geometries

The fracture test series on precipitate hardened Inconel 718 involves quasi-static tension experiments on thin, flat plane stress specimens, thick plane strain specimens, and axisymmetric specimens. The goal is to generate a fracture locus in the triaxiality – Lode parameter stress space for the material. The work closely follows the study of ductile fracture for Ti-6Al-4V performed by Hammer [6] and for 2024-T351 Aluminum performed by Seidt [43].

The plane stress and plane strain specimens are designed first. Simulations in LS-DYNA are conducted and the predicted stress state variables are recorded. Axisymmetric specimens were iteratively designed by attempting to match the triaxiality from specific plane stress and plane strain specimens.

Candidate specimen geometry is designed in SolidWorks, meshed in Hypermesh, and then simulated in LS-DYNA. Specimens are meshed such that the mesh length is 0.1524mm per element. This results in 5 elements across the thickness of plane stress geometries, 32 elements

across the minimum notch diameter of axisymmetric geometries, and 167 elements across the thickness of plane strain geometries. Representative meshes are shown in Figure 4.1.

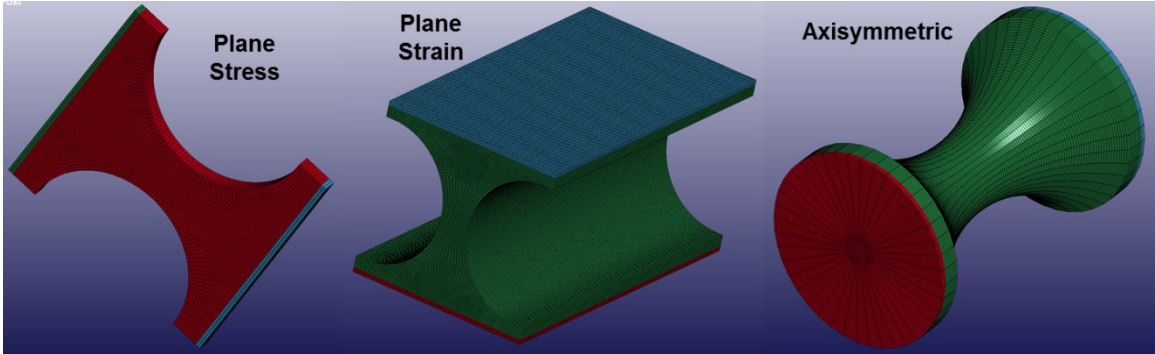


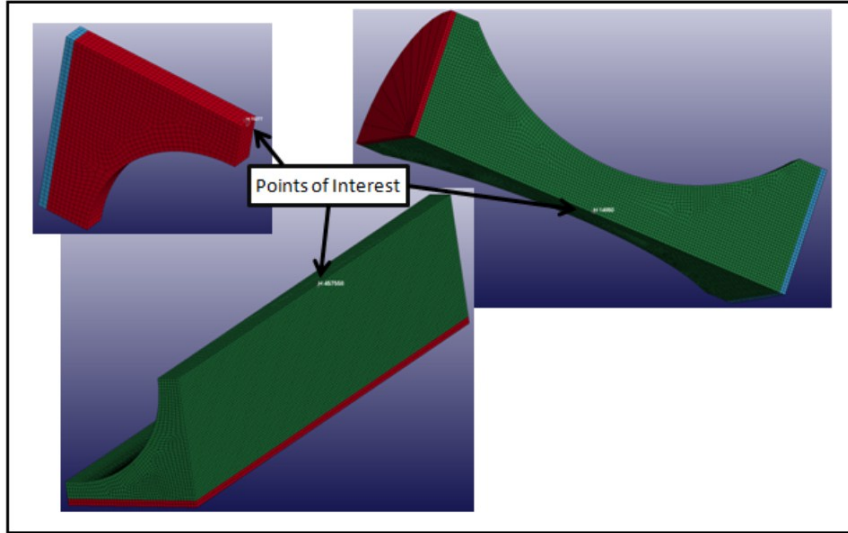
**Figure 4.1: Representative meshes for plane stress (left), plane strain (center), and axisymmetric (right) specimen geometries.**

Johnson-Cook model parameters determined by Kobayashi [29] (found in Table 3.5) were combined with a maximum principal strain based failure criterion, with the equivalent plastic failure strain,  $\varepsilon_p^f = 0.25$ , to model material behavior. One end of the specimen is given a constant velocity in the axial direction and the other is fixed. After the simulation is complete, data is extracted from an internal element – the element located at the center of the minimum notch width. These locations are highlighted in Figure 4.2. From this element, equivalent plastic strain and three principal stress histories are extracted. From this data, the average triaxiality is computed using the following equation.

$$\sigma_{avg}^* = \frac{1}{\bar{\varepsilon}_f^p} \int_0^{\bar{\varepsilon}_f^p} \sigma^* d\bar{\varepsilon} \quad (30)$$

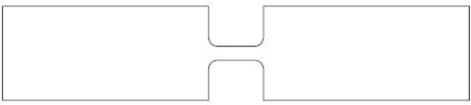
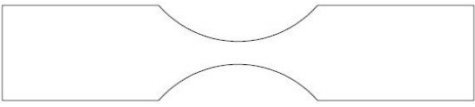
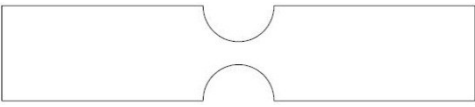
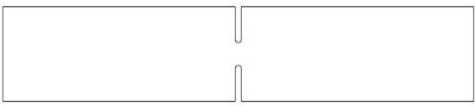
Where  $\bar{\varepsilon}_f^p$  is the equivalent plastic failure strain. The lode parameter is calculated using equation (31).

$$\bar{\theta}_{avg} = \frac{1}{\bar{\varepsilon}_f^p} \int_0^{\bar{\varepsilon}_f^p} \bar{\theta} d\bar{\varepsilon} \quad (31)$$



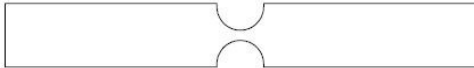
**Figure 4.2: Meshed geometries with arrows highlighting the location from which data is extracted in fracture specimen design process.**

The stress triaxiality for specimens in plane stress ranges between 0.33 and 0.57. The plane stress specimens are thus designed such that they cover this range. The geometry for plane stress specimens, their average triaxiality, and their lode parameter is shown below in Table 4.1. All plane stress samples are 63.5mm long. Stress triaxiality and lode parameter are calculated using principal stress data from LS-DYNA simulations and the average stress state equations presented above.

Test No.	Specimen Geometry	Dimensions	$\sigma^*$	$\bar{\theta}$
SG1		Thin Smooth Specimen Gage Length: 5.08mm Gage Width: 1.91mm Gage Thickness: 0.762mm	0.355	.943
SG2		Thin Large Notched Specimen Notch Radius: 14.29mm Min Notch Width: 3.05mm Thickness: 0.762mm	0.405	.753
SG3		Thin Medium Notched Specimen Notch Radius: 4.76mm Min Notch Width: 3.05mm Thickness: 0.762mm	0.476	.553
SG4		Thin Small Notched Specimen Notch Radius: 0.396mm Min Notch Width: 3.05mm Thickness: 0.762mm	0.574	.603

**Table 4.1: Plane stress fracture specimen geometry, stress triaxiality, and lode parameter.**

Wide specimens undergoing plane strain deformation are restricted to stress triaxialities greater than 0.57. The geometry for plane strain specimens, their average triaxiality and lode parameters are shown in Table 4.2. All plane strain samples are 95.25mm long. Stress triaxiality and Lode parameter are calculated in the same manner as described previously.

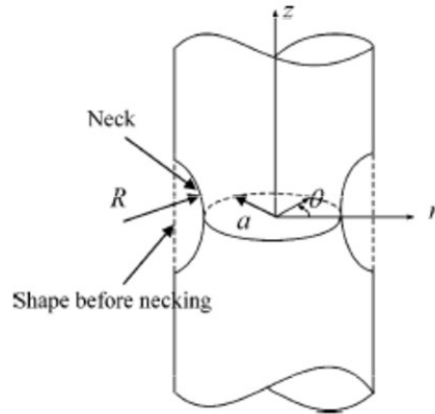
Test No.	Specimen Geometry	Dimensions	$\sigma^*$	$\bar{\theta}$
SG11		Thick Smooth Specimen Gage Length: 4.57mm Gage Width: 2.03mm Gage Thickness: 25.4mm	0.585	0.0635
SG12		Thick Large Notched Specimen Notch Radius: 12.7mm Min Notch Width: 2.03mm Thickness: 25.4mm	0.662	.0464
SG13		Thick Small Notched Specimen Notch Radius: 4.76mm Min Notch Width: 2.03mm Thickness: 25.4mm	0.761	0.0293

**Table 4.2: Plane strain fracture specimen geometry, stress triaxiality, and lode parameter.**

The axisymmetric geometry must be designed iteratively, in an effort to match the average stress triaxiality from each plane stress and plane strain specimen. The specimen design is deemed acceptable if the average stress triaxiality is within 5% of the target value. The first iteration of each design is developed using Bridgman's analytical solution for the stress state at the center of a necked sample [44]. The Bridgman equation is

$$\sigma^* = \frac{1}{3} + \ln\left(1 + \frac{a}{2R}\right) \quad (32)$$

Where  $a$  is the minimum cross-section radius and  $R$  is the required notch radius. This geometry is illustrated in Figure 4.3 [45].

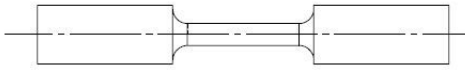
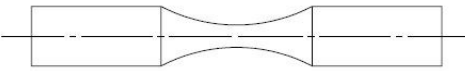
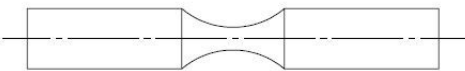
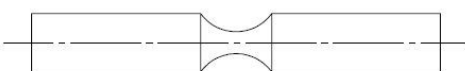
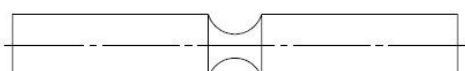
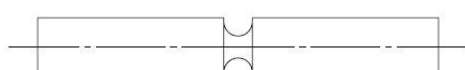


**Figure 4.3: Necked sample geometry as used in Bridgman's equation.**

Since the desired stress triaxiality is known as well as the initial value of the cross-section radius,  $a$ , the equation can be rewritten to solve for  $R$ . However, due to localization prior to failure, the stress triaxiality evolves and the actual triaxiality will likely not match the value predicted by Bridgman's equation. The initial geometries are meshed and simulated and their results are compared to the goal triaxiality. The notch radius is modified, and the new geometry is simulated and compared until the triaxiality value predicted by the LS-DYNA simulation results is within 5% of the goal triaxiality. Generally, triaxiality is inversely proportional to notch radius, and this fact informs the necessary adjustments to notch radius from one design to the next.

A total of 10 geometries for axisymmetric specimens were evaluated in LS-DYNA. From these results, six final geometries were determined, see Table 4.3. Specimen SG10 provides an additional data point at high triaxiality and is not intended to match another sample. Specimen SG7 is designed to match plane stress specimen SG4. Its average triaxiality is 2.09% lower than that of the plane stress specimen. Specimen SG6 is designed to match specimen SG3, and it predicts an average triaxiality 3.36% greater than the plane stress specimen. Specimens SG8 and SG9 are designed to match plane strain specimens SG12 and SG13 respectively. The former predicts a stress triaxiality 1.66% lower than its plane strain counterpart, and the latter predicts a

value 0.92% greater than its plane strain counterpart. All axisymmetric specimens have an overall length of 88.9mm. The Lode parameter is 1.0 for all axisymmetric specimens due to symmetry.

Test No.	Specimen Geometry	Dimensions	$\sigma^*$	$\bar{\theta}$
SG5		Axisymmetric Smooth Specimen Gage Length: 24.13mm Gage Diameter: 4.76mm	0.378	1.0
SG6		Axisymmetric Notched Specimen Notch Radius: 35.72mm Gage Diameter: 4.76mm	0.492	1.0
SG7		Axisymmetric Notched Specimen Notch Radius: 17.46mm Gage Diameter: 4.76mm	0.562	1.0
SG8		Axisymmetric Notched Specimen Notch Radius: 9.53mm Gage Diameter: 4.76mm	0.651	1.0
SG9		Axisymmetric Notched Specimen Notch Radius: 5.56mm Gage Diameter: 4.76mm	0.768	1.0
SG10		Axisymmetric Notched Specimen Notch Radius: 3.18mm Gage Diameter: 4.76mm	0.942	1.0

**Table 4.3: Axisymmetric fracture specimen geometry, average stress triaxialty, and lode parameter.**

This test plan will determine if stress triaxiality alone is enough to accurately model the failure behavior of precipitate hardened Inconel 718. If triaxiality alone is sufficient, the failure strains from specimens with the same stress triaxiality should show identical failure strains. If this is not the case, the stress state is not the same, which is highlighted by the different Lode parameter.

### 4.3 Summary & Conclusions

Geometry is introduced for the study of ductile fracture under uniaxial tensile loadings for precipitate hardened Inconel 718. These plane stress, plane strain, and axisymmetric geometries

are designed to generate experimental data over a range of different stress triaxialities,  $\sigma^*$ , and lode parameters,  $\bar{\theta}$ . Prior work has shown that these two variables are related to ductile fracture, and recent failure models have used relationships between them to define the equivalent plastic failure strain. Specifically, the design of axisymmetric specimens is aimed to match the stress triaxiality of the large and medium notched plane stress specimens as well as the large and medium notched plane strain specimens. A full study of ductile fracture, using these geometries, will be completed in later work.

## **Appendix A: Principal Strain Histories – 3D DIC in Punch Experiments**

This appendix contains principal strain histories measured using 3D digital image correlation for static and dynamic punch experiments. These come from punch experiments using the sharp (6.35mm tip radius) and hemispherical (12.17mm tip radius) punch geometries. Strain histories from the blunt (0.97 mm corner radius) punch experiments are not included because the failure point could not be observed. Detailed discussion of these results takes place in Chapter 5.

## A.1 Sharp Punch Experiments

### A.1.1 Quasi-Static Experiments

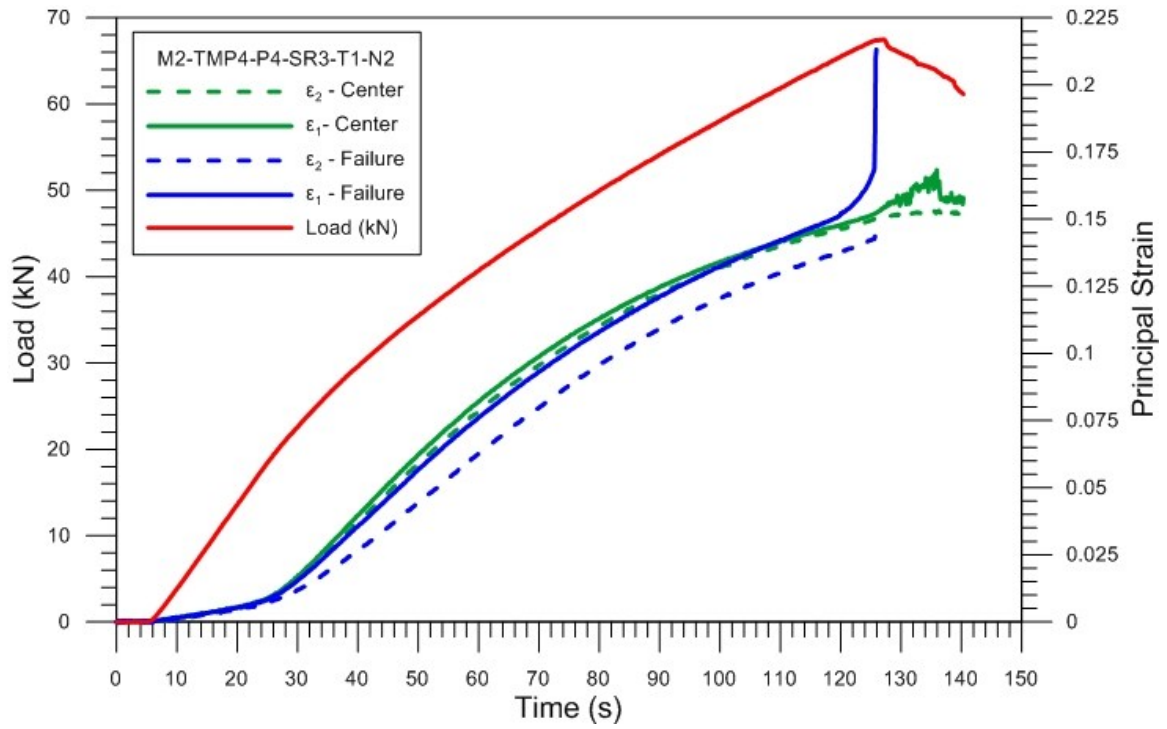


Figure A.1: Principal strain and load history for a quasi-static punch test using the sharp punch geometry.

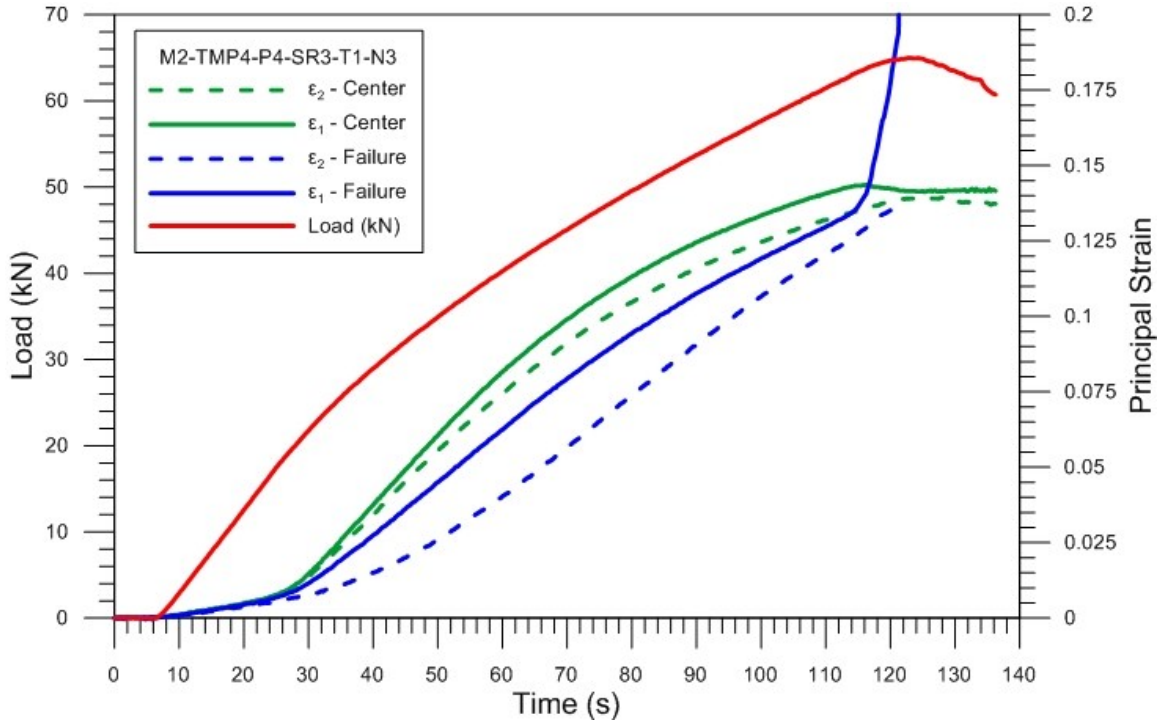


Figure A.2: Principal strain and load history for a quasi-static punch test using the sharp punch geometry.

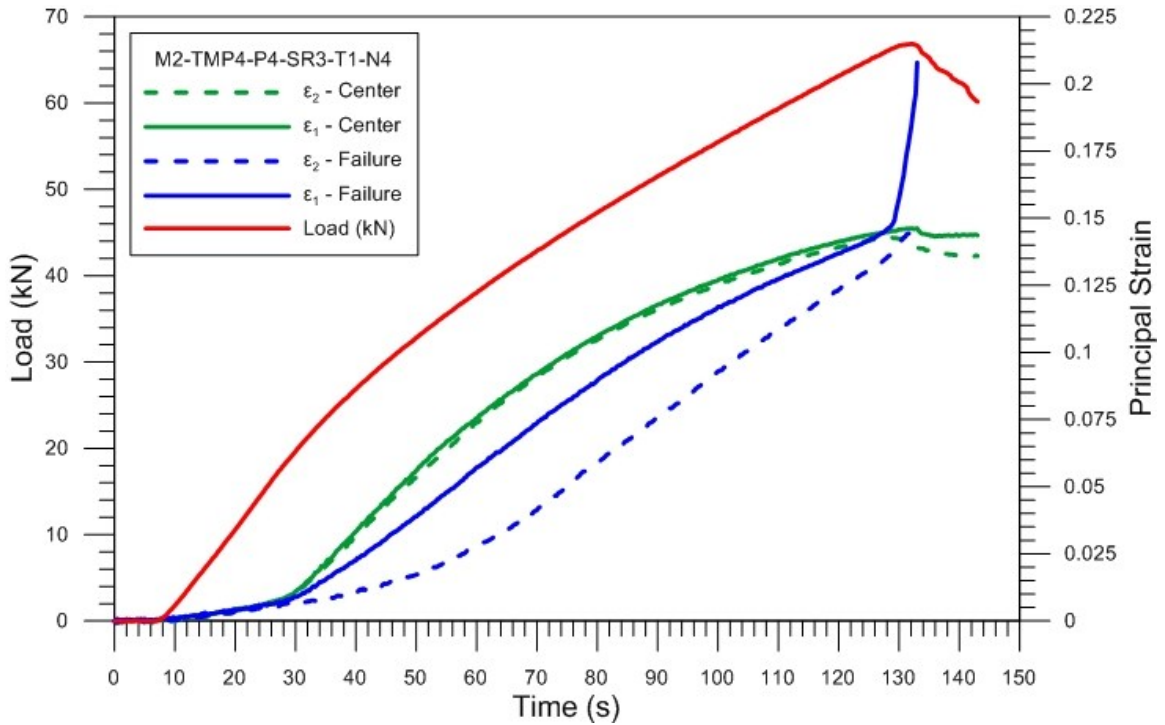


Figure A.3: Principal strain and load history for a quasi-static punch test using the sharp punch geometry.

### A.1.2 Dynamic Punch Experiments

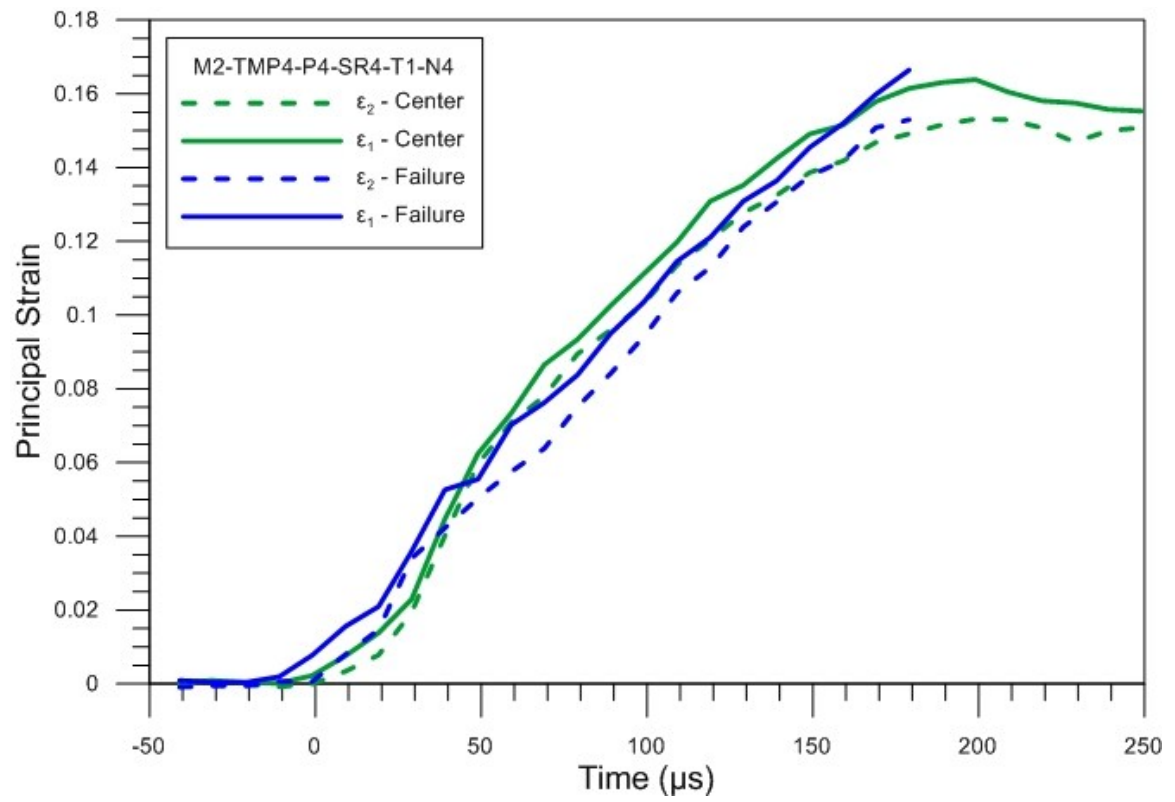


Figure A.4: Principal strain history for a dynamic punch experiment using the sharp punch geometry.

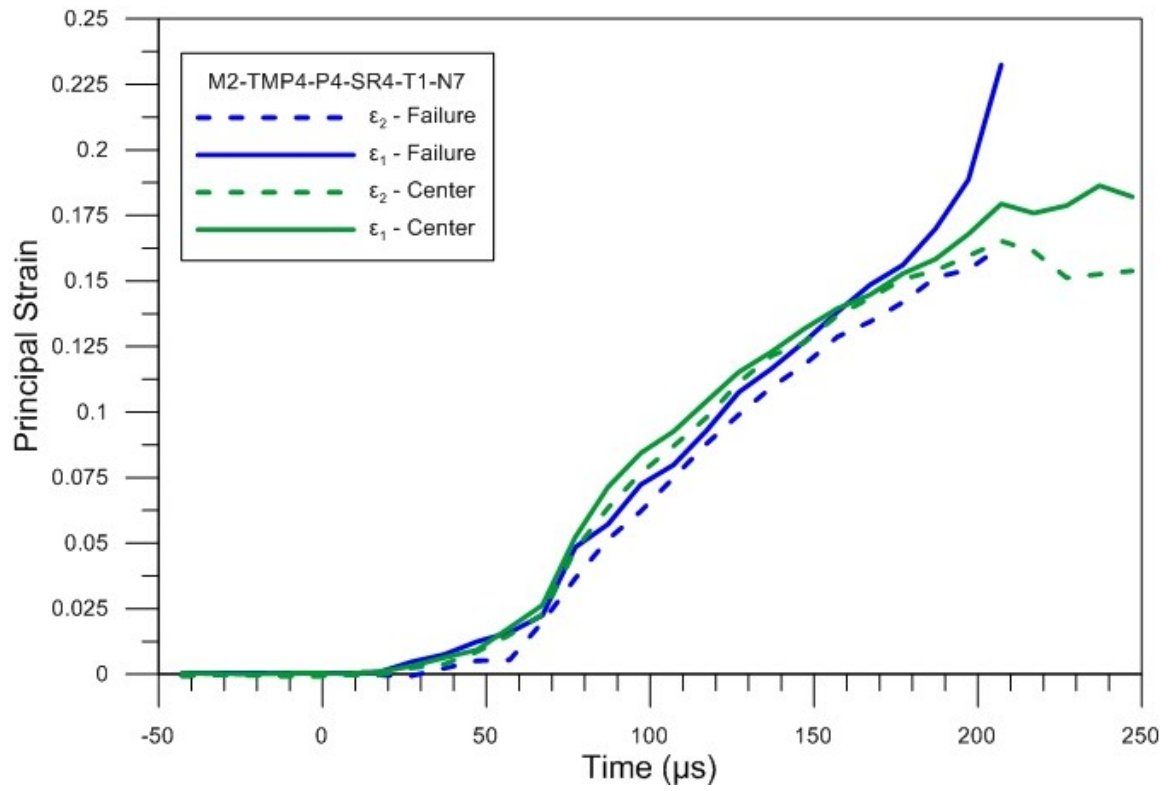


Figure A.5: Principal strain history for a dynamic punch experiment using the sharp punch geometry.

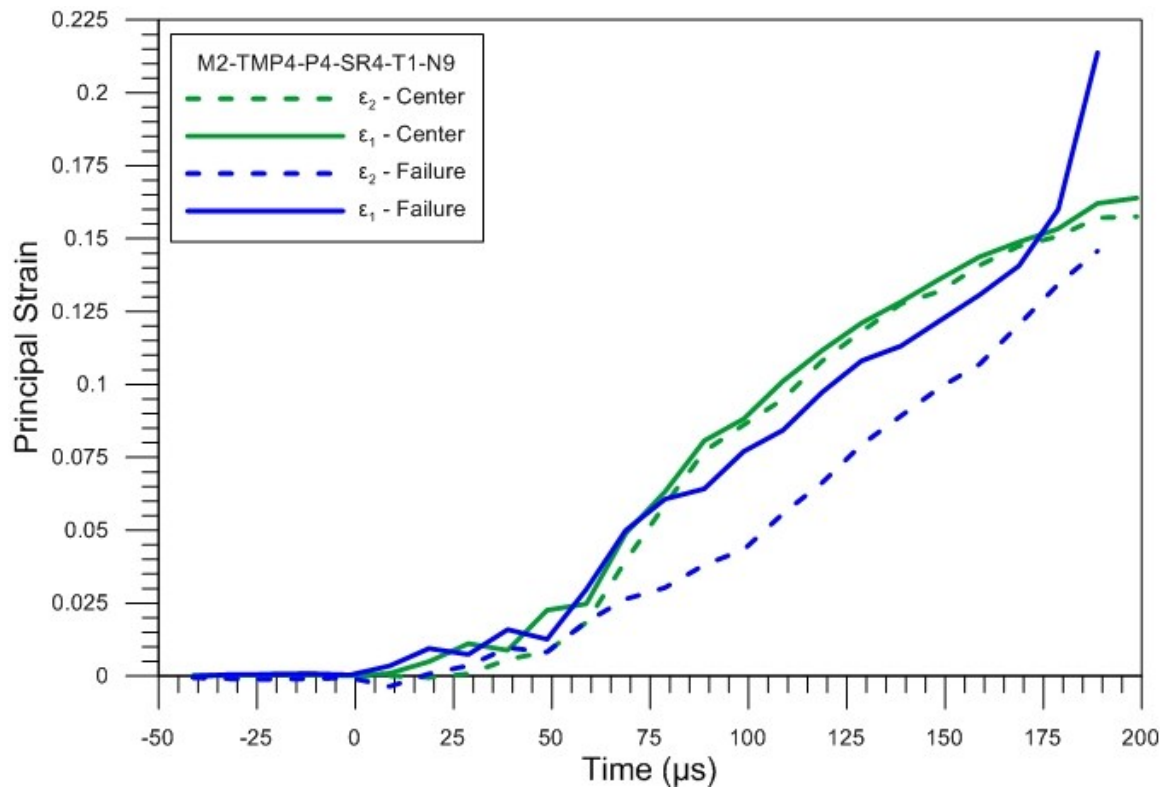


Figure A.6: Principal strain history for a dynamic punch experiment using the sharp punch geometry.

## A.2 Hemispherical Punch Experiments

### A.2.1 Quasi-static Experiments

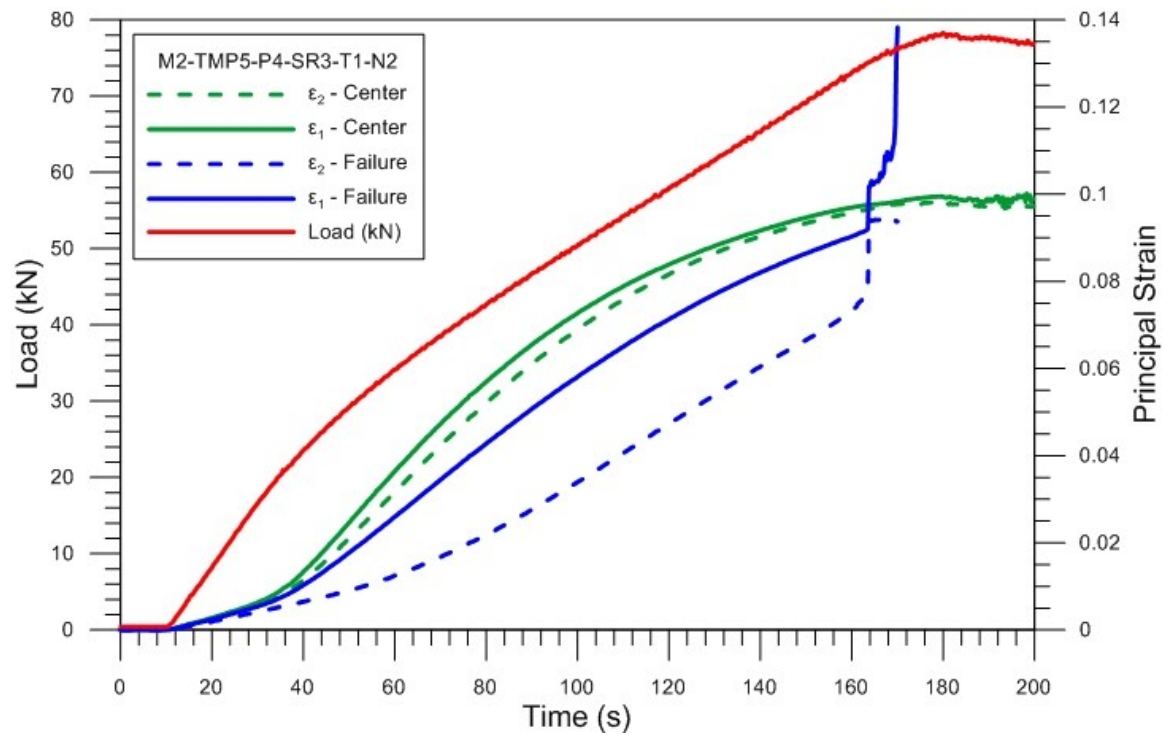


Figure A.7: Principal strain and load history for a quasi-static punch experiment with the hemispherical punch geometry.

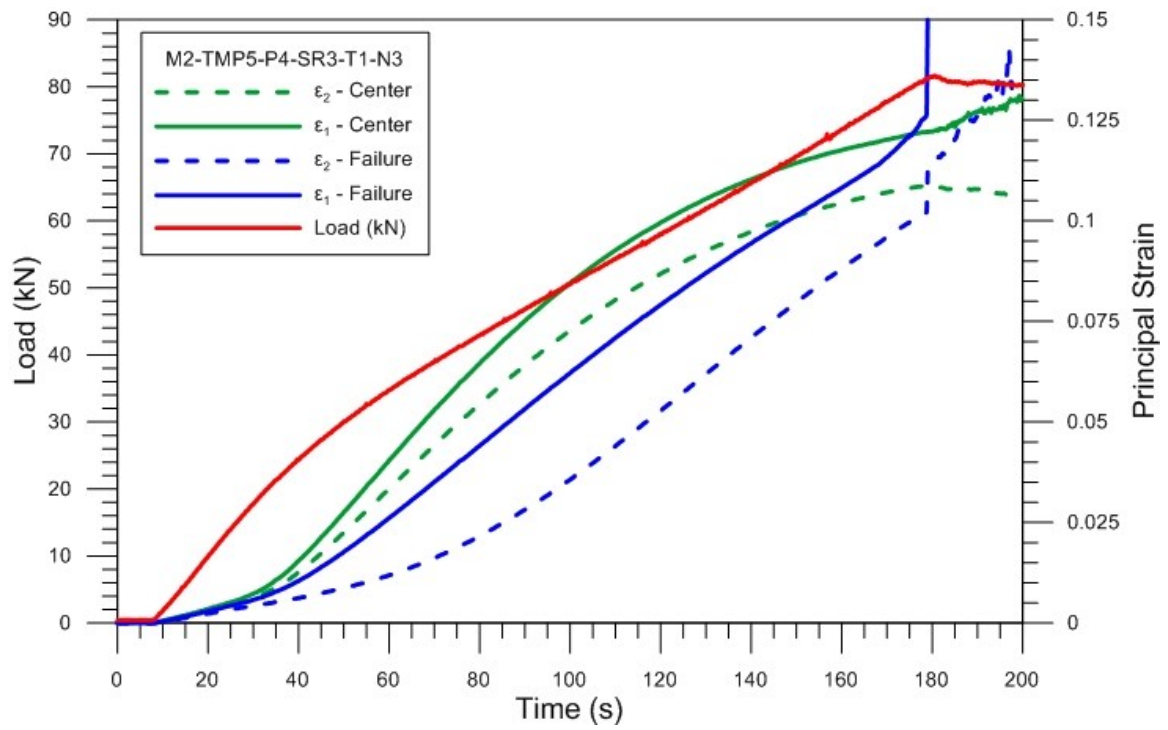
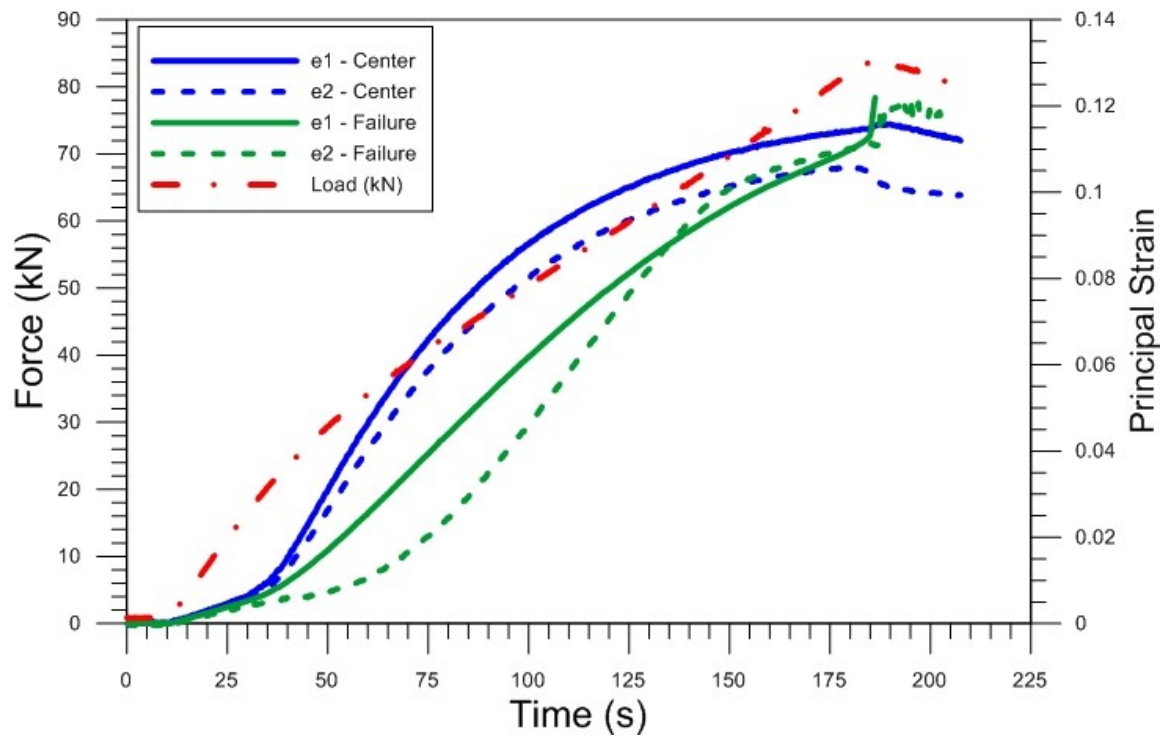


Figure A.8: Principal strain and load history for a quasi-static punch experiment with the hemispherical punch geometry.



**Figure A.9: Principal strain and load history for a quasi-static punch experiment with the hemispherical punch geometry.**

## A.2.2 Dynamic Experiments

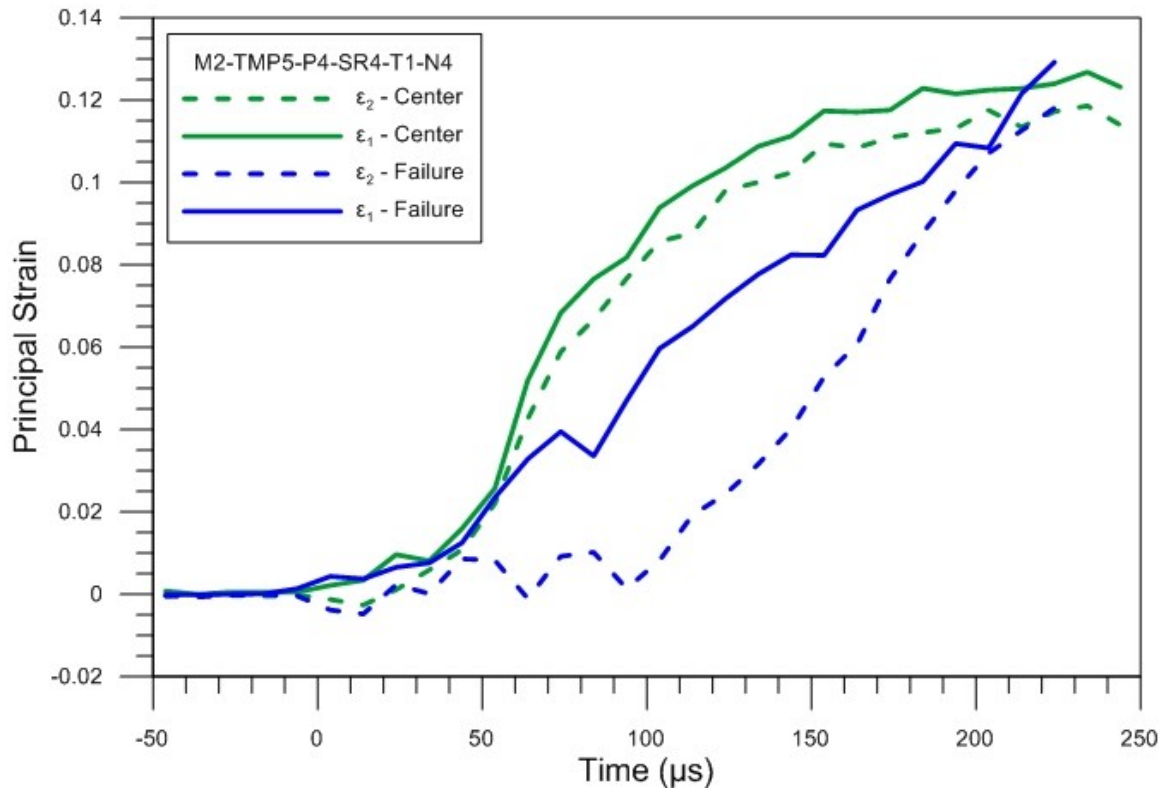


Figure A.10: Strain history for a dynamic punch experiment using the hemispherical punch geometry.

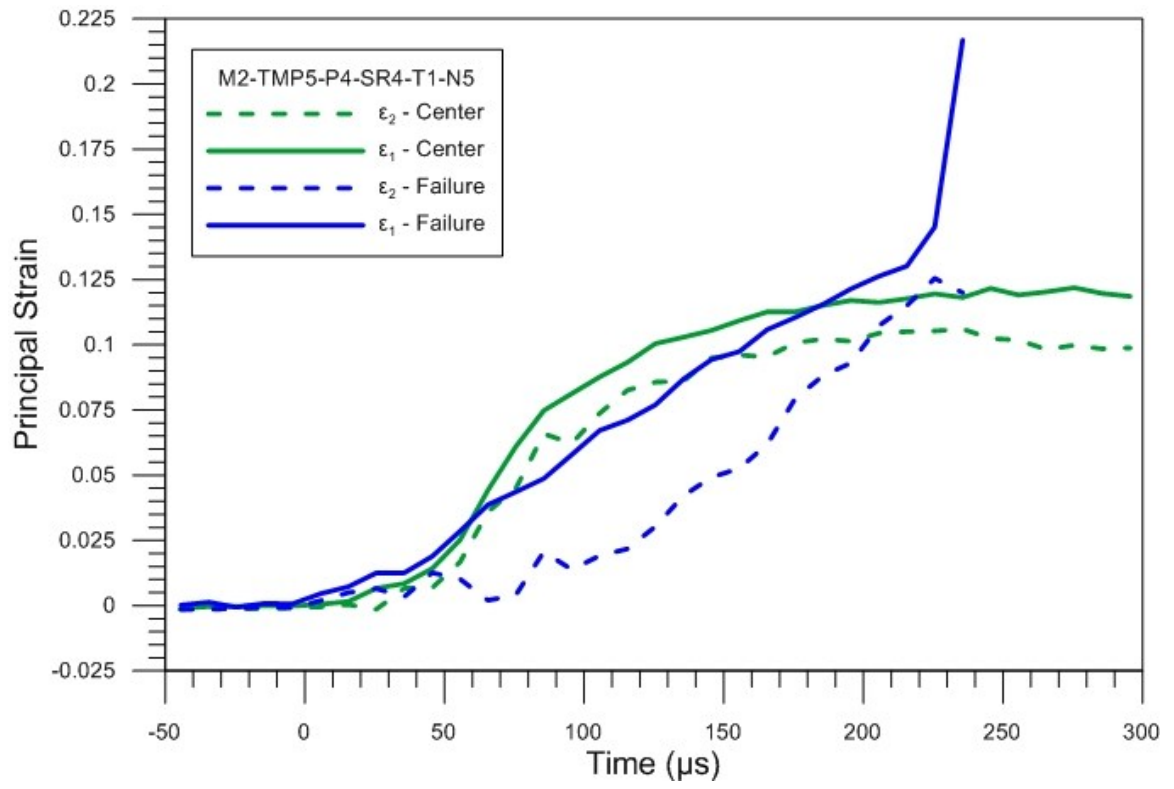


Figure A.11: Strain history for a dynamic punch experiment using the hemispherical punch geometry.

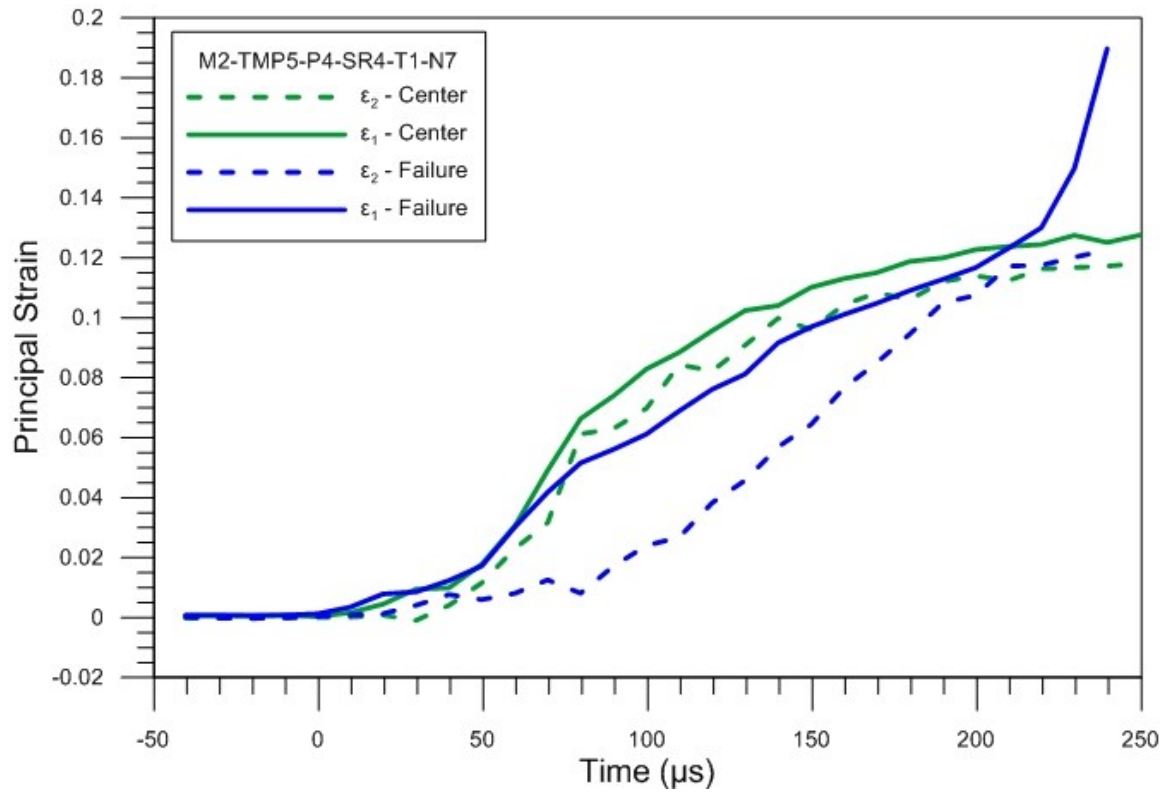


Figure A.12: Strain history for a dynamic punch experiment using the hemispherical punch geometry.

## **Appendix B: Full Experimental Results – Precipitate Hardened Inconel 718**

Full experimental results for the plastic deformation of Inconel 718 are presented here. Data is presented in true stress versus true strain curves. Representative data and discussion was presented in Chapter 3.

## B.1 Experimental Results: Tension Strain Rate Sensitivity

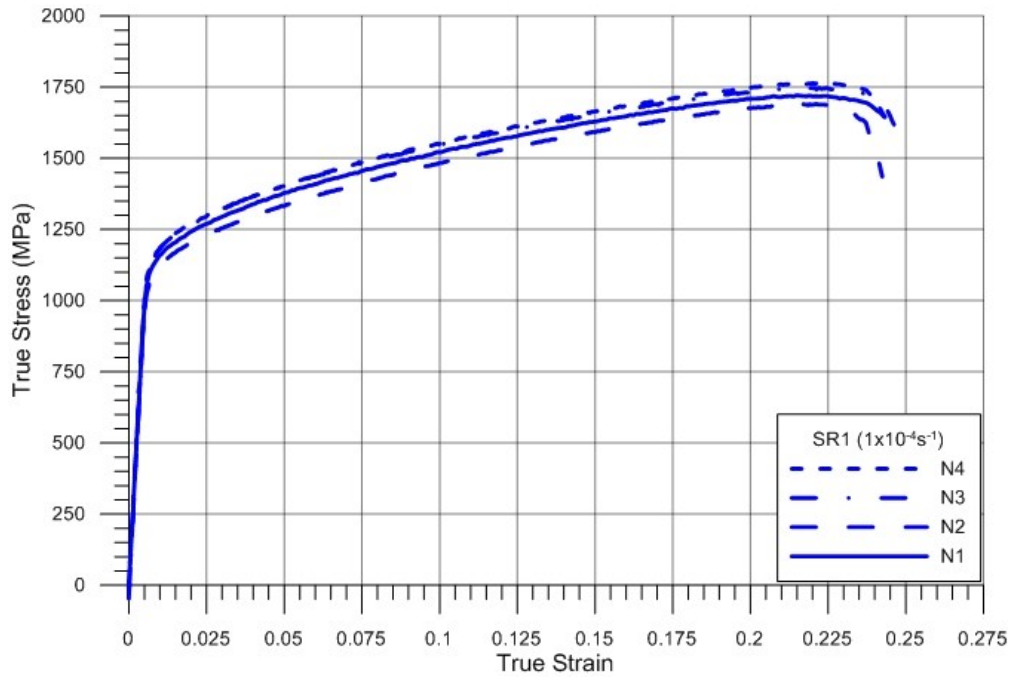


Figure B.1: Experimental results from tension experiments at  $1.0 \times 10^{-4} \text{ s}^{-1}$ .

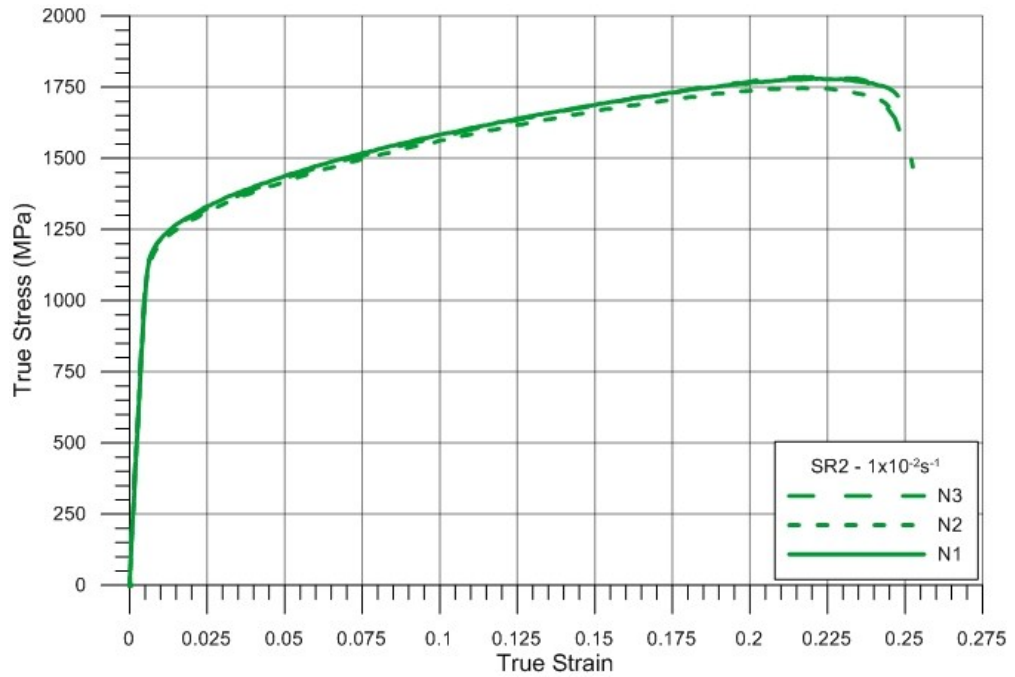


Figure B.2: Experimental results from tension experiments at  $1.0 \times 10^{-2} \text{ s}^{-1}$ .

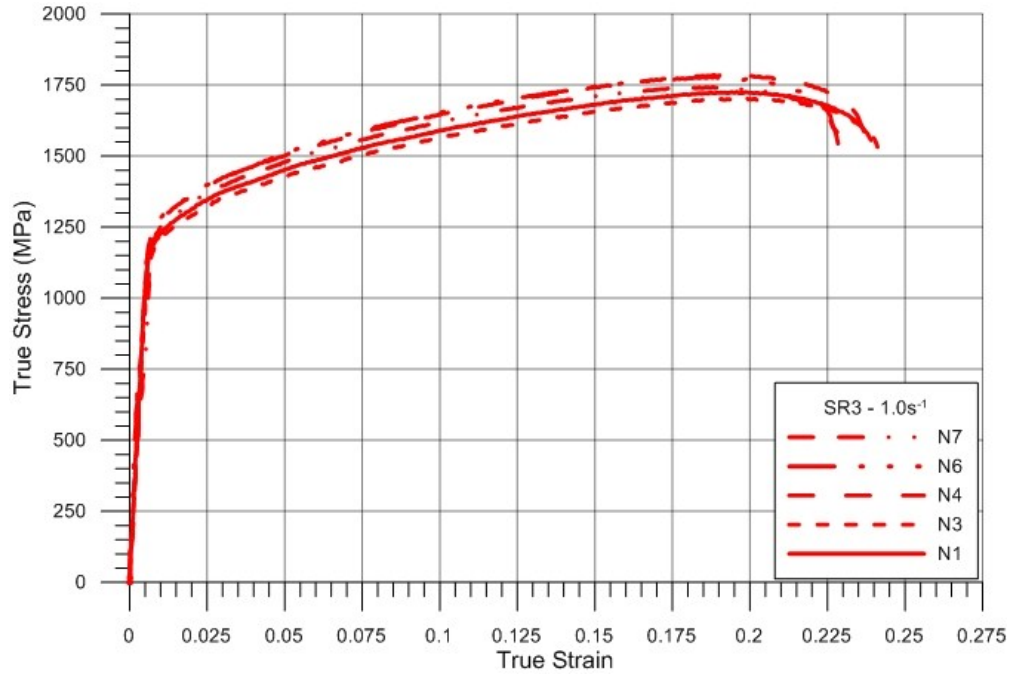


Figure B.3: Experimental results from tension experiments at  $1.00\text{s}^{-1}$ .

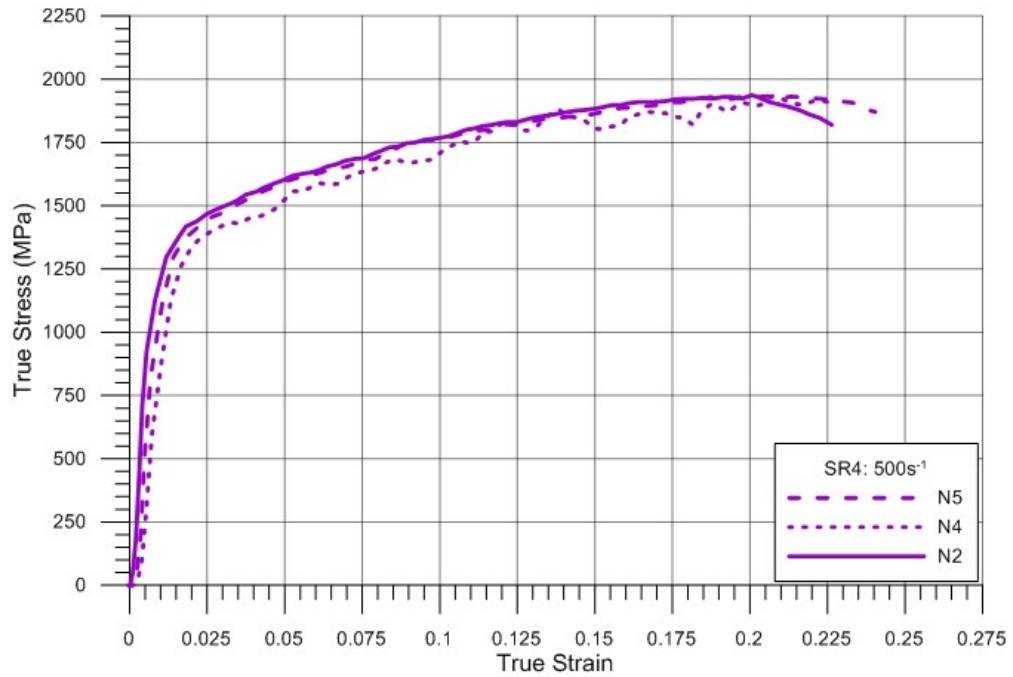
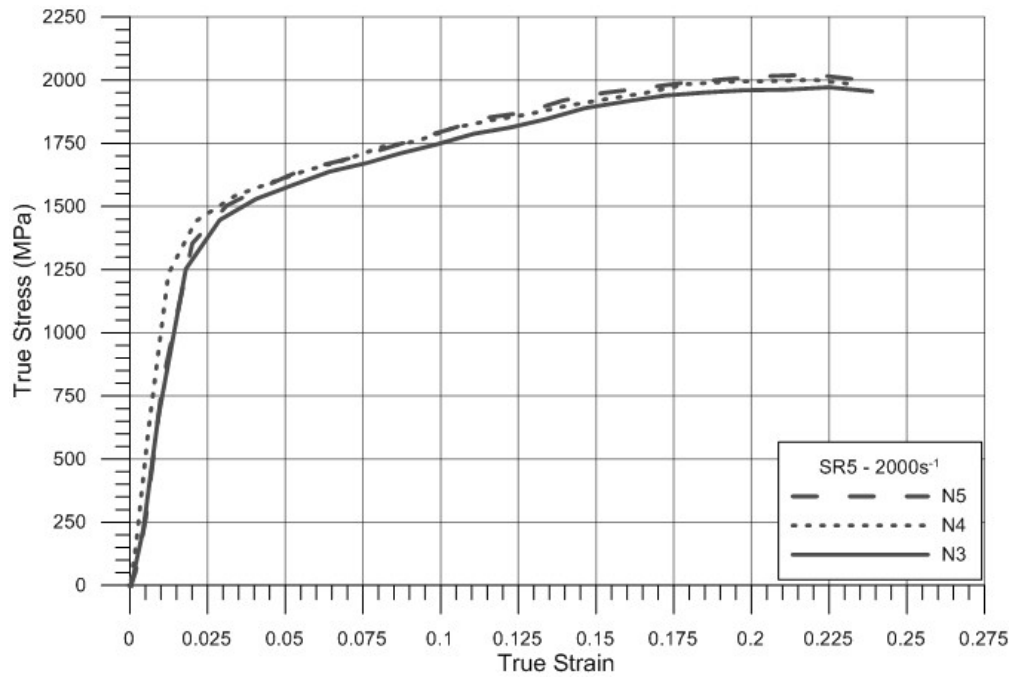


Figure B.4: Experimental results from tension experiments at  $500\text{s}^{-1}$ .



**Figure B.5: Experimental results for tension experiments conducted at  $2000s^{-1}$ .**

## B.2 Experimental Results: Tension Anisotropy

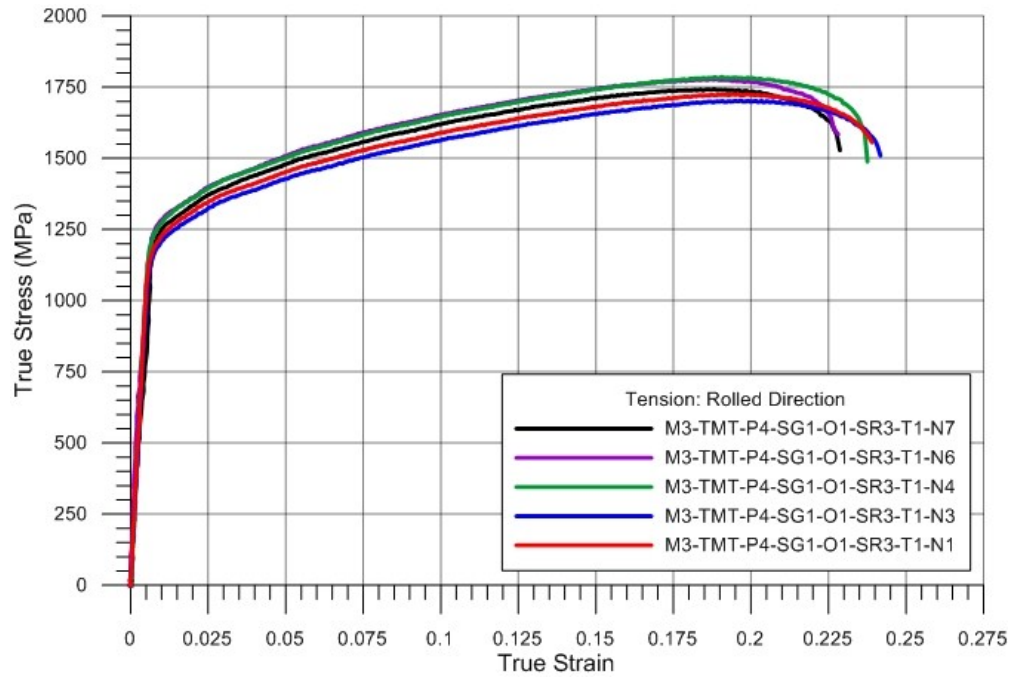


Figure B.6: Experimental results for tension experiments conducted at  $1.00s^{-1}$  in the rolled direction

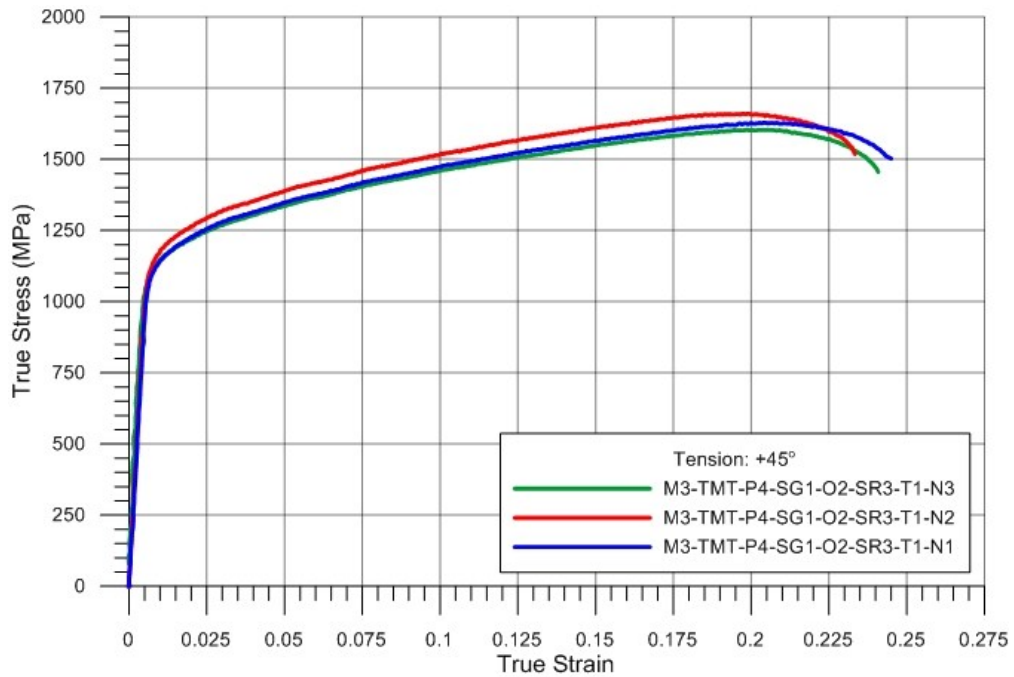


Figure B.7: Experimental results for tension experiments conducted at  $1.00s^{-1}$  in the +45° direction.

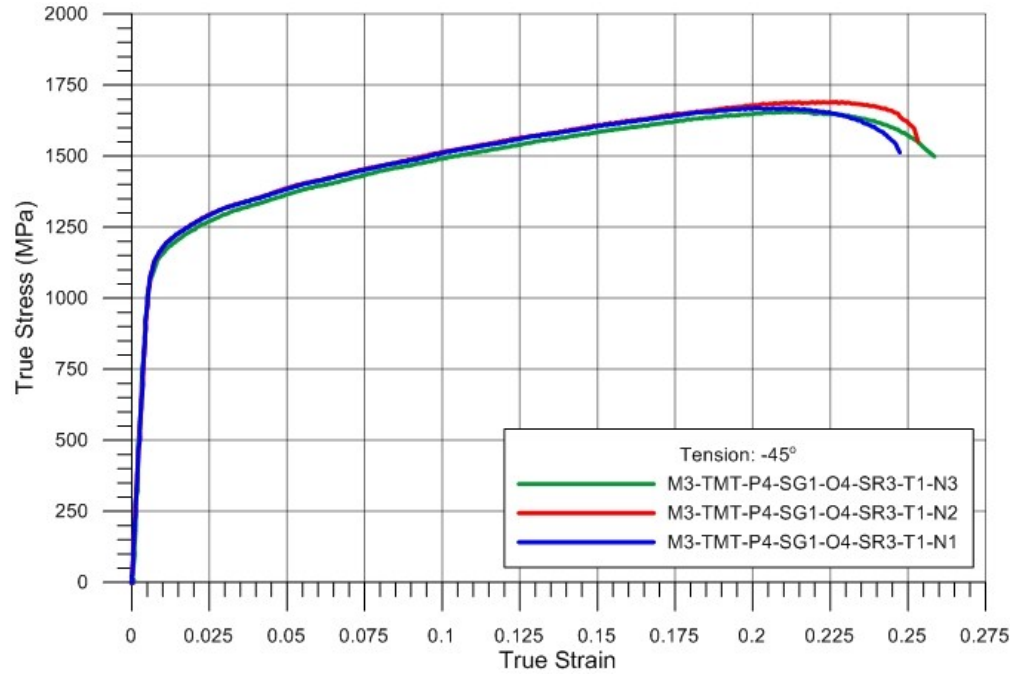


Figure B.8: Experimental Results for tension experiments conducted at  $1.00s^{-1}$  in the  $-45^\circ$  direction.

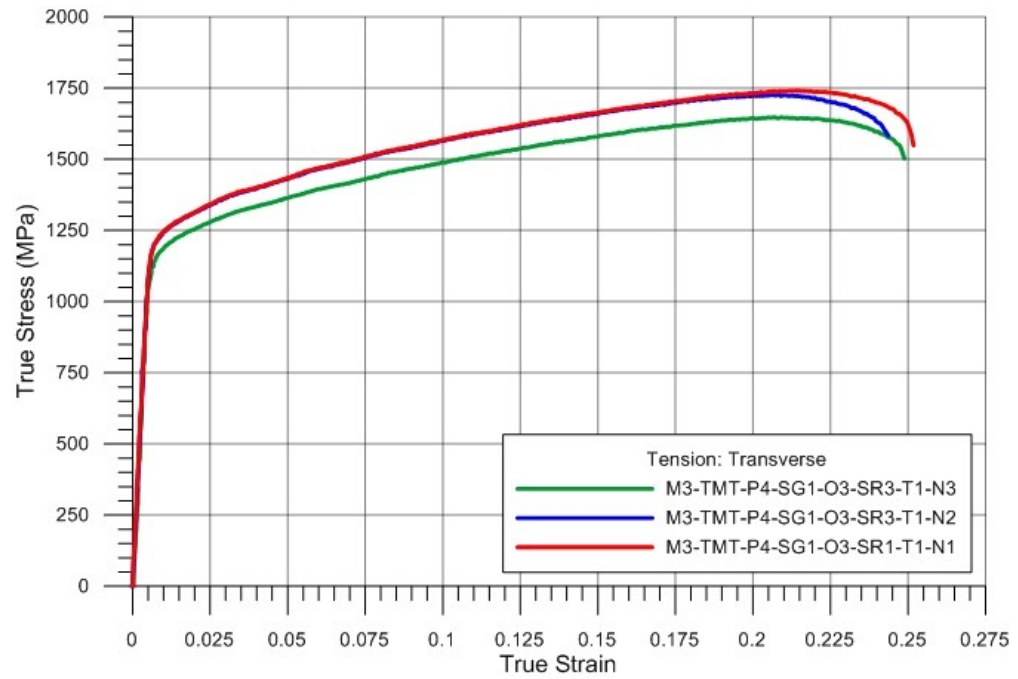


Figure B.9: Experimental Results for Tension Experiments conducted at  $1.00s^{-1}$  in the Transverse Direction

### B.3 Experimental Results: Compression Strain Rate Sensitivity

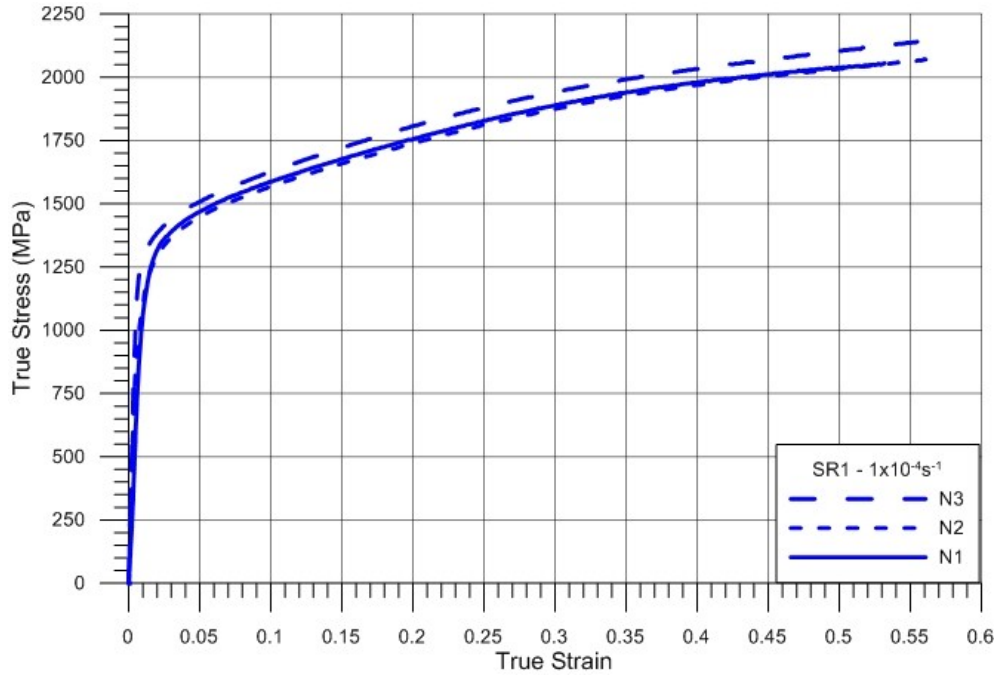


Figure B.10: Experimental results for compression experiments conducted at  $1.0 \times 10^{-4} \text{ s}^{-1}$ .

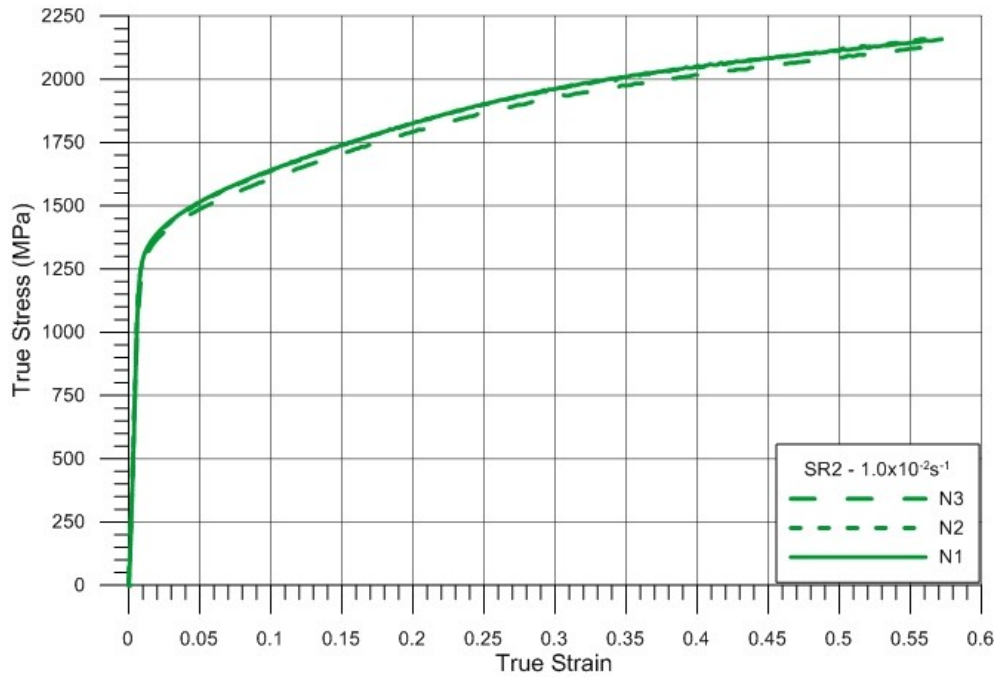


Figure B.11: Experimental results for compression experiments conducted at  $1.0 \times 10^{-2} \text{ s}^{-1}$ .

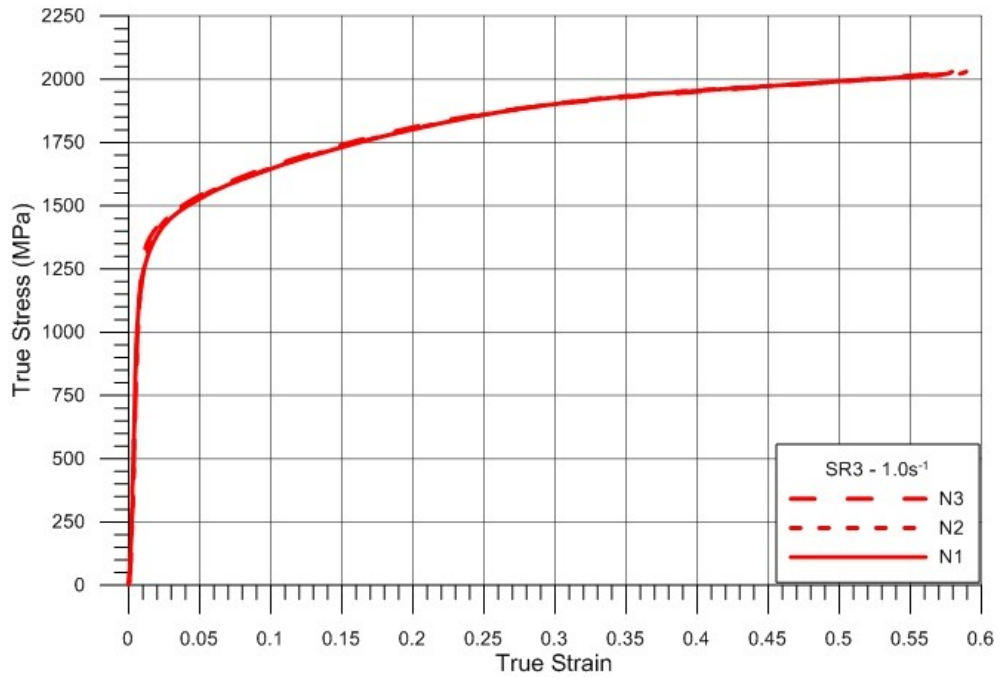


Figure B.12: Experimental results for compression experiments conducted at  $1.00s^{-1}$ .

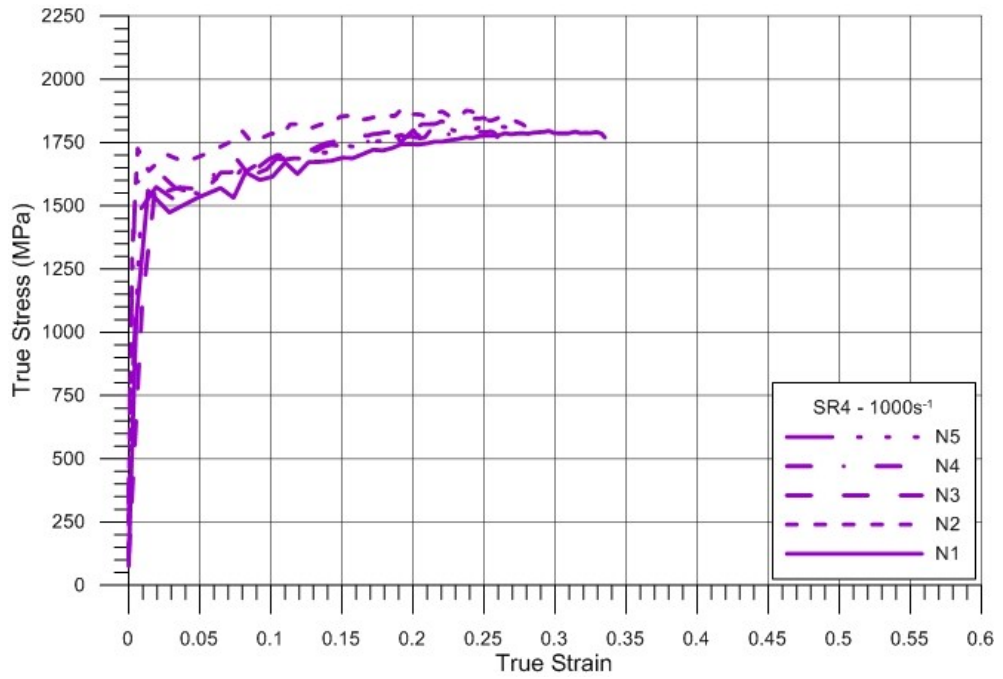


Figure B.13: Experimental results for compression experiments conducted at  $1000s^{-1}$ .

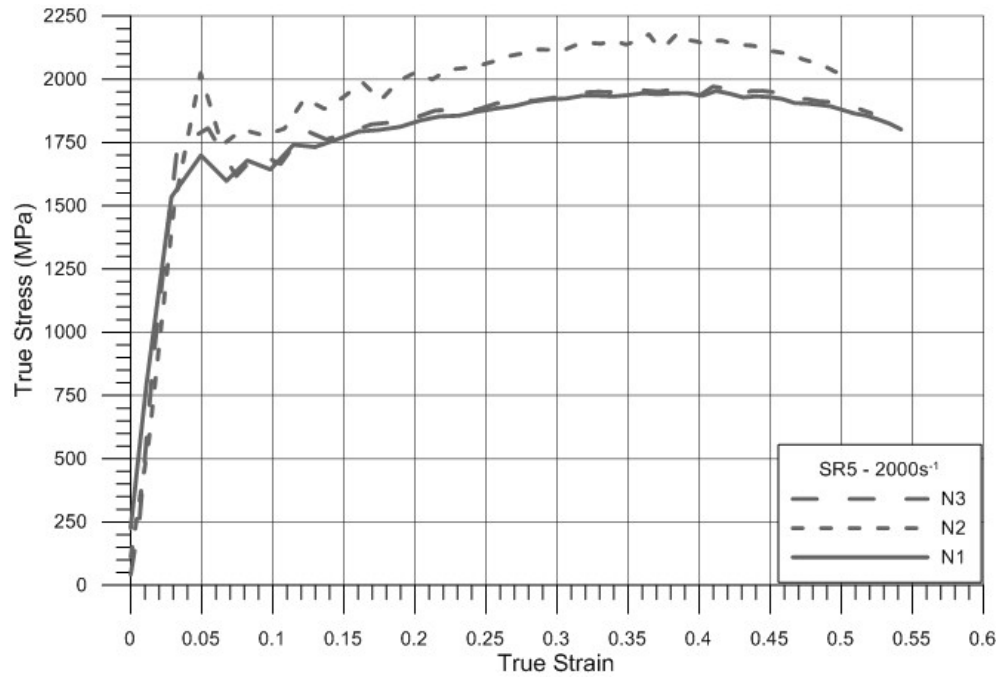


Figure B.14: Experimental results for compression experiments conducted at 2000s<sup>-1</sup>.

## B.4 Experimental Results: Compression Anisotropy

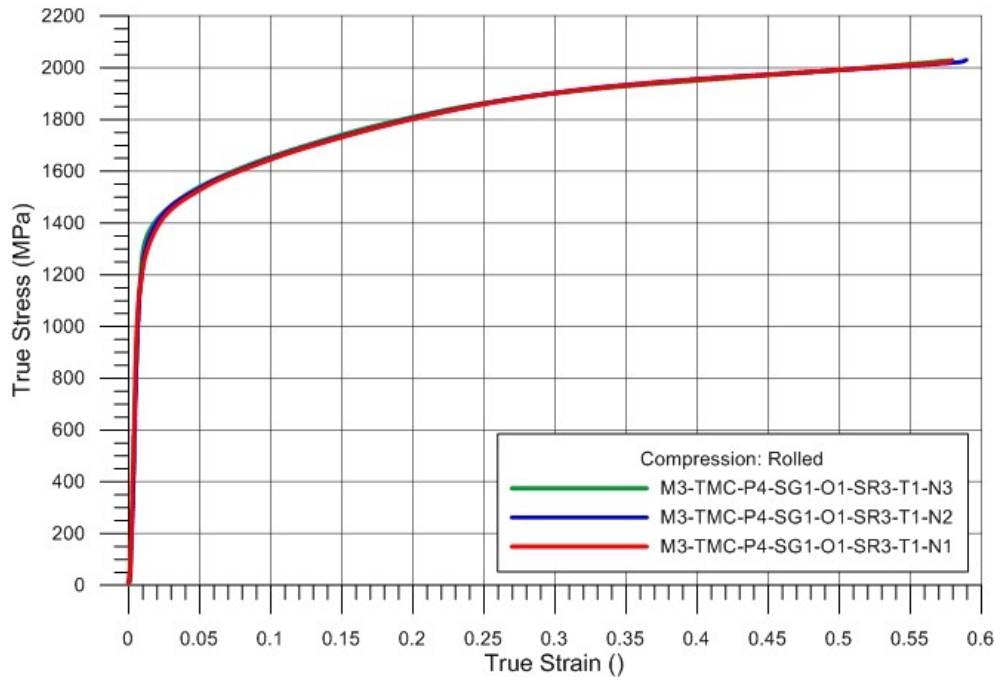


Figure B.15: Experimental results for compression experiments conducted at  $1.00s^{-1}$  in the rolled direction

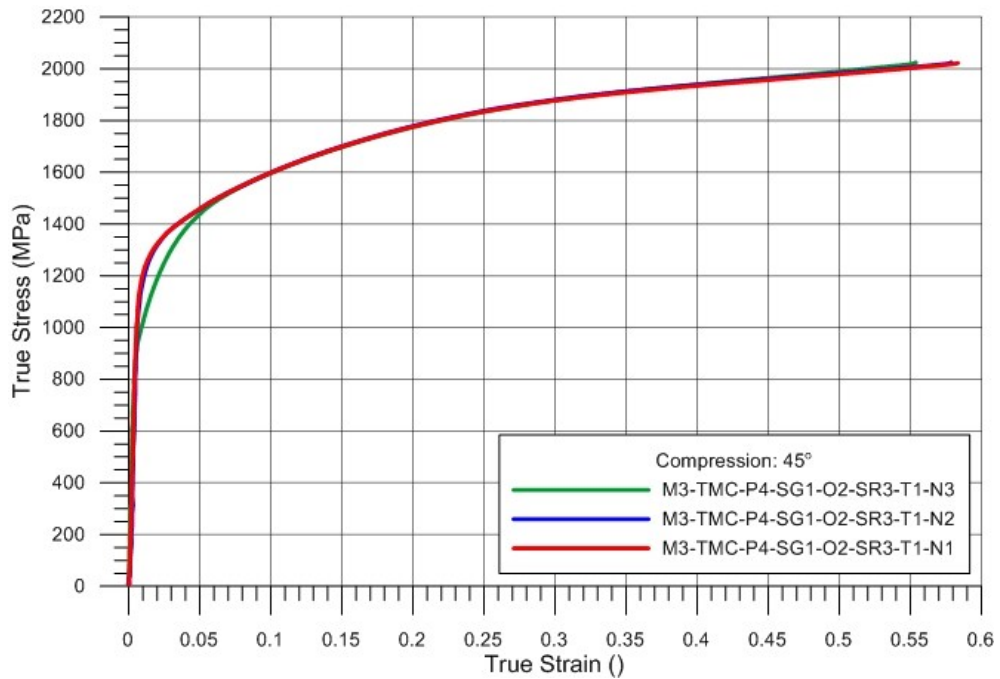


Figure B.16: Experimental results for compression experiments conducted at  $1.00s^{-1}$  in the  $45^\circ$  direction.

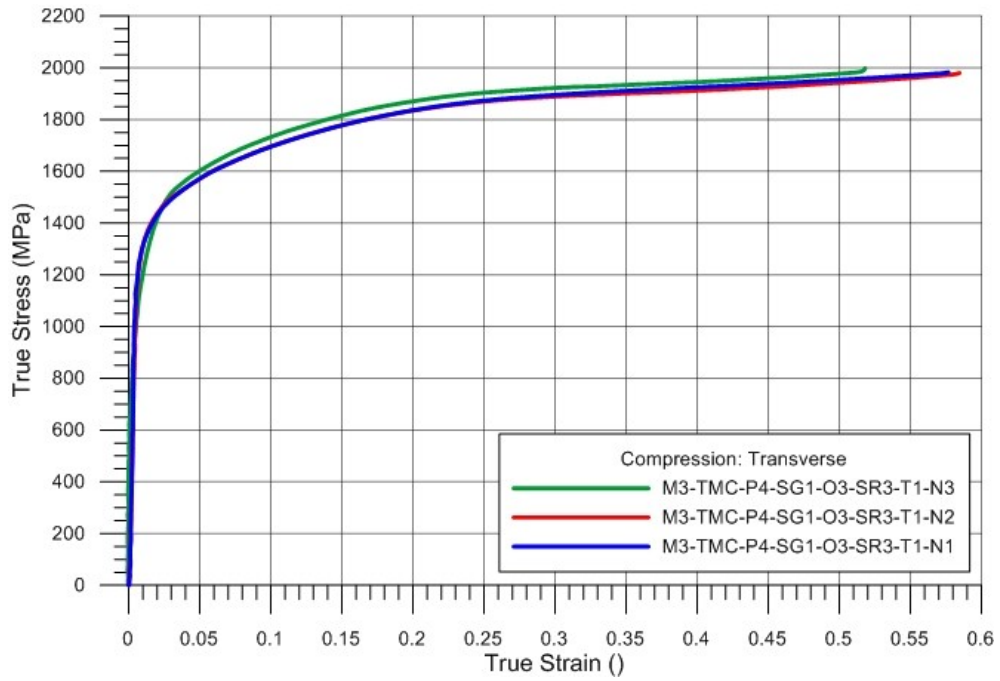


Figure B.17: Experimental results for compression experiments conducted at  $1.00s^{-1}$  in the transverse direction.

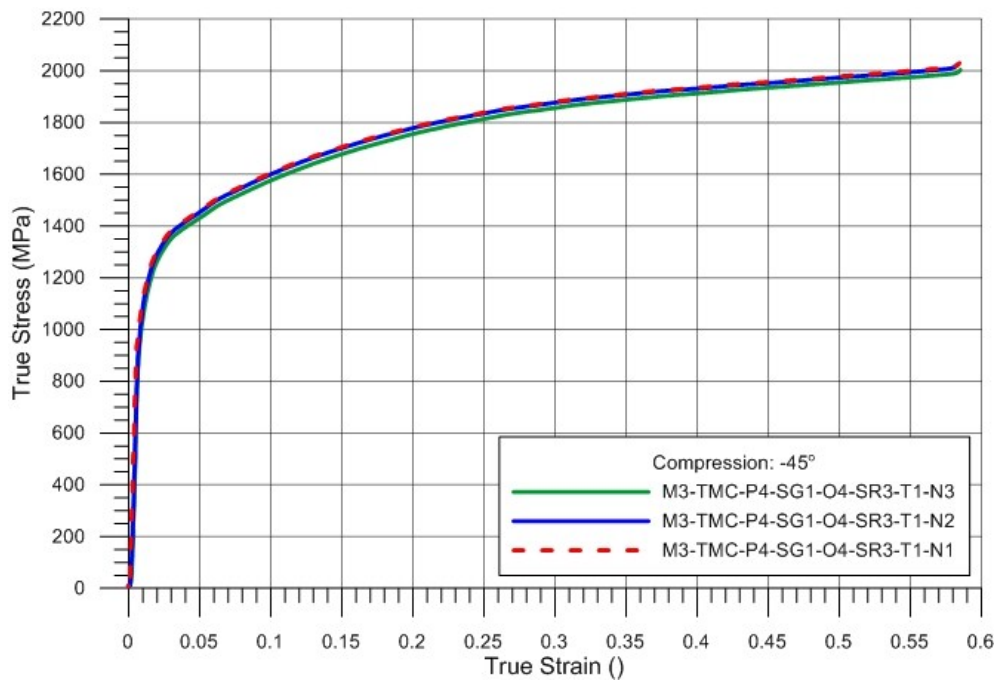


Figure B.18: Experimental results for compression experiments conducted at  $1.00s^{-1}$  in the  $-45^\circ$  direction.

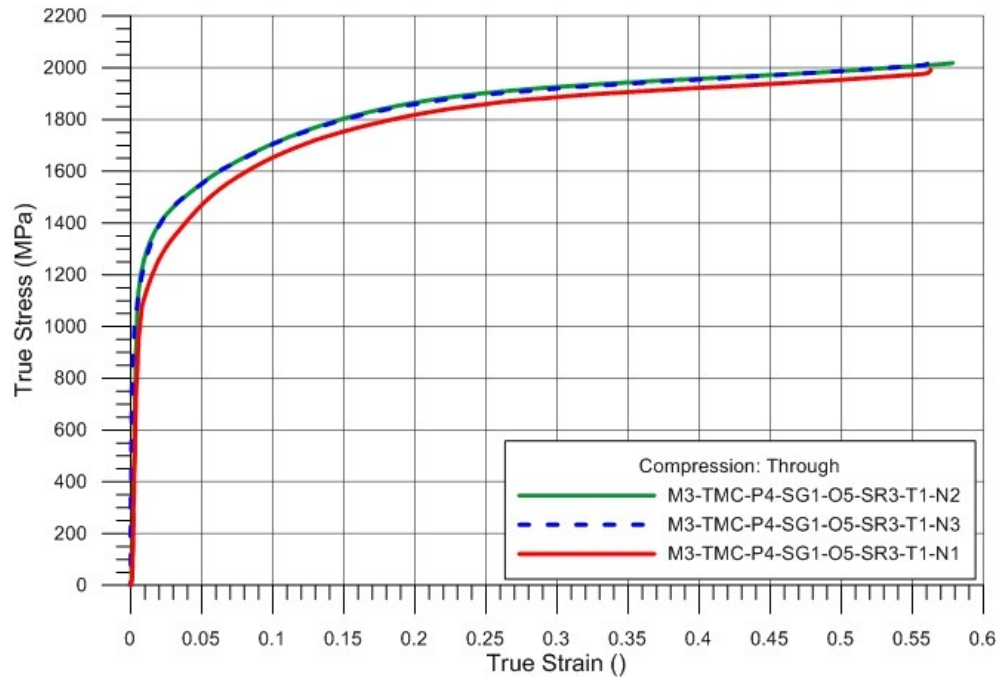


Figure B.19: Experimental results for compression experiments conducted at  $1.00\text{s}^{-1}$  in the direction through the thickness.

## **Appendix C: Finite Element Meshes Used in the Design of Specimen Geometries for the Ductile Fracture Test Series.**

This appendix contains images of the finite element meshes used in the design of tensile specimens for the ductile fracture test series.

## C.1 Plane Stress Specimens

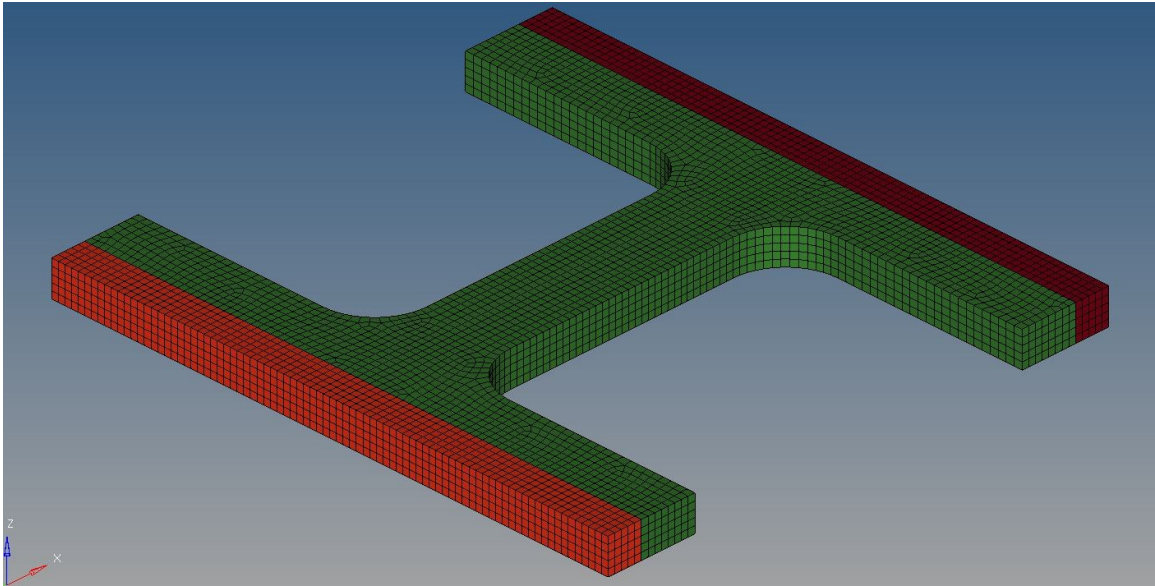


Figure C.1: Mesh for SG1, plane stress smooth, geometry.

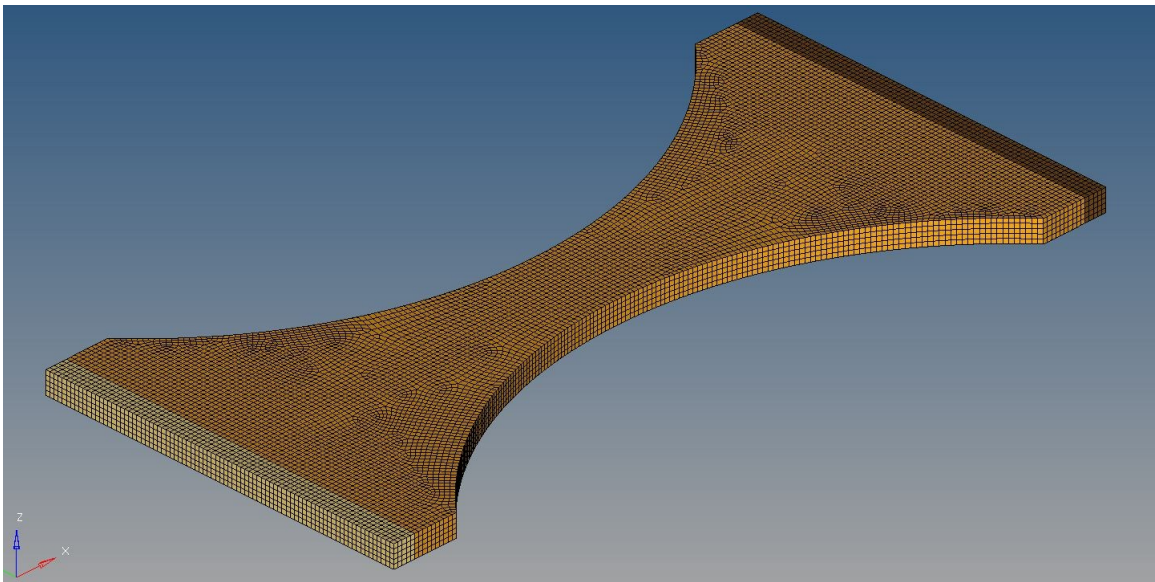
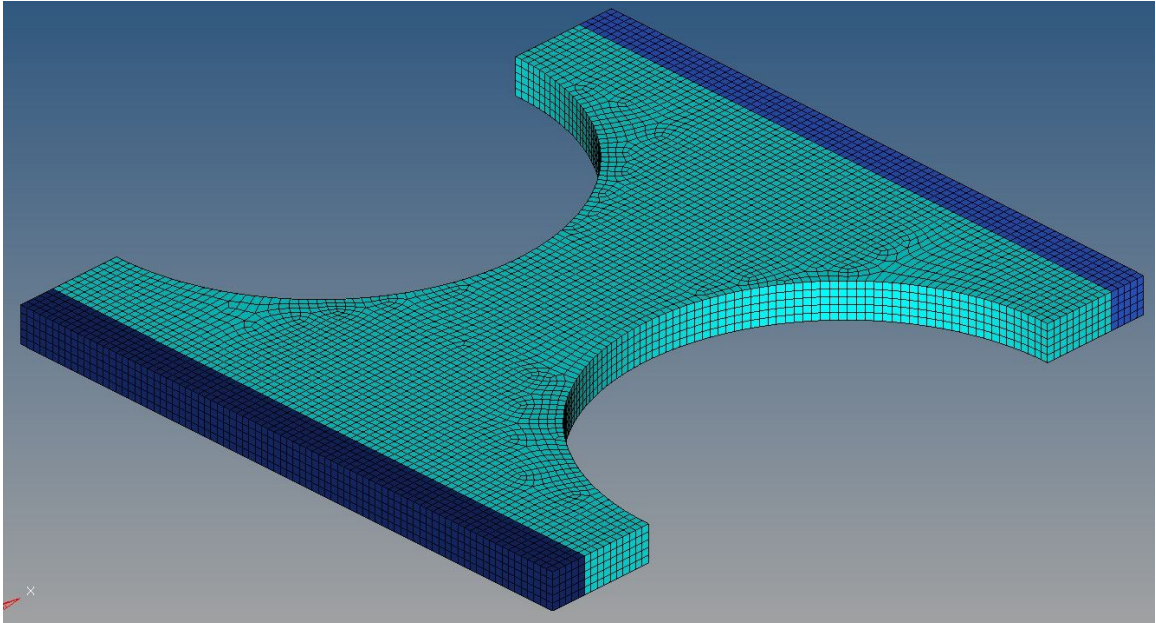
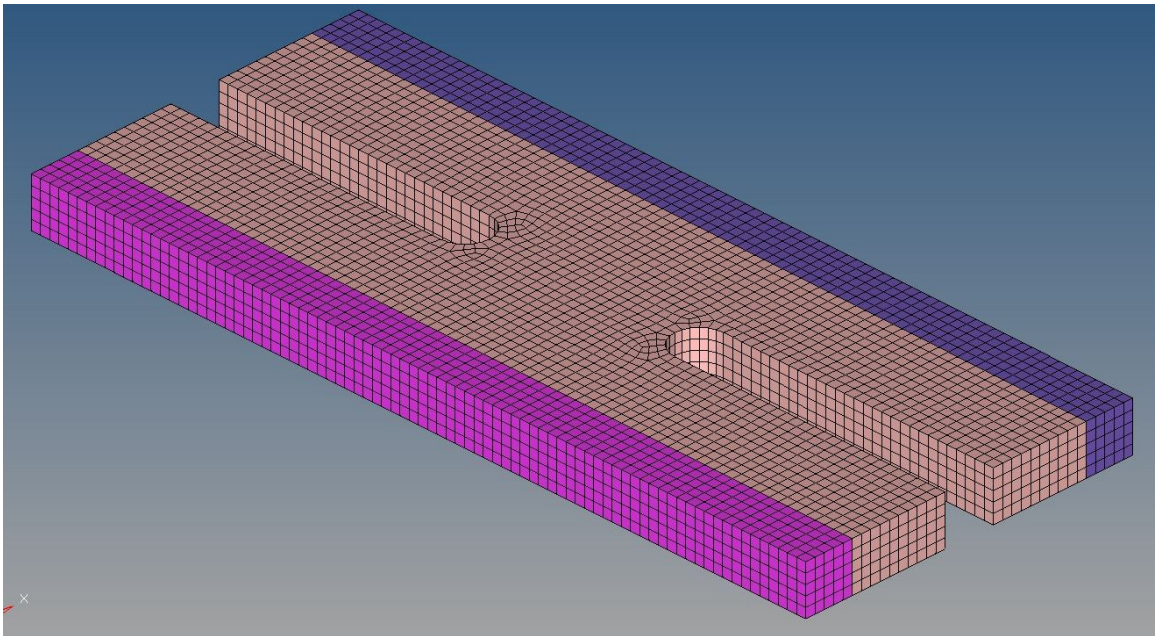


Figure C.2: Mesh for SG2, plane stress large notched, geometry.



**Figure C.3: Mesh for SG3, plane stress medium notched, geometry.**



**Figure C.4: Mesh for SG4, plane stress small notched, geometry.**

## C.2 Plane Strain Specimens

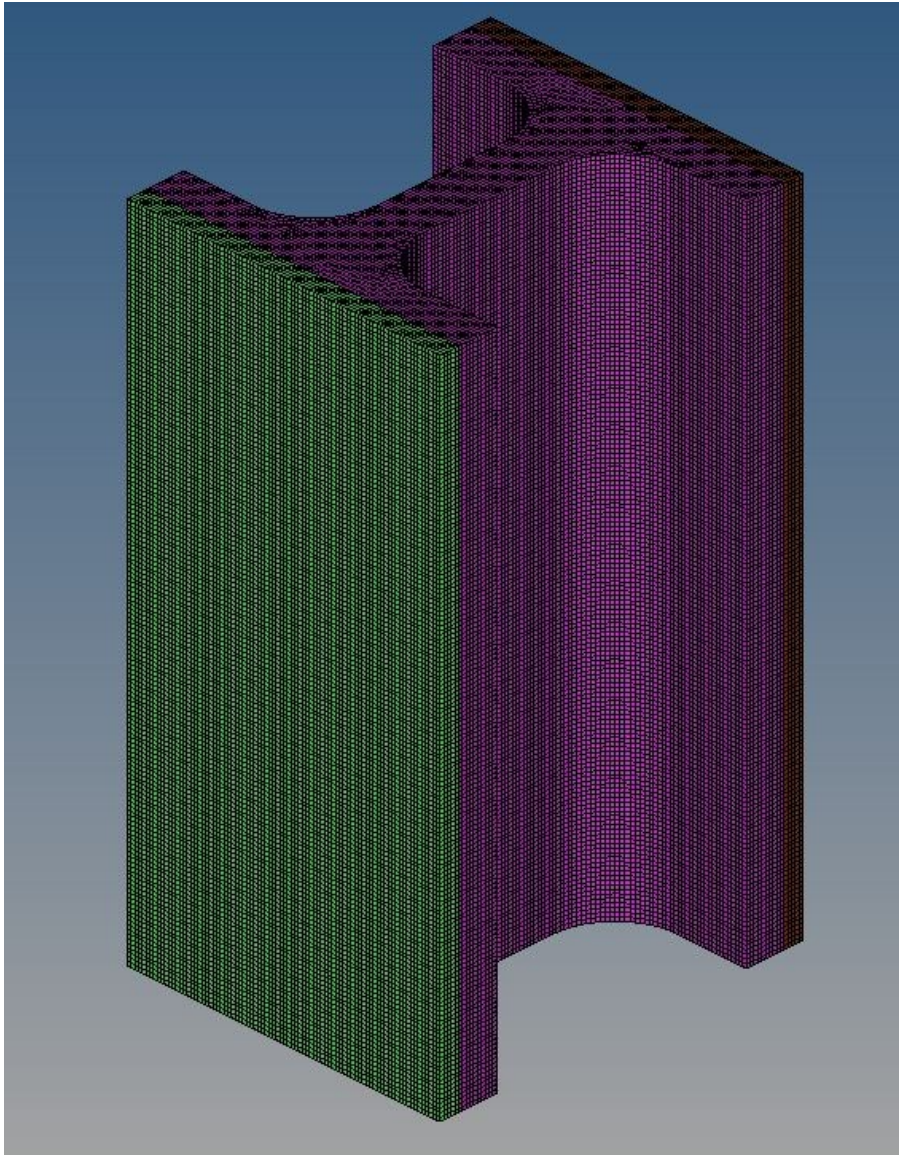
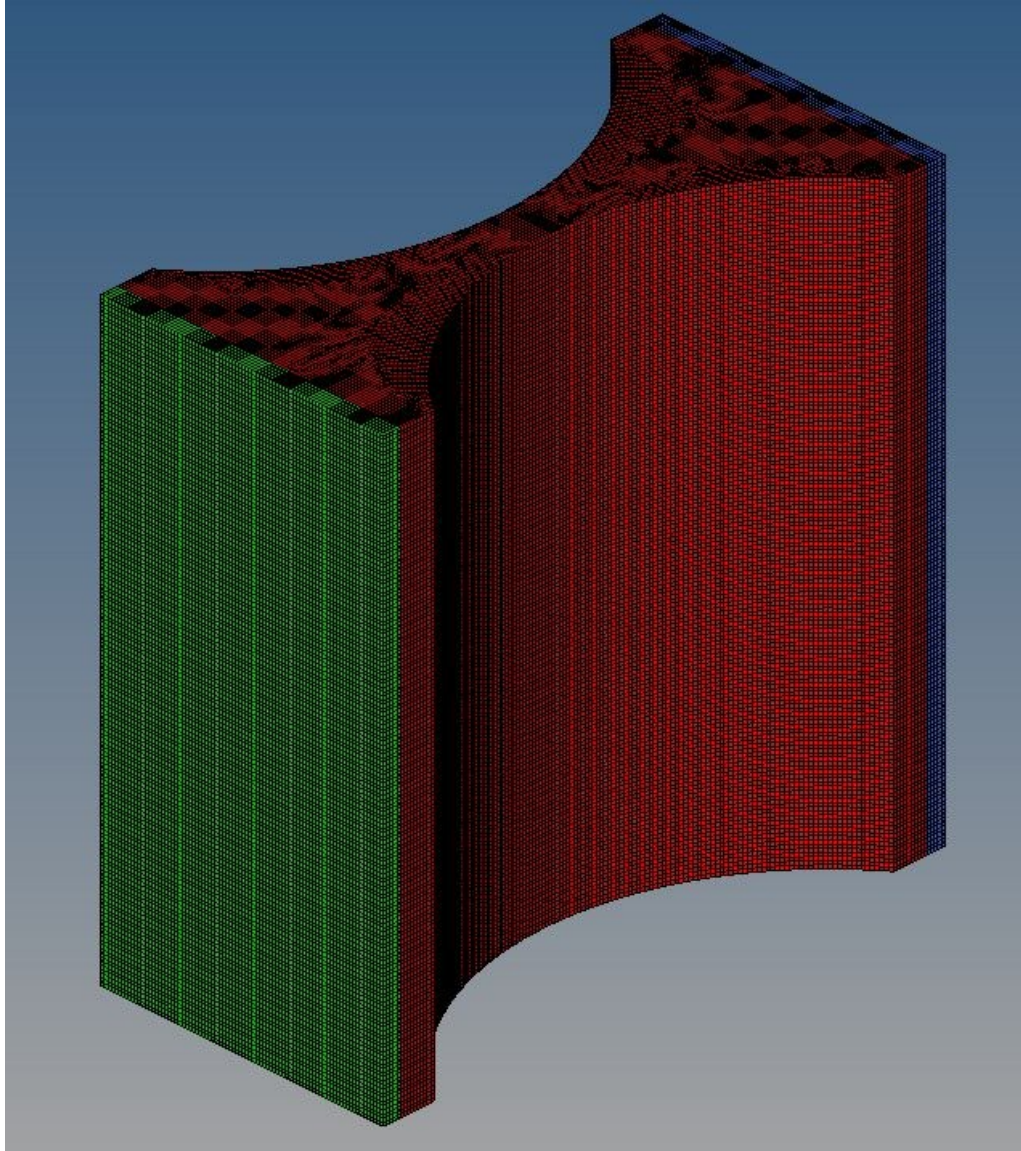
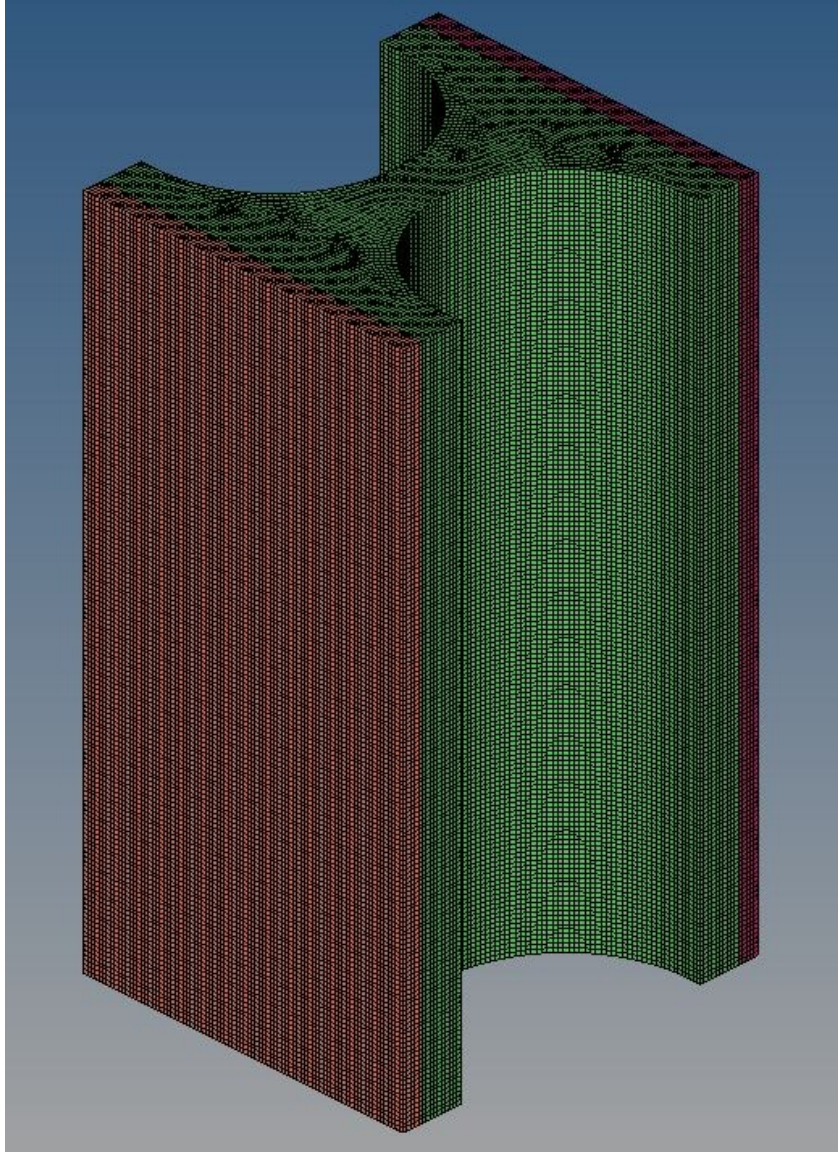


Figure C.5: Mesh for SG11, plane strain smooth, geometry.



**Figure C.6:** Mesh for SG12, plane strain large notch, geometry.



**Figure C.7: Mesh for SG13, plane strain medium notch, geometry.**

### C.3 Axisymmetric Specimens

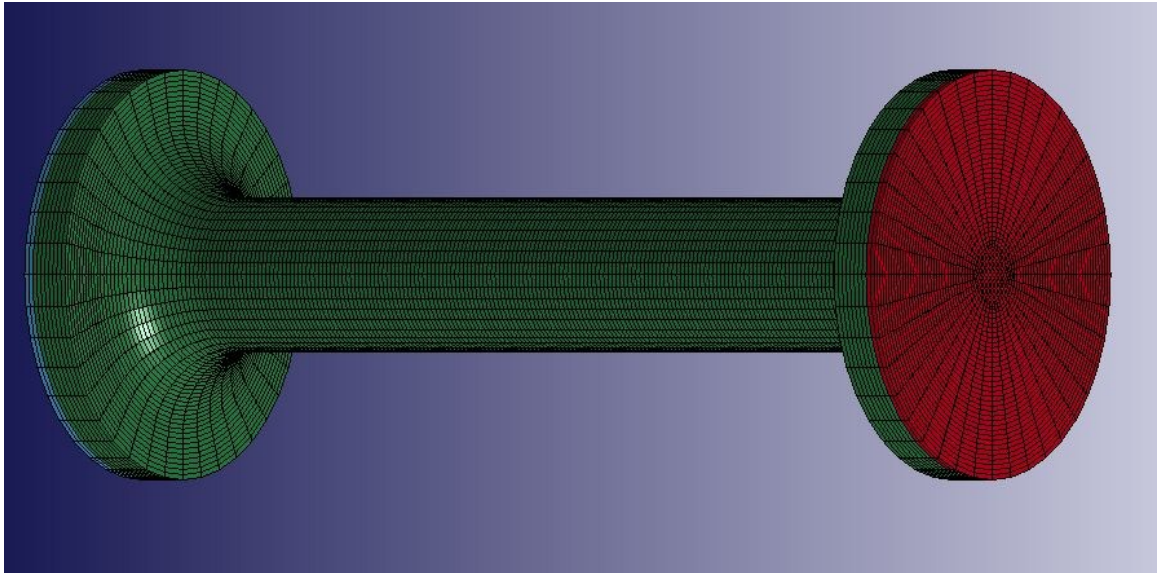
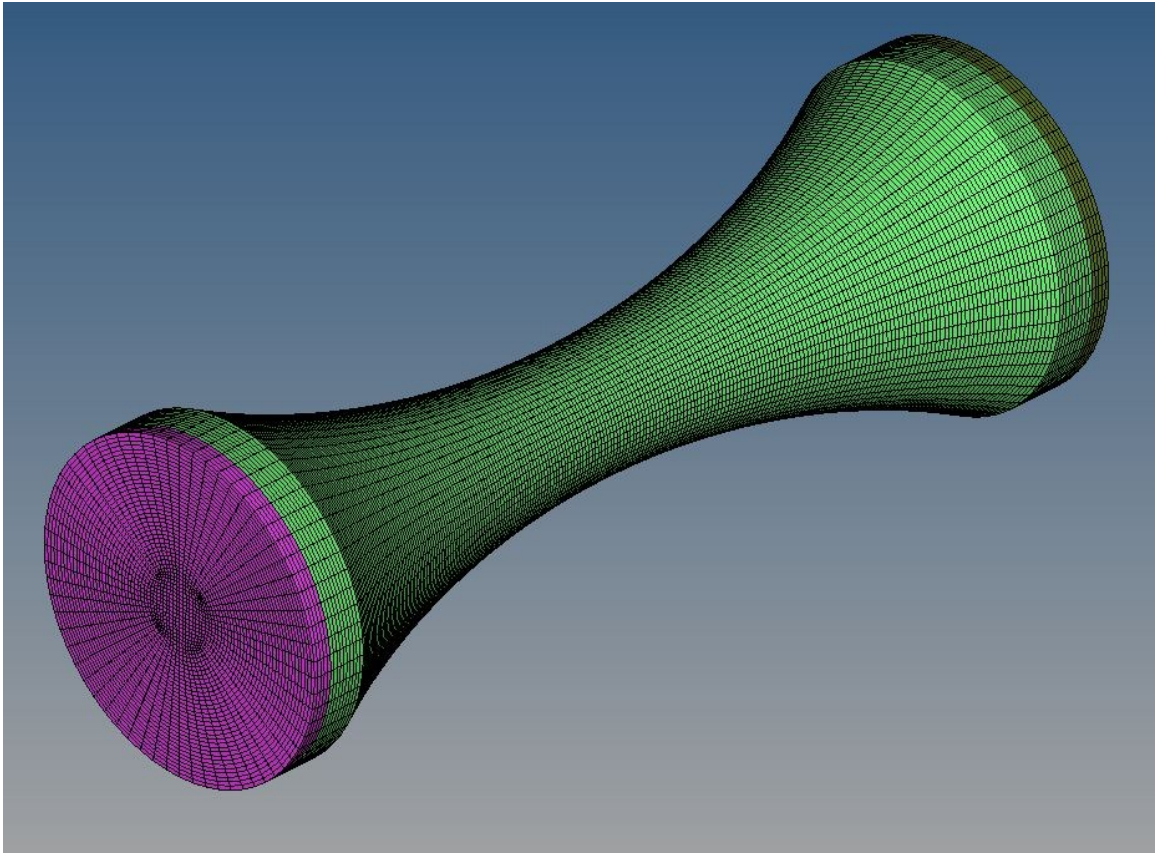


Figure C.8: Mesh for SG5, axisymmetric smooth, geometry.



**Figure C.9: Mesh for SG6, axisymmetric notched, geometry.**

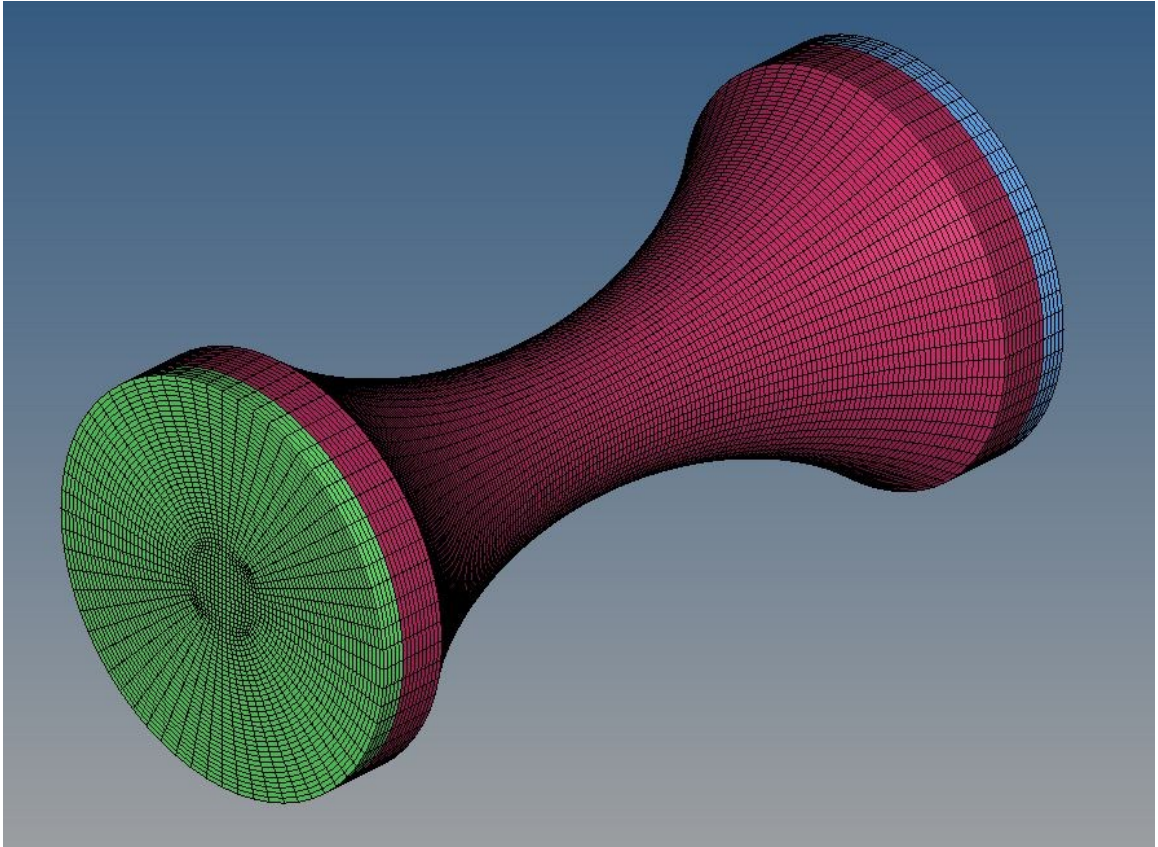
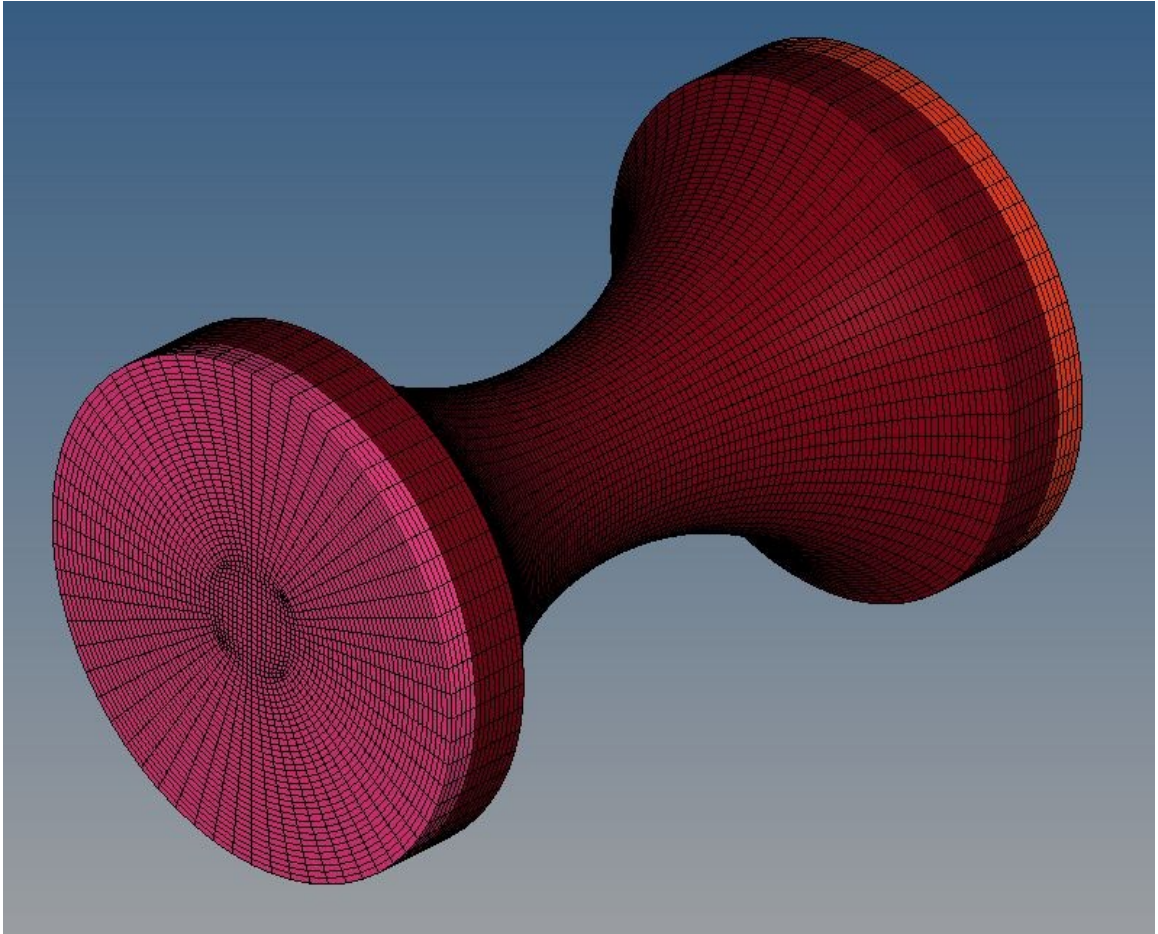


Figure C.10: Mesh for SG7, axisymmetric notched, geometry.



**Figure C.11: Mesh for SG8, axisymmetric notched, geometry.**

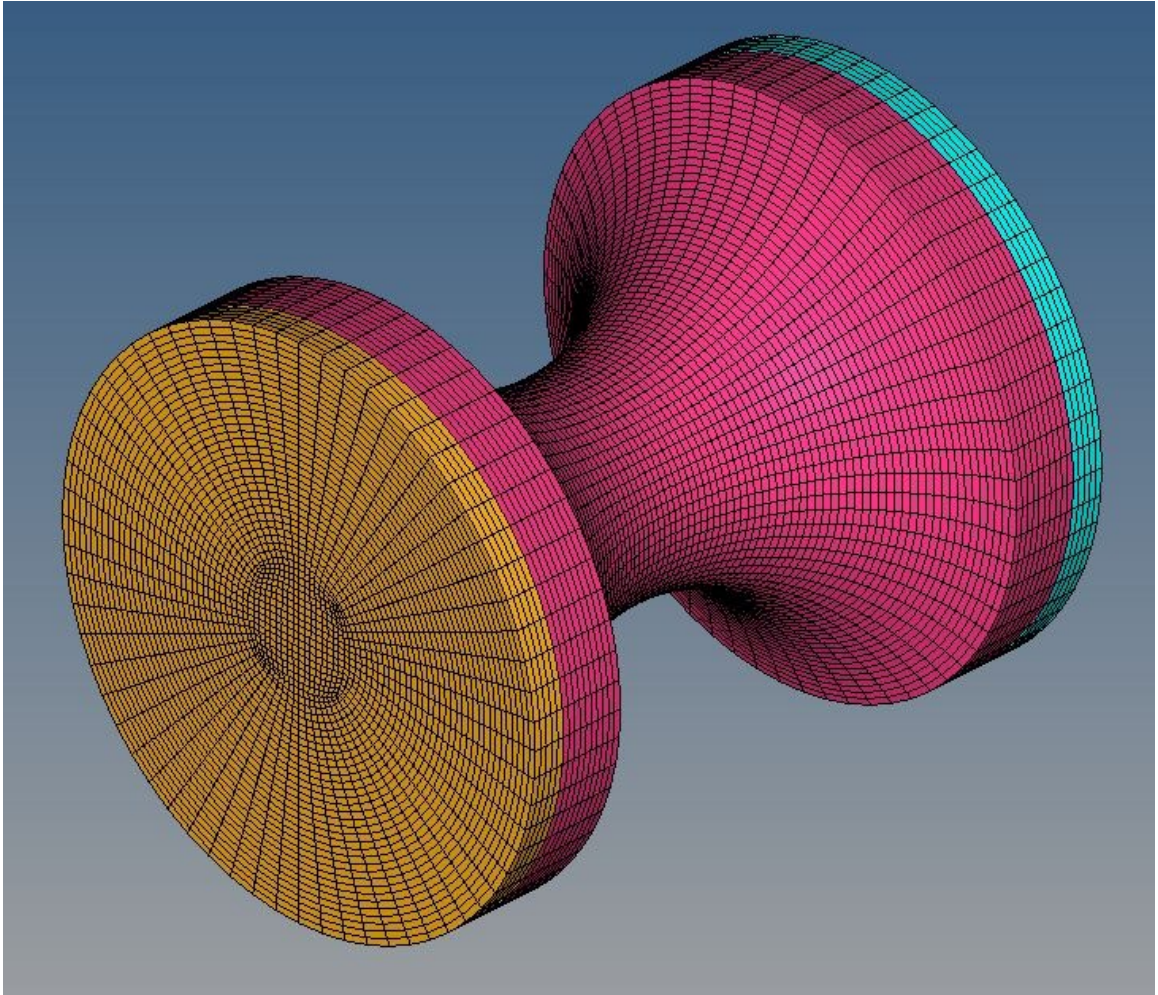


Figure C.12: Mesh for SG9, axisymmetric notched, geometry.

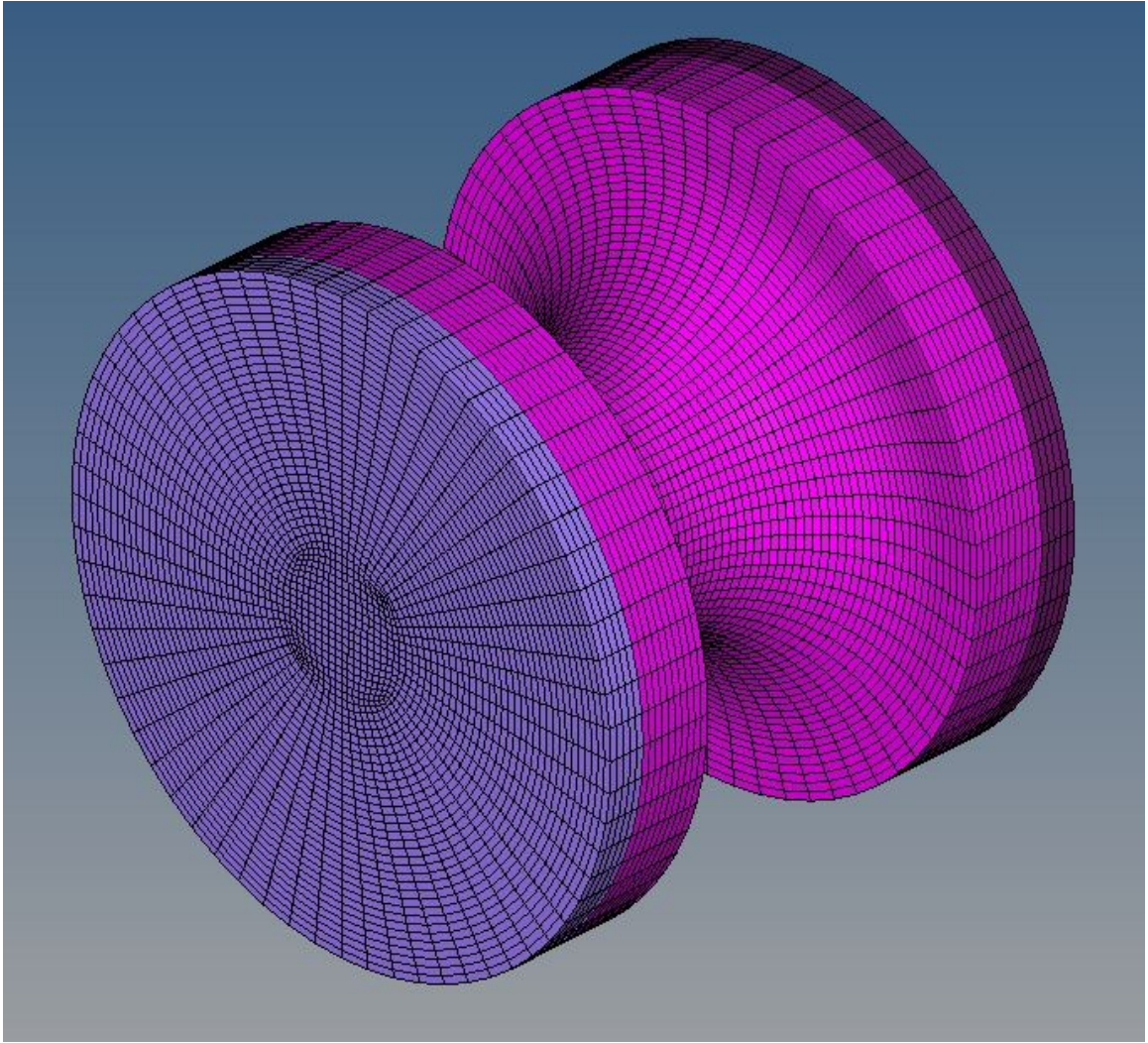


Figure C.13: Mesh for SG10, axisymmetric notched, geometry.

## Bibliography

- [1] Johnson, G. R., and Cook, W.H. "A constitutive model and data for metals subjected to large strains, high strain rates and high temperatures." *Proceedings of the 7th International Symposium on Ballistics*. Vol. 21. 1983.
- [2] LSTC. *LS-DYNA Keyword User's Manual, Volumes I and II, Version 971*. Livermore, CA, 2007.
- [3] Australian Transport Safety Bureau. *In-flight Uncontained Engine Failure - Overhead Batam Island, Indonesia - 4 November 2010, VH-OQA, Airbus A3800842*. Rep. no. AO-2010-089. Canberra City: Australian Transport Safety Bureau, 2010.
- [4] "ASN Aircraft Accident Boeing 737-2H7C TJ-CBD Douala Airport (DLA)." *Aviation Safety Network*. N.p., n.d. Web. 30 Mar. 2014. <<http://aviation-safety.net/database/record.php?id=19840830-0>>.
- [5] National Transportation Safety Board. *Aircraft Accident Report - United Airlines Flight 232, McDonnell Douglas DC-10-10, Sioux Gateway Airport, Sioux City, Iowa, July 19, 1989*. Rep. no. NTSB/AAR-90/06. Washington D.C.: National Transportation Safety Board, 1990.
- [6] Hammer, J.T. *Plastic Deformation and Ductile Fracture of Ti-6Al-4V under Various Loading Conditions*. Thesis. The Ohio State University, 2012.
- [7] ASTM Standard E 643-09, 2009, "Standard Test Method for Ball Punch Deformation of Metallic Sheet Material", ASTM International, West Conshohocken, PA, 2009, [www.astm.org](http://www.astm.org).
- [8] Zukas, J.A. *Impact Dynamics*. New York: Wiley, 1982.
- [9] Bai, Y., and Wierzbicki, T. "Application of Extended Mohr–Coulomb Criterion to Ductile Fracture." *International Journal of Fracture* 161.1 (2010): 1-20.
- [10] Barsoum, I. and Faleskog, J., "Rupture Mechanics in Combined Tension and Shear Experiments." *International Journal of Solids and Structures*, 44:1768-1786, 2007.
- [11] Xue, L., "Damage Accumulation and Fracture Initiation in Uncracked Ductile Solids Subjected to Triaxial loading." *International Journal of Solids and Structures*, 44:5163-5181, 2007.

- [12] Carney, K.S., DuBois, P.A., Buyuk, M., Kan, S., "Generalized Three-Dimensional Definition, Description and Derived Limits of the Triaxial Failure of Metals". *Journal of Aerospace Engineering*, Vol. 22, No. 3, 2009, pp 280-286.
- [13] Mohr, D., Henn, S., "Calibration of stress-triaxiality dependent crack formation criteria: A new hybrid experimental-numerical method", *Experimental Mechanics*, Vol. 47, 2007, pp 805-820.
- [14] Mohr, D., Ebnoether, F., "Plasticity and fracture of martensitic boron steel under plane stress conditions", *International Journal of Solids and Structures*, Vol. 46, 2009, pp 3535-3547.
- [15] Lee, Y-W, Woertz, J.C., and Wierzbicki, T. "Fracture Prediction of Thin Plates under Hemi-spherical Punch with Calibration and Experimental Verification." *International Journal of Mechanical Sciences* 46.5 (2004): 751-81.
- [16] Grytten, F., Børvik, T., Hopperstad, O.s., and Langseth, M. "Low Velocity Perforation of AA5083-H116 Aluminium Plates." *International Journal of Impact Engineering* 36.4 (2009): 597-610.
- [17] Chen, X., et al. "Full Field Strain Measurement of Punch-stretch Tests Using Digital Image Correlation." *SAE International Journal of Materials & Manufacturing* 5.2 (2012): 345-351.
- [18] Reu, P.L., VanGoethem, D.J., and Cordova, T.E. "Measurement of Steel Plate Perforation Tests with Digital Image Correlation." *Proceedings of the 2009 SEM Annual Conference and Exposition on Experimental and Applied Mechanics*. Albuquerque, NM. 2009.
- [19] Walters, C.L., "Dynamic Bulging Technique for Testing Fracture in Intermediate Strain Rates", *Proceedings of the 2009 SEM Annual Conference and Exposition on Experimental and Applied Mechanics*, Albuquerque, NM, June, 2009.
- [20] Zurek, A.K. "The Study of Adiabatic Shear Band Instability in a Pearlitic 4340 Steel Using a Dynamic Punch Test." *Metallurgical and Materials Transactions A* 25.11 (1994): 2483-489.
- [21] Roessig, K.M, and Mason, J.J. "Adiabatic Shear Localization in the Dynamic Punch Test, Part I: Experimental Investigation." *International Journal of Plasticity* 15.3 (1999): 241-62.
- [22] Roessig, K.M, and Mason, J.J. "Adiabatic Shear Localization in the Dynamic Punch Test, Part II: Numerical Simulations." *International Journal of Plasticity* 15.3 (1999): 263-83.
- [23] Gilat, A., Seidt, J.D., "Dynamic Punch Testing of 2024-T351 Aluminum", *Shock Compression of Condensed Matter 2009: Proceedings of the American Physical Society*

Topical Group on Shock Compression of Condensed Matter, Nashville, TN, June/July, 2009.

- [24] Gaudillière, C., Ranc, N., Larue, A., Maillard, A., and Lorong, P. "High Speed Blanking: An Experimental Method to Measure Induced Cutting Forces." *Experimental Mechanics* 53.7 (2013): 1117-126.
- [25] Xiao, H., Bruhns, O.t., and Meyers, A. "Explicit Dual Stress-strain and Strain-stress Relations of Incompressible Isotropic Hyperelastic Solids via Deviatoric Hencky Strain and Cauchy Stress." *Acta Mechanica* 168.1-2 (2004): 21-33.
- [26] Demange, J.J., Prakash V., and Pereira, J.M. "Effects of Material Microstructure on Blunt Projectile Penetration of a Nickel-based Super Alloy." *International Journal of Impact Engineering* 36.8 (2009): 1027-043.
- [27] Sciuva, M.D., Frola, C., and Salvano, S. "Low and High Velocity Impact on Inconel 718 Casting Plates: Ballistic Limit and Numerical Correlation." *International Journal of Impact Engineering* 28.8 (2003): 849-76.
- [28] Pereira, J.M., and Lerch, B.A. "Effects of Heat Treatment on the Ballistic Impact Properties of Inconel 718 for Jet Engine Fan Containment Applications." *International Journal of Impact Engineering* 25.8 (2001): 715-33.
- [29] Kobayashi, T., Simons, J.W., Brown, C.S., and Shockey, D.A. "Plastic Flow Behavior of Inconel 718 under Dynamic Shear Loads." *International Journal of Impact Engineering* 35.5 (2008): 389-96.
- [30] Zhang, B., Mynors, D.J., Mugarra, A., and Ostolaza, K. "Representing the Superplasticity of Inconel 718." *Journal of Materials Processing Technology* 153-154 (2004): 694-98.
- [31] Xue, H., Lijun, W., Hui, X., Runguang, L., Shaogang, W., and Zhonglin, C. "Superplastic Properties of Inconel 718." *Journal of Materials Processing Technology* 137.1-3 (2003): 17-20.
- [32] Yoo, J.T., Yoon, J.H., Lee, H.S., and Youn, S.K. "Material Characterization of Inconel 718 from Free Bulging Test at High Temperature." *Journal of Mechanical Science and Technology* 26.7 (2012): 2101-105.
- [33] Zhang, S.H., Zhang, H.Y., and Cheng, M. "Tensile Deformation and Fracture Characteristics of Delta-processed Inconel 718 Alloy at Elevated Temperature." *Materials Science and Engineering: A* 528.19-20 (2011): 6253-258.
- [34] Thomas, A., El-Wahabi, M., Cabrera, J.M., and Prado, J.M. "High Temperature Deformation of Inconel 718." *Journal of Materials Processing Technology* 177.1-3 (2006): 469-72.

- [35] G.H. Staab and A. Gilat. A direct-tension split Hopkinson bar for high strain-rate testing. *Experimental Mechanics*, 31:232-235. 1991.
- [36] A. Gilat, T.E. Schmidt, A.L. Walker. Full Field Strain Measurements in Compression and Tensile Split Hopkinson Bar Experiments. *Experimental Mechanics*, 49: 291-302. 2009.
- [37] G. T. Gray III. Classic split-hopkinson pressure bar testing, *ASM Handbook*, 8:462-476, 2000.
- [38] Sutton, M.A., Orteu, J.J., and Schreier, H.W. *Image Correlation for Shape, Motion and Deformation Measurements: Basic Concepts, Theory and Applications*. New York, NY: Springer, 2009.
- [39] Inc. Correlated Solutions. Correlated solutions: Non-contacting measurement solutions. <<http://www.correlatedsolutions.com>>, March 2014.
- [40] N.S. Stoloff, Wrought and P/M Superalloys, *Properties and Selection: Irons, Steels, and High-Performance Alloys*, Vol 1, *ASM Handbook*, ASM International, 1990, 950-980.
- [41] C.R. Brinkman and G.E. Korth. Strain Fatigue and Tensile Behavior of Inconel 718 from Room Temperature to 650°C. *Journal of Testing and Evaluation*. 2:4: 249-259. 1974.
- [42] Special Metals. *Inconel Alloy 718*. Special Metals Corporation, Sept. 2007. Web. 30 Mar. 2014. <[www.specialmetals.com](http://www.specialmetals.com)>.
- [43] Seidt, J.D. *Plastic deformation and ductile fracture of 2024-T351 aluminum under various loading conditions*. Dissertation. The Ohio State University, 2010.
- [44] P.W. Bridgman. Studies in large plastic flow and fracture, with special emphasis on the effect of hydrostatic pressure. *Harvard University Press*, 1964.
- [45] M. Buyuk, P. DuBois, J. He, and S. Kan. Procedure for the determination of the specimen geometries. *Presentation Slides May 7<sup>th</sup>*, 2010.